

**Experiments with Feshbach molecules in a
Bose-Fermi mixture**

by

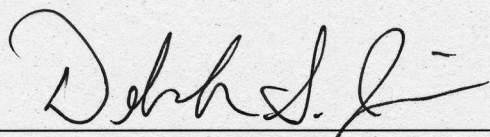
Michele Lynn Olsen

B.A. Physics, State University of New York at Geneseo,

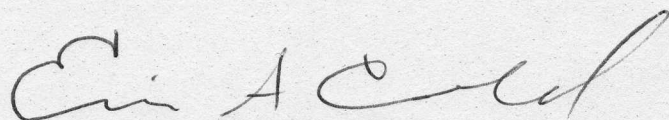
2001

A thesis submitted to the
Faculty of the Graduate School of the
University of Colorado in partial fulfillment
of the requirements for the degree of
Doctor of Philosophy
Department of Physics
2008

This thesis entitled:
Experiments with Feshbach molecules in a Bose-Fermi mixture
written by Michele Lynn Olsen
has been approved for the Department of Physics



Deborah S. Jin



Eric A. Cornell

Date 11/25/2008

The final copy of this thesis has been examined by the signatories, and we find
that both the content and the form meet acceptable presentation standards of
scholarly work in the above mentioned discipline.

Olsen, Michele Lynn (Ph.D., Physics)

Experiments with Feshbach molecules in a Bose-Fermi mixture

Thesis directed by Dr. Deborah S. Jin

In this thesis, I present studies of the creation of ultracold heteronuclear molecules from a dilute gas mixture of ^{87}Rb and ^{40}K . Using a Fano-Feshbach resonance, atom pairs are associated into molecules via time-dependent magnetic fields. Slow magnetic-field sweeps are used to make large samples of highly vibrationally excited KRb molecules, while rapid magnetic-field pulses are used to create quantum superpositions of atom and molecule states. Rabi- and Ramsey-type experiments demonstrate coherent oscillations between atoms and molecules. This new type of quantum superposition involves particles of different statistics (i.e. bosons and fermions) and demonstrates atom-molecule coherence without a Bose-Einstein condensate (BEC). These atom-molecule oscillations may provide a unique way to probe the many-body behavior of a strongly interacting Bose-Fermi mixture.

Acknowledgements

The work presented in this thesis could not have happened without the contributions of many different people. First, I have to thank my advisor, Debbie, for giving me the opportunity to work on this project and for all her help over the years. In addition to experimental and theoretical guidance, Debbie worked side-by-side with me in the lab for a while as a “post post-doc”, and even rewrote our experiment control software. More importantly, though, her uncanny ability to reduce a problem to its key elements has taught me how to attack almost any problem. I can only hope that some of her determination, enthusiasm, and physical intuition has rubbed off. I would also like to thank her for a bit of personal understanding. She was very supportive when I hit my breaking point with the experiment after months and months of frustration and personal struggles and made every effort to help.

As part of the ultracold atom group, I have also benefitted from two additional advisors, Eric Cornell and Carl Wieman. They were never at a loss for suggestions on how to improve a particular experiment or how to fix a laser or how best to present data in a poster or talk. Their years of experience with ultracold experiments have built a seemingly limitless pool of knowledge and intuition. They are among the few people you actually take seriously when they suggest taking a hammer or wrench to your vacuum system (okay, the ion pump)—I have to admit, that was kind of fun. While I never particularly relished giving talks at

the group seminars, I am thankful for the emphasis Carl, Eric, and Debbie placed on giving good talks and clearly presenting scientific data.

During my time in the lab, I've been fortunate to have worked with some wonderful people. Jon Goldwin and Shin Inouye were the grad student and post-doc on the experiment when I joined the lab. Jon and Shin were patient with all my questions and taught me everything from how to align a laser beam to how to design experiments. I learned from them how to run a lab (and sometimes how not to). Shortly after Jon and Shin moved on to bigger and better things, Tyler Cumby joined our lab as a grad student. Though Ty and I haven't always seen eye to eye, his quiet dedication has been instrumental in the results of this thesis. John Perreault joined us as a post-doc two years ago. John came on the experiment just when I needed him most. He was a breath of fresh air at a time when the experiment was stuck in the muck. His new perspective helped us get the experiment back on its feet and moving forward. John's experience with interferometry proved indispensable in our most recent work, but more importantly, his easy-going nature and optimism made working in the lab fun again. A new grad student, Ruth Shewmon, joined the lab only a few months ago. Already, I can see that she will be a valuable addition, and I hope that I have left her with an experiment that will be productive for years to come.

There are several other people who worked on the experiment with me and deserve special thanks. Brett De Paola was a Visiting Fellow who worked in our lab during my first year at JILA. He helped me build and temperature stabilize my first laser (which is still in operation today). Jian-ying Lang, a grad student who worked with me for a while, helped me redesign, rebuild, and reoptimize the apparatus. I've never worked with anyone with as strong a work ethic as Jian-ying. Jesper Bertelsen spent a few months in the lab as an exchange student and helped with some of our early efforts at molecule creation. I'd also like to thank

Cindy Regal, who took time away from her own experiment to help me build my new vacuum system. Thanks also go to two undergrads who worked with us, Bonna Newman and Margot Phelps.

I would also like to thank a few additional members of the “Tri-group” who have made contributions large and small. Paul Haljan taught me about imaging and camera controls and first introduced me to the worlds of Frame Transfer and Kinetics Mode. Scott Papp could always be counted on for advice (sometimes unsolicited) on how to improve various aspects of the experiment. Josh Zirbel and Kang-Kuen Ni offered new expertise on Rb and K and a bit of friendly competition in making molecules. Countless other grad students and post-docs have impacted the workings of the experiment and made JILA a fun place to work through parties and lunches and ski trips and chatting in labs and hallways and semi-annual grudge matches with the Ye group.

One of the greatest aspects of JILA is its staff. Without the members of the electronic shop, machine shop, scientific reports office, supply office and administration, none of the experiments we do would be possible. In particular, I’d like to thank Tom Foote, Hans Green, and Todd Asnicar of the machine shop. Tom machined the forms for our IP trap, and Hans and Todd built me not one, but two collection cells, complete with getters and ampoules, and the second one in a turn-around time of a week or two! In the electronics shop, I’d like to thank James Fung-A-Fat and Terry Brown for always answering my questions about the many servos we use, and Carl Sauer for painstakingly mode-matching microwave coils for me. I’d also like to thank Julie Phillips in the SRO for help and support with our most recent paper.

Throughout the years, there have been a handful of people that I could always count on for a laugh, a place to hang out, or a shoulder to cry on. Ian Coddington, Rachel Doriese, Chris Jones, Etienne Gagnon, Odele Hofmann Brian

Laughman, Nathan Miller (now Tomlin), Kerry Tomlin, Nick Wagner, Mike and Eva Ziemkiewicz all deserve special thanks. Chris, Etienne, Brian, Nathan, Nick, and I all started out in the physics program together. We bonded over interminable homework sets of classical and quantum mechanics in the tower and have been friends ever since. From camping and ski trips and bull-riding birthday parties and volleyball to countless pint nights, trivia nights, game nights, girl's nights and let's-go-grab-dinner nights, they've all made my grad school years unforgettable. Special thanks go to Etienne, my roommate of 4 years, for putting up with my messes and being someone to come home to, and Chris, for being my confidante over TV and cocktails (a few too many, maybe?), and Kerry, what can I say? she's my best friend. And, of course, I have to thank Nick, my eternal partner in adventure. I've never known Nick to turn down a day of skiing or hiking, and in our quasi-annual vacations, we've visited 15 national parks and monuments, 3 countries, one Indian reservation and who knows how many miles of highway. I cannot imagine my life without any of these fantastic friends.

Last, but definitely not least, I'd like to thank my family, Sheila, Alan, and Melissa, for all their love and support through the years.

Contents

Chapter

1	Introduction	1
1.1	Fun things to do with Bose-Fermi mixtures	2
1.2	The state of affairs	4
1.3	Atom-molecule coherence	6
1.3.1	Quantum superpositions	7
1.3.2	Atom-molecule superpositions in a Bose-Fermi mixture . .	8
1.4	Overview of this thesis	8
2	Experimental improvements	11
2.1	Experimental sequence	11
2.2	New vacuum system	13
2.2.1	Large, controllable K MOTs	17
2.2.2	Model of a two-species MOT	19
2.3	Keeping all those atoms	26
2.3.1	Fiber coupling the MOT light	26
2.3.2	Spin state purification	30
2.3.3	Quadrupole trap to IP trap transfer	34
2.4	Too much of a good thing?	35
2.5	Magnetic-field curvature compensation	41

2.6	Fast magnetic-field pulse circuit and eddy current correction	42
2.7	High-field absorption imaging	48
2.8	Isolating the track controller that spews noise all over the lab	53
3	Creating molecules with a Fano-Feshbach resonance	58
3.1	Fano-Feshbach resonances	58
3.2	Locating the resonances with atom loss	60
3.3	KRb Feshbach molecules	63
3.3.1	Magnetic-field sweeps	65
3.3.2	Density dependence of molecule creation sweep rates	69
3.3.3	Why we no longer use a 1075 nm broadband laser	70
3.4	Molecule imaging	70
3.5	Locating the resonance with molecule sweeps	74
4	Semiclassical Monte Carlo simulations of molecule conversion	76
4.1	Monte Carlo simulation	77
4.2	Two-component systems	78
4.3	^{40}K - ^{87}Rb Bose-Fermi mixture in particular	80
4.3.1	Number ratio	85
4.3.2	Gravitational sag	89
4.3.3	Molecule conversion in expansion	92
5	Coherent atom-molecule oscillations	96
5.1	Rabi and Ramsey oscillations in the atom + photon system	96
5.2	Criteria for observing oscillations	102
5.3	Ramsey oscillations	104
5.3.1	Empirical optimization	105
5.3.2	Frequency dependence on B	108

5.3.3	Amplitude dependence on density	110
5.3.4	Ramsey oscillations in expansion	112
5.4	Rabi oscillations	114
5.4.1	Ramsey oscillations without Rabi oscillations?	114
5.4.2	Rabi oscillations in expansion	118
5.4.3	Amplitude dependence on B	121
5.4.4	Frequency dependence on B	121
5.5	Oscillation decoherence/dephasing	123
5.5.1	Non-technical mechanisms	123
5.5.2	Technical mechanisms	131
6	As yet unsubstantiated Monte Carlo predictions	134
6.1	Assumptions	135
6.2	Dependence of coherence times on temperature	136
6.3	Dependence of coherence times on quantum degeneracy	138
7	Conclusions and Outlook	142
Bibliography		144
Appendix		
A	Fitting dephased oscillations	154
B	Nearest-neighbor distance and density-weighted density for Gaussian clouds with different sizes, numbers, and aspect ratios.	161

List of Figures

Figure

1.1	Bosons and fermions at zero temperature.	2
2.1	CAD drawing of the new vacuum system.	15
2.2	CAD drawing of the new vacuum system (top view).	16
2.3	Failed MOT cell with Rb ampoules.	18
2.4	Expected pressure dependence of single-species MOT numbers. . .	22
2.5	Expected dependence of the Rb MOT number on the partial pressures of Rb and K.	23
2.6	Expected dependence of the K MOT number on the partial pressures of Rb and K.	24
2.7	Measured MOT numbers when running only the K getter. . . .	25
2.8	Hyperfine structure of the relevant ground and excited states of ^{40}K and ^{87}Rb	27
2.9	Fiber coupling the MOT light.	28
2.10	Effect of optical molasses on the temperature of the Rb MOT. . .	31
2.11	Rb spin states loaded into the quadrupole trap.	33
2.12	Schematic of the cloud shapes in the quadrupole and Ioffe-Pritchard traps.	35
2.13	Temperature dependence of the fraction of atoms transferred to the IP trap.	36

2.14	Quadrupole to IP trap transfer.	37
2.15	Evaporation in the magnetic trap.	39
2.16	False-color absorption images of a degenerate Fermi gas and a Bose-Einstein condensate.	40
2.17	Magnetic-field curvature cancellation.	43
2.18	Measured axial magnetic-field inhomogeneity.	44
2.19	Circuit used to generate fast magnetic-field ramps.	45
2.20	Magnetic-field ramp determined from the current through the auxiliary coils.	47
2.21	Decaying magnetic field after a magnetic-field ramp.	47
2.22	Schematic of the eddy current model.	48
2.23	Magnetic-field ramps that compensate for eddy fields.	49
2.24	Magnetic-field ramps with eddy current compensation.	49
2.25	Decaying magnetic field after a fast magnetic-field ramp.	50
2.26	Magnetic-field ramps that compensate for eddy fields.	51
2.27	Measured magnetic-field deviation after a fast ramp.	51
2.28	Laser frequencies for trapping, pumping, probing Rb and K.	54
2.29	Schematic of the high-field imaging configuration.	57
2.30	Noise broadcast by the Soloist cart controller.	57
3.1	Schematic of a Fano-Feshbach resonance.	59
3.2	Magnetic-field dependence of the scattering length a at a Fano-Feshbach resonance.	61
3.3	Magnetic-field dependent atom loss at Fano-Feshbach resonances between ^{40}K atoms in the $ 9/2, -9/2\rangle$ state and ^{87}Rb atoms in the $ 1, 1\rangle$ state.	64
3.4	Molecule association with magnetic-field sweeps.	66

3.5	Molecule creation via magnetic-field sweeps through a Fano-Feshbach resonance.	68
3.6	Measured density dependence of adiabatic magnetic-field sweep speeds.	71
3.7	KRb molecular potentials.	72
3.8	Determination of the Fano-Feshbach resonance position via molecule dissociation.	75
4.1	Temperature dependence of the molecule conversion in single-species experiments.	79
4.2	Temperature dependence of the molecule conversion in a bosonic mixture of ^{85}Rb and ^{87}Rb	81
4.3	A simplified energy level diagram for rf association.	82
4.4	Temperature dependence of the molecule conversion in a Bose-Fermi mixture of ^{87}Rb and ^{40}K	84
4.5	Effect of number ratio on molecule conversion for fixed T_C	86
4.6	Effect of number ratio on molecule conversion for fixed T_F	87
4.7	Adiabatic molecule conversion with an excess of fermions.	90
4.8	Effect of gravitational sag on molecule conversion.	91
4.9	Molecule conversion in expansion for two identical Bose gases.	94
4.10	Molecule conversion in expansion for a mixture of Rb and K.	94
5.1	Energy level diagram for an atom in a radiation field.	98
5.2	Eigenstates of the dressed atom.	98
5.3	Ramsey's method of separated oscillatory fields and analogous systems.	101
5.4	Empirical optimization of Ramsey oscillations.	106
5.5	Ramsey-type atom-molecule oscillations.	109

5.6	Magnetic-field dependence of the measured oscillation frequency for the molecule number in Ramsey-type double-pulse experiments.	111
5.7	Density dependence of the amplitude of the molecule oscillations in Ramsey-type experiments.	113
5.8	Empirical optimization of pulse time for a cloud after 1 ms of expansion from the trap.	115
5.9	Time dependence of the molecule number in a single-pulse experiment.	117
5.10	Rabi-type atom-molecule oscillations.	119
5.11	Rabi-type atom-molecule oscillations with varying density clouds.	120
5.12	Magnetic-field dependence of the peak-to-peak amplitude and frequency of the single-pulse oscillations.	122
5.13	Schematic of the energy eigenvalues of a trapped atom pair in the vicinity of a Fano-Feshbach resonance.	124
5.14	Illustration of dephasing.	126
5.15	Calculated oscillations for typical in-trap conditions with coherence times limited by the energy distribution of the pairs.	128
5.16	Calculated oscillations for typical expansion conditions with coherence times limited by the energy distribution of the pairs.	129
5.17	Atom motion in the trap and in expansion.	131
5.18	Magnetic-field dependence of the coherence times of Ramsey oscillations.	133
6.1	Expected temperature dependence of the coherence time of atom-molecule oscillations.	137
6.2	Expected dependence of the atom-molecule oscillation coherence time on quantum degeneracy.	140

6.3	Expected dependence of the nearest-neighbor atom-molecule oscillation coherence time on quantum degeneracy.	141
A.1	Frequency distribution due to an inhomogeneous magnetic field. .	156
A.2	Calculated distribution of relative kinetic energies, E , of nearest-neighbor pairs in a 200 nK Boltzmann gas.	158
A.3	Calculated atom-molecule oscillation for a 200 nK gas with a Boltzmann energy distribution at $B = 546.135\text{G}$	158
A.4	Calculated distribution of the relative kinetic energies E of atom pairs associated into molecules in the Monte Carlo simulation. .	159
A.5	Calculated atom-molecule oscillation for pairs with the distribution shown in Fig. A.4.	159
B.1	Illustration of the calculation of the typical nearest-neighbor distance for a mixture with different numbers of atoms.	162
B.2	Distribution of nearest-neighbor distances d_{nn} for a simulated Gaussian cloud.	163
B.3	Density dependence of the calculated nearest-neighbor distance. .	165

Chapter 1

Introduction

All of the light and matter in the universe can be divided into two categories: bosons and fermions. They are distinguished from one another by their quantum mechanical spins. Bosons have integer values of spin, while fermions have half-integer values of spin. Examples of bosons in nature are photons and phonons, while electrons, protons, and neutrons are fermions. While the distinction between these two categories is not necessarily obvious in our daily lives, whether particles have whole- or half-integer spin determines their quantum mechanical behavior. At sufficiently low temperatures, a group of identical bosons will form a Bose-Einstein condensate (BEC), in which all of the particles occupy the ground state. This macroscopic occupation of a single quantum state is prohibited in groups of identical fermions. Instead, each particle must occupy its own state, leading to a “Fermi sea” with singly filled energy states up to the Fermi level. This leads to a vast difference in energy between groups of fermions and bosons at $T = 0$ (see Fig. 1.1).

In this thesis, I present experiments with an ultracold mixture of bosons (^{87}Rb) and fermions (^{40}K) at an interspecies Fano-Feshbach resonance. I will emphasize experiments that utilized the resonance to create heteronuclear molecules and ultimately a coherent superposition of atoms and molecules. At the time this work began, experiments with ultracold atomic gases at Fano-Feshbach reso-

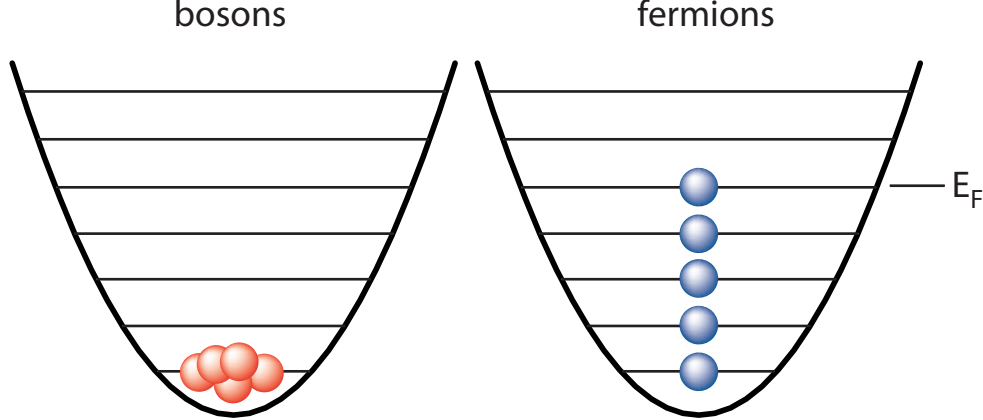


Figure 1.1: Bosons and fermions at zero temperature. Identical bosons form a BEC in which all of the particles occupy the ground state. Fermions form a Fermi sea, in which one fermion occupies each energy state up to the Fermi energy, E_F .

nances abounded and were making great headway into understanding the nature of interactions in BECs in bosonic samples [1, 2, 3, 4, 5] and exploring pairing in the BCS-BEC crossover in fermionic systems [6, 7]. Many of these single-species experiments involved the association of molecules with a Fano-Feshbach resonance [8]. There were, however, relatively few experiments exploring interactions between atoms with different nuclei at ultracold temperatures [9, 10, 11], and none had yet created heteronuclear molecules via Feshbach association. These heteronuclear experiments allow for the study of interactions between atoms with differing quantum statistics, that is, bosons and fermions and, therefore, open up a host of phenomena to study.

1.1 Fun things to do with Bose-Fermi mixtures

The Bose-Fermi mixture is more than just the sum of its parts. Alone, our spin-polarized Fermi gas is non-interacting at ultralow temperatures, while the bosons are weakly repulsive ($a_{\text{Rb}} = 98.98 a_0$) [12, 13], which leads to a stable BEC in sufficiently cold clouds. When mixed together, the interplay between the

inter- and intraspecies interactions can lead to a wide variety of phenomena. If the interspecies interaction is strong and attractive, this attraction can overcome the boson-boson repulsion and cause the system to collapse [14, 9, 15] as in the “bosenova” observed in condensates with attractive interactions [16, 17]. A strong, repulsive interspecies interaction will cause phase-separation [18, 19] in which the two species are forced to occupy physically separate regions of the trap. In between these two extremes, however, there are predicted to be some subtle and some exotic effects of the interspecies interaction.

The effective interactions between the bosons can be altered by the presence of fermions. Repulsive Bose-Fermi interactions are expected to enhance an already repulsive boson-boson interaction, resulting in a lower critical temperature for Bose-Einstein condensation, while attractive interactions should reduce the boson-boson repulsion and shift the transition to higher temperatures [20]. In highly elongated traps, changing the effective boson-boson interactions by abruptly changing interspecies interactions is expected to create two-component solitons in degenerate mixtures [21, 22, 23]. Just as the presence of fermions can alter the boson-boson interactions, the presence of the bosons can affect the fermion-fermion interactions. With strong enough interspecies interactions (of either sign), phonons in a BEC can induce an effective fermion-fermion attraction, which may lead to Cooper pairing in a Fermi gas that would otherwise be non-interacting [24, 25] or enhance the attraction of a two-component Fermi gas, resulting in an increase in the critical temperature for pairing [26, 27].

Clearly, trapped Bose-Fermi mixtures are rich physical systems to study, but the addition of a periodic trapping potential, such as an optical lattice opens up a host of additional avenues of study. The system of a Bose-Fermi mixture on a lattice is predicted to exhibit a multitude of novel phases including superfluid and insulating phases in addition to density waves and Fermi liquids [28] and in low-

dimensionality, a supersolid phase [29, 30]. Boson-mediated Cooper pairing is also expected to occur in the lattice, offering a controllable system directly analogous to superconductivity in solid-state systems, which may shed additional light on high- T_C superconductors [31, 32]. The addition of disorder to a lattice is expected to lead to Anderson-like localization of the bosons [33] and quantum spin glasses [34]. Bose-Fermi mixtures in optical lattices offer a playground for experimentalists that has only begun to be explored with observations of localization of bosons due to small impurities of fermions [35] and shifts of the Mott Insulator transition due to Bose-Fermi interactions [36].

The final exciting avenue for Bose-Fermi mixtures I will mention is the subject of this thesis—the study of heteronuclear molecules. We have used an atomic Bose-Fermi mixture to create highly vibrationally excited molecules and study quantum superpositions of atoms and molecules [37]. These superpositions may offer a probe of the many-body behavior of a strongly interacting Bose-Fermi mixture. Additionally, heteronuclear molecules can have a significant electric dipole moment when in the ro-vibrational ground state. Therefore, over the past several years, there has been much interest in transferring Feshbach molecules to their ground state to create a dense, ultracold sample of polar molecules. Such a sample was recently created by Ni *et al.* [38], which may be used as qubits in novel quantum computation schemes [39], as probes of quantum phase transitions [40], or in quantum simulations of condensed matter systems [41].

1.2 The state of affairs

In the summer of 2004, we had recently discovered four Fano-Feshbach resonances between ^{87}Rb and ^{40}K [11]. We had a ‘knob’ with which to tune the interspecies interactions and were poised to begin experiments investigating some of the phenomena discussed in §1.1 with one major technical stumbling block: low

potassium number. From day to day, we could not guarantee that we would have any potassium at the end of our evaporation, and even our best conditions left us with only 30,000 potassium atoms. This was, of course, problematic for an experiment studying interactions *between* species. This issue was exacerbated by the fact that we had few diagnostics with which to optimize the potassium number. We had fluorescence imaging of the atoms in the MOT and absorption imaging in the magnetic trap. The latter requires optically dense samples, which were only achievable in the Fermi gas near the end of evaporation. Thus, if the potassium number dropped too low or the temperature became too high, the atom gas would become too dilute and its optical depth would simply be below the noise floor of our detection during the entirety of the magnetic-trap evaporation. There are numerous steps between collection of the atoms in the MOT and evaporation to microKelvin temperatures, some of which could be optimized with fluorescence in the MOT chamber, but some steps required absorption imaging. Without a signal to optimize, we were (in)effectively shooting arrows in the dark.

The first order of business, then, was to rebuild the experiment with an eye to capturing and keeping more potassium atoms without allowing the rubidium number to suffer. Much of my thesis work has gone to building a new vacuum system and improving the many experimental steps required to create an ultracold (or even quantum degenerate) mixture of ^{87}Rb and ^{40}K . The result is a machine that over the past year has reliably generated nearly quantum degenerate mixtures with more than half a million potassium atoms and comparable numbers of rubidium atoms and allowing for the first studies of coherent oscillations between atoms and molecules in a Bose-Fermi mixture. My hope is that the machine will continue to operate stably for years to come, enabling the study of some of the other phenomena mentioned in §1.1 and possibly some yet-to-be-theorized applications of Bose-Fermi mixtures.

1.3 Atom-molecule coherence

Upon achieving the initial goal of increasing the number of atoms at the end of the experiment, we set out to study the interspecies interactions in our Bose-Fermi mixture. Our first step was to make KRb molecules from the ultracold mixture. Due to their internal atomic structure, the interactions between ^{87}Rb and ^{40}K atoms are resonantly enhanced at particular values of an externally applied magnetic field, known as Fano-Feshbach resonances [11, 42, 19]. In the vicinity of these resonances, the sign and strength of the interactions between two colliding atoms can be experimentally controlled by tuning the strength of an external magnetic field. Colliding atoms can be made to attract or repel one another or even bind together into molecules. Through precise control of an external magnetic field, we are able to transfer a mixture of ultracold atoms into weakly-bound molecules. These so-called “Feshbach molecules” are highly vibrationally excited and have sizes that are comparable to the interparticle spacing in the atomic gas. Unlike the bosonic molecules formed in single species experiments (boson + boson = boson and fermion + fermion = boson), our molecules are fermions since they are formed from the union of one bosonic and one fermionic atom. Because they are made up of two different atomic species, these molecules are expected to have an appreciable electric dipole moment when in their vibrational ground state. Recently, much work has been focused on transferring Feshbach molecules into the ro-vibrational ground state to generate an ultracold, dense sample of dipolar molecules [38, 43]. In our experiment we instead chose to study the near-threshold Feshbach molecules where we could exploit the similarities between the molecules and unpaired atoms to create coherent superpositions between atoms and molecules [44, 45, 37].

1.3.1 Quantum superpositions

In the mid-20th century, molecular beam experiments by Rabi and Ramsey demonstrated some of the earliest examples of quantum control [46, 47, 48, 49]. They showed that an oscillating magnetic field can resonantly couple two atomic states with different magnetic quantum numbers. Transitions between the two states can be induced by appropriately tuning the frequency, amplitude, and duration of the oscillating field. Additionally, applying a judiciously chosen oscillating magnetic field can result in a coherent superposition of the two quantum states, where each particle simultaneously occupies both states. This method of coupling two quantum states with oscillating fields was originally developed for the measurement of nuclear magnetic moments but has found a multitude of applications including neutron beam experiments [50], Josephson junctions in superconducting devices [51], and atomic clocks [52], to name a few. In fact, the coupling of two internal states of an atom with radio frequency (rf) or microwave photons is a tool routinely used in atomic physics experiments.

In 2002, Donley *et al.* demonstrated the first quantum superposition between atoms and molecules [44]. In this experiment, a BEC of ^{85}Rb atoms was coherently coupled to diatomic molecules, creating pairs of atoms that were both two separated atoms *and* molecules at the same time. The result was oscillations in the atom population at a frequency that corresponded to the binding energy of the molecules. Instead of coupling the atom and molecule states with an oscillating magnetic field, the superposition was created by pulsing the magnetic field to a value near a Fano-Feshbach resonance. More recently, Syassen *et al.* used a Fano-Feshbach resonance to create a quantum superposition of atoms and molecules from pairs of bosonic atoms prepared in the ground state of a tightly confining optical lattice potential [45]. Long-lived Rabi oscillations between the

atoms and molecules were observed. In more direct analogy with the experiments of Rabi and Ramsey, atoms and molecules have also been coherently coupled via two-color photoassociation in BECs [53, 54]. Each of these experiments began with identical bosons occupying a single quantum state. This circumstance leads to the question: Can an atom-molecule superposition be demonstrated with an incoherent ensemble of atoms such as non-condensed bosonic atoms, fermionic atoms [55, 56, 57], or a mixture of different atomic species [58, 59]?

1.3.2 Atom-molecule superpositions in a Bose-Fermi mixture

In the case of a Bose-Fermi mixture, the participants of an atom-molecule superposition represent three different populations with different energy distributions and quantum statistics: bosonic atoms, fermionic atoms, and fermionic molecules. Even at zero temperature the atom pairs would not occupy a single energy state due to the energy distribution of the fermionic atoms (see Fig. 1.1). The same is true of the molecules. This distribution of energies leads to a distribution of oscillation frequencies among the atom pairs in the cloud. Despite this, we have observed collective oscillations between atoms and molecules in our Bose-Fermi mixture, as will be discussed in detail in Chapter 5. These experiments represent the first observations of coherent superpositions of atoms and fermionic molecules.

1.4 Overview of this thesis

This thesis details the steps that were necessary to create and understand Feshbach molecules and superpositions of atoms and molecules in a Bose-Fermi mixture of ^{87}Rb and ^{40}K . While the basic techniques for trapping and cooling this mixture can be found in the thesis of my predecessor, Jon Goldwin [60], much of the apparatus has been upgraded and optimized. In Chapter 2, I will highlight the

main changes that enabled significant improvement in the efficiency of creating our nearly quantum degenerate mixture. This chapter is intended for the benefit of future students and post-docs working on this apparatus or someone building a similar machine.

In Chapter 3, I will discuss the Fano-Feshbach resonance, the critical tool that has enabled all of the experiments detailed in this thesis. Fano-Feshbach resonances provide the knob with which we can control the interactions between colliding atoms and allow us to coax unpaired atoms into forming molecules. They also provide the coupling between atoms and molecules that allowed for the creation of atom-molecule superpositions. In this chapter, I will introduce a simple model of Fano-Feshbach resonances and how they can be used to create molecules in general and discuss some details specific to our system.

In Chapter 4, I will outline a semiclassical Monte Carlo calculation for the association of molecules using a Fano-Feshbach resonance. This model is an extension of that used to successfully predict molecule conversion fractions in both bosonic and fermionic single-species experiments [61, 62] and bosonic heteronuclear experiments [63]. I will show that the model can also successfully account for the conversion fraction in Bose-Fermi mixtures [64] and discuss some of the parameters for optimizing the molecule fraction.

The main experimental results of this thesis are presented in Chapter 5, where I will discuss the observation of coherent atom-molecule oscillations in both Rabi- and Ramsey-type experiments. I will highlight the differences between oscillations in our system and those observed in bosonic systems and introduce potential applications of these and similar superpositions.

Chapter 6 details some predictions about the coherence times and envelopes of the atom-molecule oscillations that have yet to be tested experimentally. These predictions arise from using the Monte Carlo calculation to predict not simply

the number of molecules, but also the relative kinetic energy between the atoms that form the molecules. The results show some counter-intuitive dependences on temperature and degeneracy.

Finally, in Chapter 7, I will conclude with a summary of the work presented. I will also provide some thoughts on the goals for the experiment for the near future and possible long-term directions to follow.

Chapter 2

Experimental improvements

The apparatus used for the experiments discussed in this thesis has been described in detail in Jon Goldwin’s thesis [60]. Since 2005, we have made many improvements to the system that have allowed for efficient production of ultracold and degenerate mixtures of ^{40}K and ^{87}Rb . In this chapter, I will not describe every change that was made to the apparatus. Instead, I will begin with an overview of the experimental steps that take a room-temperature gas of free atoms to a (nearly) degenerate Bose-Fermi mixture with tunable interactions in under a minute and a half. I will then discuss in detail the changes to the experiment that brought about the most significant improvements and a few additional capabilities that have enabled the studies of Fano-Feshbach resonances and atom-molecule oscillations discussed in Chapters 3 and 5.

2.1 Experimental sequence

We begin our experiments by simultaneously collecting Rb and K atoms from a room-temperature vapor via a two-species magneto-optical trap (MOT). By overlapping the beams required for trapping Rb atoms with those for K atoms, we are able to confine the two species in roughly the same position in space. We typically trap 4×10^8 atoms in the Rb MOT and 4×10^7 atoms in the K MOT. Each species is then prepared in a single spin state ($|f = 2, m_f = 2\rangle$ for Rb, and

$|9/2, -9/2\rangle$ for K) and transferred into a quadrupole magnetic trap as discussed in detail in §2.3.2 below. Here, f is the total atomic spin, and m_f is the projection of the spin along the magnetic field. The vapor pressure in the MOT cell limits the lifetime of a trapped atom to a few seconds. To achieve longer lifetimes, we transfer the atoms to another cell, termed the “science cell”, which is connected to the MOT cell via a long (60 cm), narrow (1 cm diameter) tube. This tube allows for differential pumping between the two cells, and the lifetime of the trapped mixture can be several hundred seconds in the science cell. To transfer the atoms to the science cell, we physically move the coils that generate the quadrupole trap (a.k.a. the cart coils), which are mounted on a linear translation stage.

Once in the science cell, the atoms are transferred to a Ioffe-Pritchard (IP) type magnetic trap as detailed in §2.3.3. Here, the mixture is cooled via sympathetic cooling. That is, the Rb gas is cooled by forced rf evaporation, and the K gas is cooled by thermalizing collisions with the Rb atoms. Typically, we stop the evaporation when we reach a temperature of $2\mu\text{K}$, leaving us with 1×10^6 atoms in each species.

We use Fano-Feshbach resonances between K and Rb atoms in their lowest energy states to control the interspecies interactions (see Chapter 3). In these spin states, the atoms are not magnetically trappable. Therefore, we transfer the mixture to a far-off-resonance optical dipole trap (FORT) generated by a single focused laser beam with a $1/e^2$ radius $18\ \mu\text{m}$ and a wavelength of 1090 nm. The atoms are then transferred to the $|9/2, -9/2\rangle$ atomic Zeeman state of K and the $|1, 1\rangle$ state of Rb via rf and microwave adiabatic rapid passage, respectively.

To achieve a quantum degenerate mixture (or nearly so), the mixture must be further cooled. We simultaneously evaporatively cool the two species by decreasing the power in the optical-trap beam. This lowers the trap depth and causes high energy atoms in both species to be ejected from the trap. At the

end of the evaporation, the trap is adiabatically recompressed. At the end of this sequence, we can have a nearly pure BEC with 65,000 atoms with a degenerate Fermi gas of 180,000 atoms at 0.2 T_F , where T_F is the Fermi temperature of the K gas. However, for most of the experiments presented in this thesis, we stop the evaporation before the onset of Bose condensation to avoid the associated high densities.

During the optical trap evaporation, a nearly uniform magnetic field is applied and increased to a field near one of the Fano-Feshbach resonances (usually 542 G). The interspecies interactions can then be manipulated by varying the magnetic field around the resonance. The final properties of the atoms (number, temperature, spin state, etc.) at the end of this sequence are then measured with species-selective absorption imaging, which is discussed in §2.7.

2.2 New vacuum system

Prior to 2005, our experiments suffered from having too few K atoms at the end of the experimental sequence. From day to day, we could not guarantee that we would be left with any K atoms at the end of the IP trap evaporation, and our best conditions left us with only 30,000 K atoms loaded into the optical trap. This problem of low atom numbers at the end of the experiment was compounded by the fact that we had few diagnostics with which to optimize the K number. We were able to detect the K atoms in the MOT with fluorescence imaging, but once the atoms are transferred into the science cell, we rely on absorption imaging to detect them. This requires optically dense ensembles of atoms, and if the K number was too low or the temperature too high, the atoms would be indistinguishable from background noise in the images.

A seemingly simple solution to these problems was to increase the number of K atoms in the MOT. However, we observed little to no improvement in our

starting conditions when we tried to increase the output of our K dispensers. These dispensers, which we refer to by the unfortunate misnomer “getters”, are made in-house at JILA and are based on the design of the alkali metal dispensers from SAES Getters, Inc. [65]. The K getters contain commercially available enriched KCl (5% ^{40}K , which is large compared with the 0.012% natural abundance of the ^{40}K isotope) and calcium, a reducing agent. When current is passed through the getter, ohmic heating enables a chemical reaction that releases the K atoms from the alkali salt. Controlling the current, therefore, controls the pressure in the MOT cell, and, consequently, the number of atoms trapped by the MOT.

In the summer of 2005, we decided that we had to replace the K getters, which, of course, meant breaking vacuum. In addition to improving the K atom number and its controllability, this afforded us the opportunity to make a few improvements to the vacuum system as well. We added a gate valve in middle of the transfer tube. This enables us to break vacuum on either the MOT-cell side or the science-cell side while leaving the other under vacuum (a capability that was immediately useful!). We also swapped all the bolts along the transfer tube for higher quality 316 stainless steel bolts. The previous vacuum system had been fastened together with 304 stainless steel bolts, which are nominally nonmagnetic but were generating magnetic fields of up to 10 G. These were likely the cause of a magnetic “speed bump” over which the cart had to pass slowly to prevent severe atom loss [60]. Also, the titanium sublimation pump was moved closer to the science cell to enable more rapid pumping. Schematic drawings of the vacuum system in its current incarnation are shown in Figs. 2.1 and 2.2.

Initially, we were concerned that the Rb getters in the old system had contaminated the K getters. A new MOT cell was made with a K getter arm and two Rb ampoules instead of Rb getters. To achieve the ultralow pressures required for our experiments, we baked the entire chamber at temperatures between 200 and

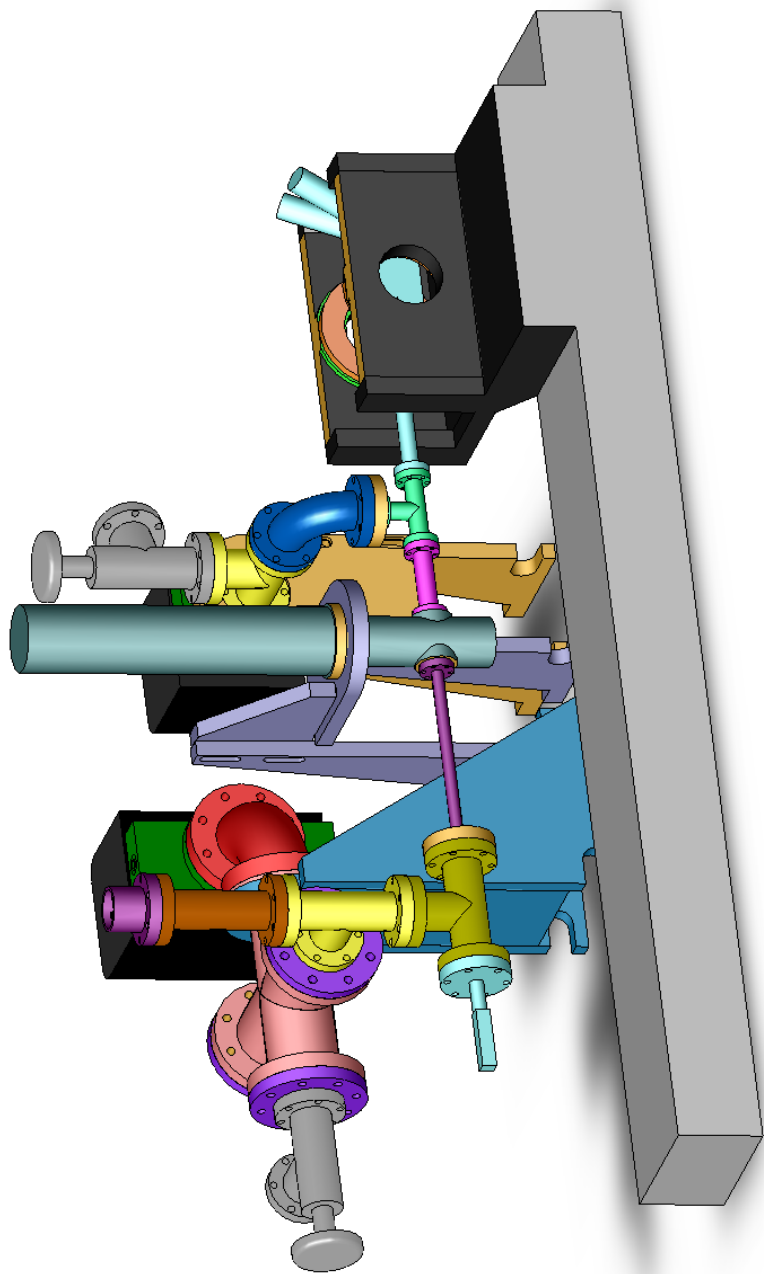


Figure 2.1: CAD drawing of the new vacuum system.

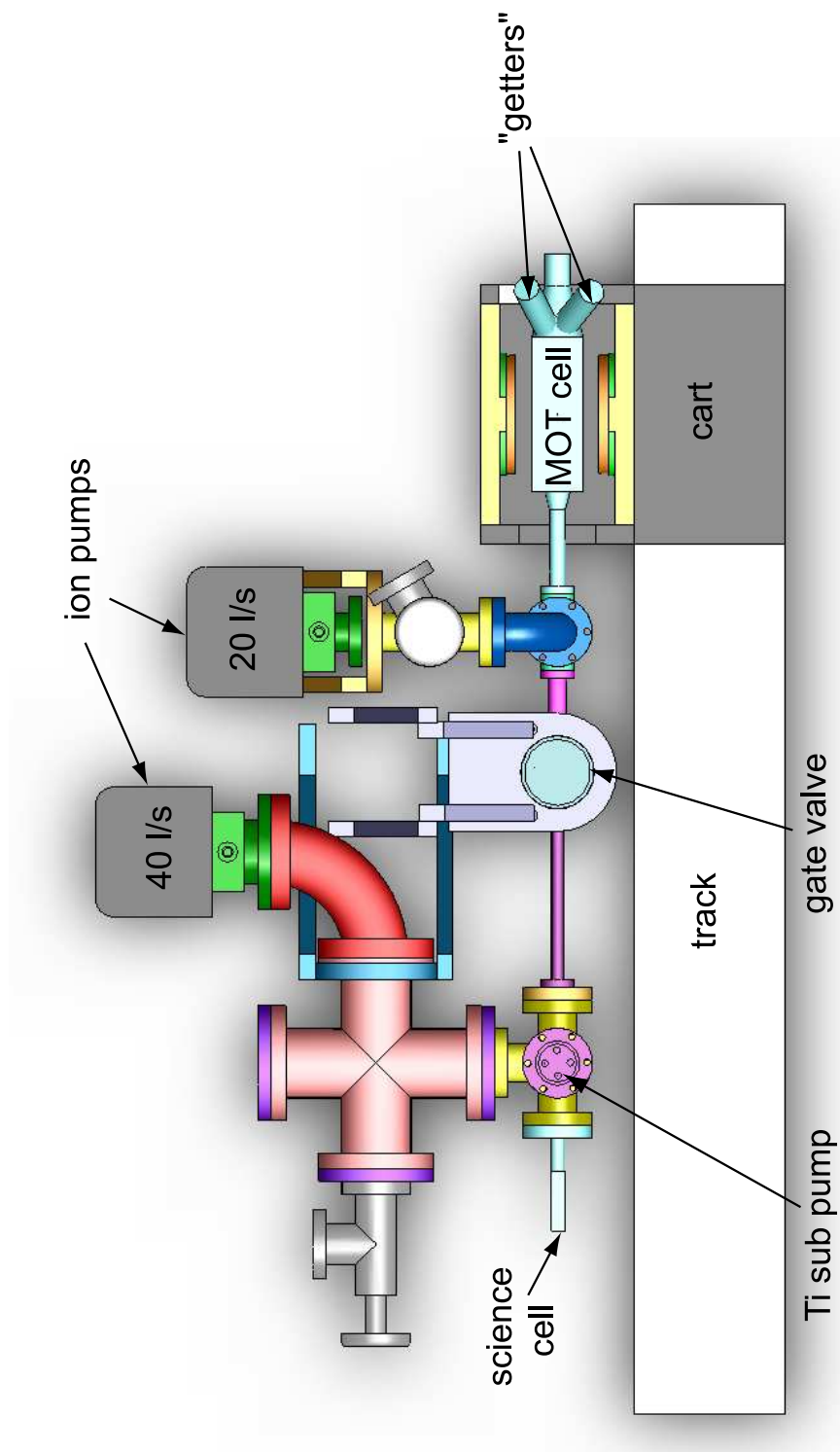


Figure 2.2: CAD drawing of the new vacuum system (top view).

350°C for 9 days. All the metal parts were wrapped with tape heaters, and an oven made from fire bricks was built around each glass cell to minimize thermal gradients. When we cooled down the system and opened the oven surrounding the MOT cell, we found that the Rb had reacted with the borosilicate glass, turning both ampoules red and causing one to rupture as shown in Fig. 2.3. During the bake, the oven temperature near the ampoules was 275°C. This corresponds to a Rb vapor pressure of 0.7 Torr [66], which is more than 3 orders of magnitude too small to break the glass. Presumably, the chemical reaction that turned the ampoules red also stressed the glass.

We promptly closed the new gate valve, which sealed off the science cell, and replaced the MOT cell with another, this time reverting to the original design of two getter arms and no ampoules. The MOT side of the vacuum chamber was then baked at 250°C for 7 days. Upon cooling the system and finding no cracks in the glass cells, we began to test our new system.

2.2.1 Large, controllable K MOTs

Since the main goal of the new vacuum system was to achieve higher numbers of atoms in the K MOT, we chose to first operate without running the Rb getters. This way, we could ensure that the K getters worked properly and that we could control the number of atoms in the MOT without having to consider the effects of another species. By controlling the current through the K getter, we were able to achieve K MOTs with 1.5×10^8 atoms with exponential fill times of 3.5 s. This is an order of magnitude improvement over the 10^7 -atom K MOTs we had worked with in the past. Satisfied that our new K getters worked and that we could trap large numbers of K atoms, we were then ready to introduce Rb into the system.

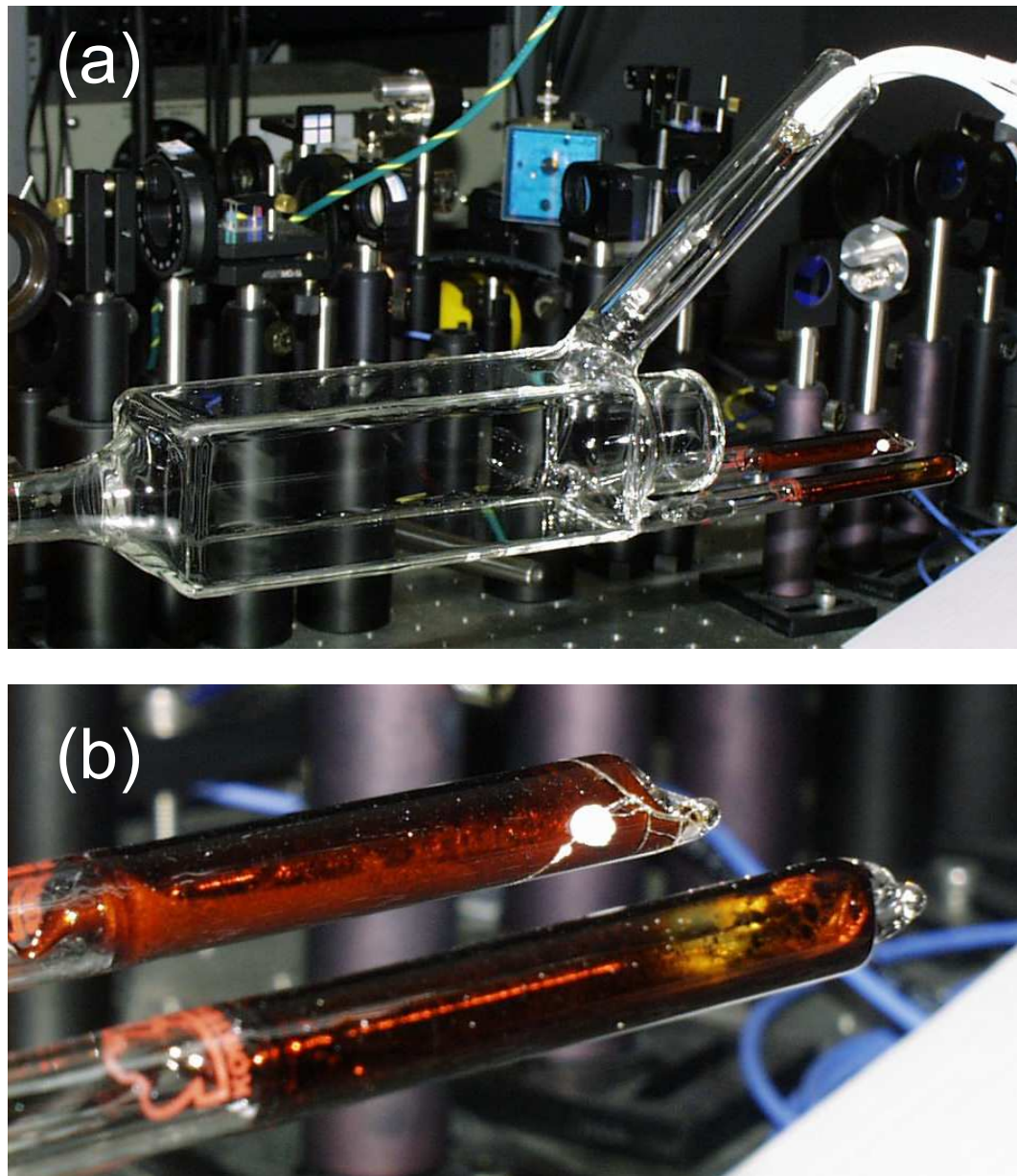


Figure 2.3: Failed MOT cell with Rb ampoules. A photograph of the MOT cell with a K getter arm and two Rb ampoules taken after baking out the vacuum system is shown in (a). The cell was baked at 275°C. (b) shows a zoomed-in view of the ampoules. The Rb has reacted with the glass, causing it to turn red. Prior to the bake, the glass was clear, and a puddle of silver Rb was visible. During the bake, one ampoule ruptured, and some Rb escaped and reacted with the oxygen in the air (white blob on upper ampoule).

2.2.2 Model of a two-species MOT

In addition to trapping large numbers of atoms in each species, we would like to independently control the population in each MOT. To do so, we must understand the behavior of the K MOT in the presence of Rb and vice versa. Here, I present a simple model of the two-species MOT to illustrate how the number of atoms in each species depends on the total pressure in the MOT cell. The model considers only elastic collisions between atoms, and, therefore, ignores the light-assisted inelastic collisions that have been observed to reduce the number of atoms in the K MOT [67].

Let us first consider each MOT individually. The number of atoms N in a single-species MOT can be described by [68]

$$\frac{d}{dt}N_i(t) = L - \Gamma N_i(t), \quad (2.1)$$

where L is the loading rate, Γ is the loss rate of atoms from the MOT, and the subscript $i = \{\text{Rb, K}\}$ represents the species of atoms in the MOT. The loading rate is proportional to the pressure of trappable atoms P_i in the cell

$$L = \alpha_i P_i. \quad (2.2)$$

Here, α_i is a proportionality constant that depends on the geometry, laser intensities, and detunings of the MOT and the species being trapped. Atom can be lost from the MOT when an untrapped atom collides with a trapped atom. Therefore, the atom loss rate depends on the total pressure [69]

$$\Gamma = \beta_i \cdot (P_i + P_{\text{bg}}), \quad (2.3)$$

where P_{bg} is the pressure of “background” atoms, i.e. all species that are not being trapped. β_i is a proportionality constant, and we have assumed that an atom is just as likely to be lost if it collides with another atom of its own species as with

any other species. In equilibrium, the number of atoms in a MOT is

$$N_i = \frac{L}{\Gamma} = \frac{\alpha_i P_i}{\beta_i \cdot (P_i + P_{bg})} = \frac{\alpha_i}{\beta_i} \frac{1}{1 + \frac{P_{bg}}{P_i}}. \quad (2.4)$$

Now, let us consider the case of ideal getters in a perfect vacuum for Rb and K, in turn. We will assume that an ideal, but unenriched Rb getter emits 3 ^{85}Rb atoms for every ^{87}Rb atom, and an ideal, 5% enriched K getter emits 19 ^{39}K (or ^{41}K) atoms for every ^{40}K atom. For the Rb MOT, $P_{bg} = 3P_{\text{Rb}}$, and for the K MOT, $P_{bg} = 19P_{\text{K}}$. Here, P_{Rb} and P_{K} are the pressures of ^{87}Rb and ^{40}K , respectively. The equilibrium number of Rb atoms in a MOT when this ideal getter is fired into a perfect vacuum is

$$N_{\text{Rb}} = \frac{\alpha_{\text{Rb}}}{\beta_{\text{Rb}}} \frac{1}{1 + \frac{3P_{\text{Rb}}}{P_{\text{Rb}}}} = \frac{1}{4} \frac{\alpha_{\text{Rb}}}{\beta_{\text{Rb}}}. \quad (2.5)$$

Likewise, firing an ideal K getter into a perfect vacuum results in

$$N_{\text{K}} = \frac{\alpha_{\text{K}}}{\beta_{\text{K}}} \frac{1}{1 + \frac{19P_{\text{K}}}{P_{\text{K}}}} = \frac{1}{20} \frac{\alpha_{\text{K}}}{\beta_{\text{K}}}. \quad (2.6)$$

For this case, in which the background pressure is proportional to the trappable atom pressure, we find the somewhat surprising result that the equilibrium atom number in the MOT is independent of pressure. To compare the number of atoms in the two MOTs, we make some assumptions about the proportionality constants α_i and β_i . First, we assume the probability that a collision with a background atom ejects a trapped atom from the MOT is the same for the two species, i.e. $\beta_{\text{Rb}} = \beta_{\text{K}} = \beta$. Next, we will assume that the loading of the Rb MOT is 3 times more efficient than the K MOT¹, so $\alpha_{\text{Rb}} = 3\alpha_{\text{K}} = 3\alpha$. The number in each MOT, then, is

$$N_{\text{Rb}} = \frac{3}{4} \frac{\alpha}{\beta} \quad \text{and} \quad N_{\text{K}} = \frac{1}{20} \frac{\alpha}{\beta}. \quad (2.7)$$

¹ This assumption is based on the empirical observation that K MOTs trap fewer atoms than Rb MOTs with similar intensities, detunings, and geometries.

In this idealized case, we find the total number of Rb atoms is fifteen times larger than the number of K atoms, due to the relative fraction of trappable atoms.

Now, let us consider a more realistic case: ideal getters fired into an imperfect vacuum with an initial pressure P_{vac} . For now, we will still consider each species individually. We find the equilibrium number of atoms in each MOT is

$$N_{\text{Rb}} = \frac{3\alpha}{\beta} \frac{P_{\text{Rb}}}{P_{\text{Rb}} + 3P_{\text{Rb}} + P_{\text{vac}}} = \frac{\alpha}{\beta} \frac{3}{4 + \frac{P_{\text{vac}}}{P_{\text{Rb}}}} \quad (2.8)$$

$$N_{\text{K}} = \frac{\alpha}{\beta} \frac{P_{\text{K}}}{P_{\text{K}} + 19P_{\text{K}} + P_{\text{vac}}} = \frac{\alpha}{\beta} \frac{1}{20 + \frac{P_{\text{vac}}}{P_{\text{K}}}}. \quad (2.9)$$

The number of atoms in each MOT multiplied by β/α is plotted as a function of the trappable atom pressure in Fig. 2.4. Not surprisingly, we see that the number in the K MOT is lower than in the Rb MOT. We also see that the number in both species reach 90% of the maximum number at the same total pressure. Due to the output of the getters, the partial pressure at this saturation point is 5 times lower for K than Rb.

Now, let us consider the two-species MOT, in which the number in each species depends on the outputs of both getters. Now, P_{Rb} and P_{K} are partial pressures. The background pressure for the ^{87}Rb MOT is made up of everything that is not ^{87}Rb , $P_{\text{bg}} = P_{85\text{Rb}} + P_{40\text{K}} + P_{39\text{K}} + P_{\text{vac}} = 3P_{\text{Rb}} + 20P_{\text{K}} + P_{\text{vac}}$, and the background pressure for the ^{40}K MOT is $P_{\text{bg}} = P_{85\text{Rb}} + P_{87\text{Rb}} + P_{39\text{K}} + P_{\text{vac}} = 4P_{\text{Rb}} + 19P_{\text{K}} + P_{\text{vac}}$. Now, the number in each species is

$$N_{\text{Rb}} = \frac{3\alpha}{\beta} \frac{P_{\text{Rb}}}{P_{\text{Rb}} + 3P_{\text{Rb}} + 20P_{\text{K}} + P_{\text{vac}}} = \frac{3\alpha}{\beta} \frac{1}{4 + \frac{20P_{\text{K}} + P_{\text{vac}}}{P_{\text{Rb}}}} \quad (2.10)$$

$$N_{\text{K}} = \frac{\alpha}{\beta} \frac{P_{\text{K}}}{P_{\text{K}} + 19P_{\text{K}} + 4P_{\text{Rb}} + P_{\text{vac}}} = \frac{\alpha}{\beta} \frac{1}{20 + \frac{4P_{\text{Rb}} + P_{\text{vac}}}{P_{\text{K}}}}, \quad (2.11)$$

as shown in Figs. 2.5 and 2.6. Running either of the getters will increase the number of atoms in the corresponding MOT but will decrease the number of atoms in the other MOT. This is because running the Rb getter increases the background

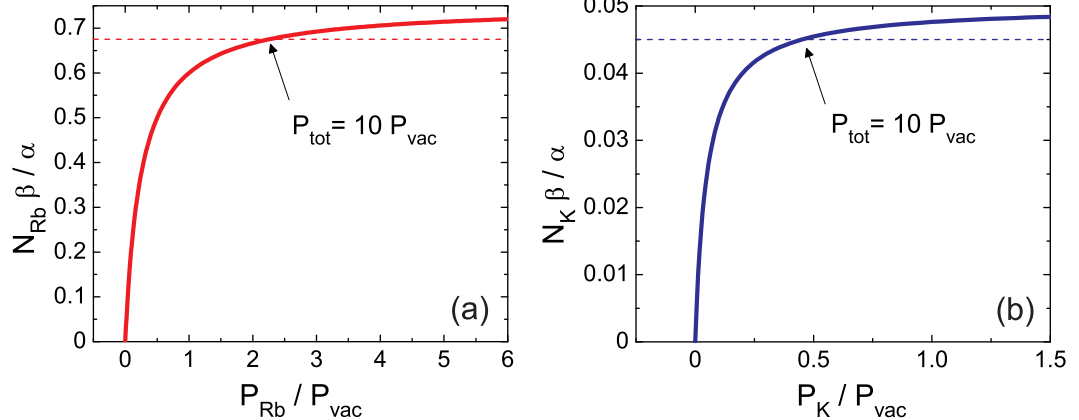


Figure 2.4: Pressure dependence of single-species MOT numbers. The number of ^{87}Rb atoms in the MOT multiplied by β/α as a function of the ^{87}Rb partial pressure P_{Rb} scaled by the initial pressure P_{vac} is shown in (a). A similar plot for a ^{40}K MOT is shown in (b). The dashed lines represent 90% of the maximum number of atoms in the MOTs, which differ by a factor of 15 between the two species. Both species reach 90% of the maximum when the total pressure is 10 times the initial pressure, but the partial pressure of trappable atoms differs due to the output of the “ideal” getters as described in the text.

pressure for the K MOT and vice versa. Even in this idealized illustration, controlling the number of atoms in each MOT requires striking a balance between the partial pressures of Rb and K.

In the experiment, this situation is further complicated. Josh Zirbel and coworkers demonstrated that the K getters have a small (200 ppm) Rb contamination [70]. This has a negligible effect on daily operation, but we have found that over time, both getters become contaminated, presumably due to atom adsorption. Running either getter releases both Rb and K. Figure 2.7 shows the number of atoms in each species as a function of pressure when running a 5-A current through only the K getter. The number of K atoms follows the expected dependence, but we would expect a decrease in the number of Rb atoms as in the top plot in Fig. 2.5. Instead, both increase, indicating that both K and Rb are being released. This may indicate that the current running through the K getter

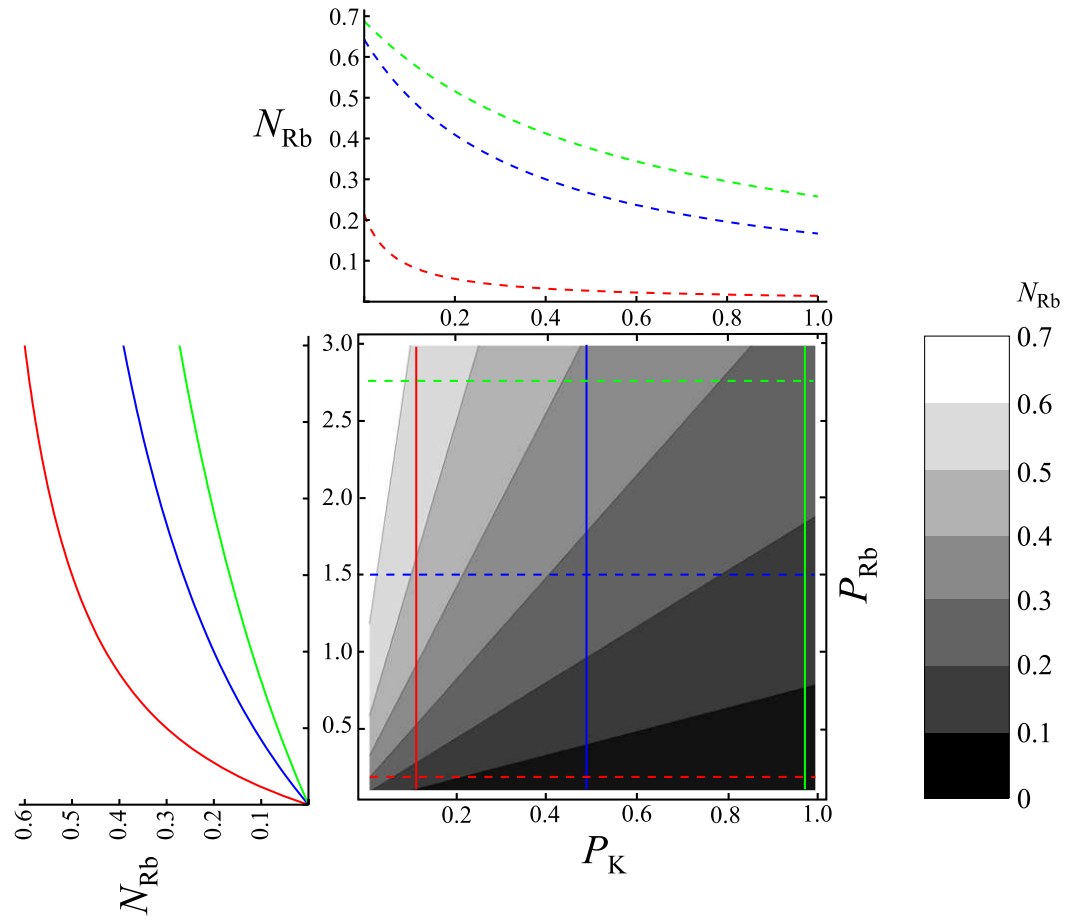


Figure 2.5: Dependence of the Rb MOT number on the partial pressures of Rb and K. The contour plot shows the number of atoms in the Rb MOT N_{Rb} scaled by β/α calculated with Eq. 2.10 as a function of the partial pressures of ^{87}Rb and ^{40}K , P_{Rb} and P_{K} in units of P_{vac} . The left-hand plot shows N_{Rb} as a function of the Rb pressure for fixed K pressures, corresponding to the vertical lines on the contour plot. The top plot shows N_{Rb} as a function of the K pressure for fixed Rb pressures, corresponding to the horizontal lines on the contour plot.

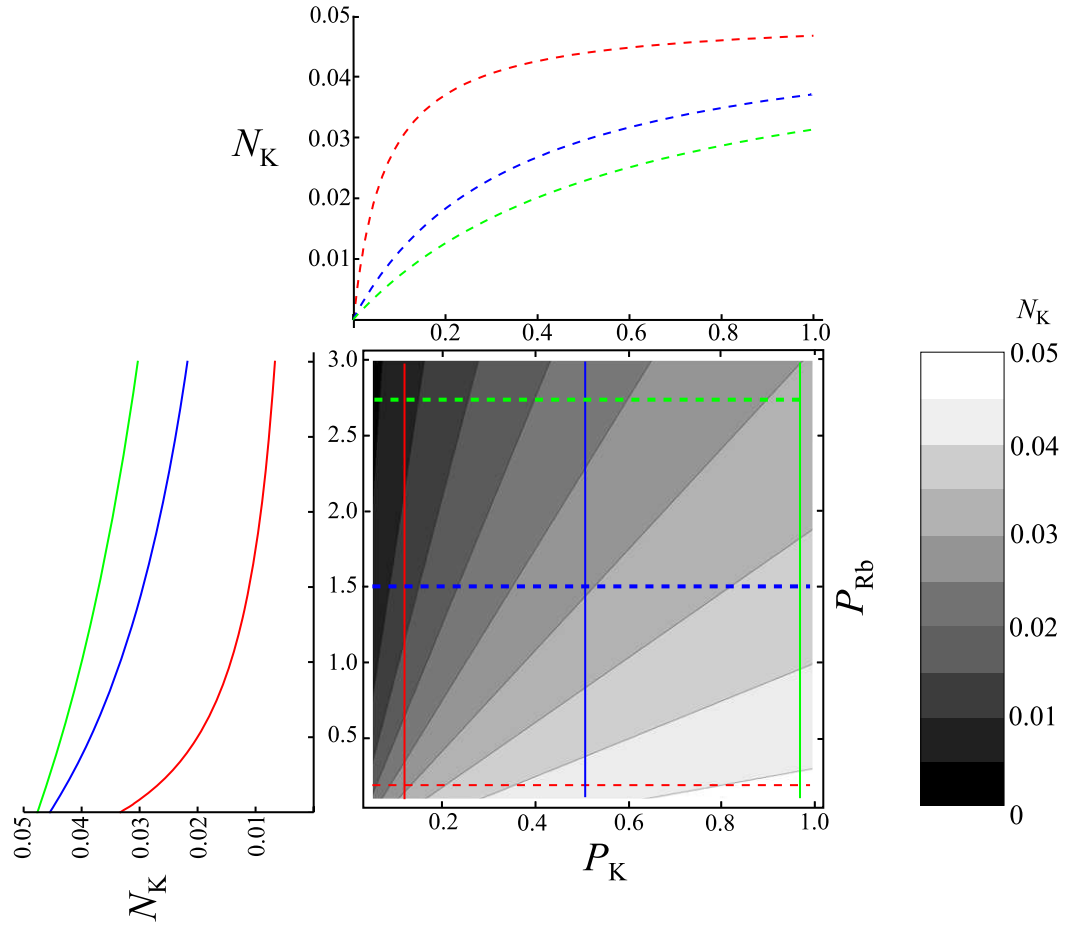


Figure 2.6: Dependence of the K MOT number on the partial pressures of Rb and K. The contour plot shows the number of atoms in the K MOT N_K scaled by β/α calculated with Eq. 2.11 as a function of the partial pressures of ^{87}Rb and ^{40}K , P_{Rb} and P_K , in units of P_{vac} . The left-hand plot shows N_K as a function of the Rb pressure for fixed K pressures, corresponding to the vertical lines on the contour plot. The top plot shows N_K as a function of the K pressure for fixed Rb pressures, corresponding to the horizontal lines on the contour plot.

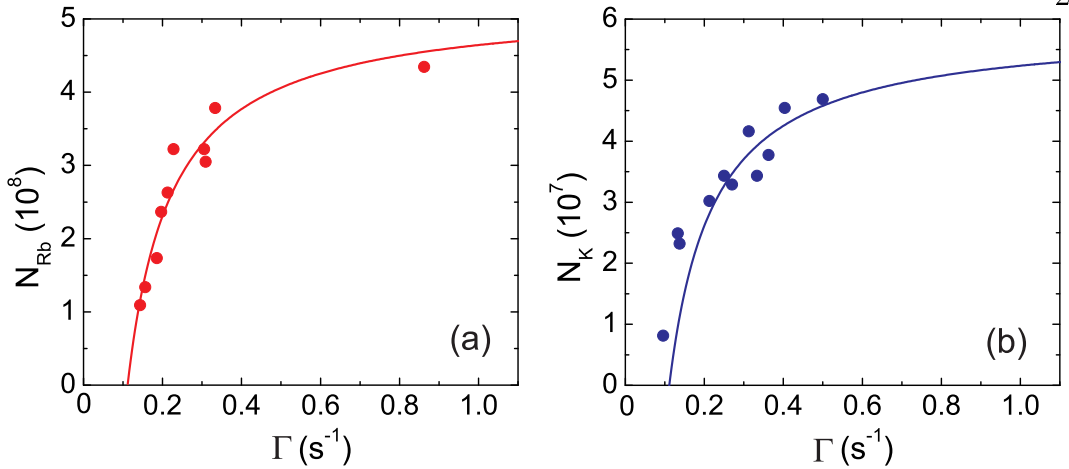


Figure 2.7: Measured MOT numbers running only the K getter. The numbers of atoms in the Rb (a) and K (b) MOT are plotted as a function of the exponential fill rate Γ , which is proportional to the total pressure. The pressure is varied by running a current of 5 A through the K getter for varying durations. Contrary to the expectation of the model presented in the text, the number in both MOTs increase with increasing pressure, indicating that both species are released by the K getter. The lines are the result of a simultaneous fit to the data to $N = N_{\max} \frac{\Gamma - \Gamma_{\text{bg}}}{\Gamma}$, which is equivalent to Eq. 2.4 with $N_{\max} = \alpha/\beta$ and $\Gamma_{\text{bg}} = \beta P_{\text{bg}}$. The fit yields a background fill time of $1/\Gamma_{\text{bg}} = (9 \pm 2)$ s and a maximum number of $N_{\max} = (5.2 \pm 0.3) \times 10^8$ atoms in the Rb MOT and $(5.9 \pm 1.1) \times 10^7$ atoms in the K MOT.

does not heat the getters enough to induce the chemical reactions that should preferentially release K, but instead only heats the assembly enough to release adsorbed atoms. Higher currents (> 6.2 A) are necessary to release enough K to visibly coat the glass getter arm.

In the experiment, we typically operate with 4×10^8 atoms in the Rb MOT and 4×10^7 atoms in the K MOT with exponential fill times of $1/\Gamma = 2.5$ s. We achieve these conditions by pulsing on the Rb getter at 4.5 A for 90 s each morning. To maintain a steady pressure throughout the day, we run 3.75 A through the K getter with the Rb getter off. The K getter is turned off at night to extend its life.

2.3 Keeping all those atoms

Having achieved our goal of increased K atoms in the MOT, we wanted to ensure that the improved initial conditions would translate to larger numbers at the end of the experiment. This meant minimizing losses in the experiment, with particular emphasis on the transfer of the atoms between the various traps. In this section, I describe three important improvements that allowed us to maintain the larger K numbers throughout the experiment.

2.3.1 Fiber coupling the MOT light

To trap atoms in the MOTs, we use two frequencies of laser light for each species. The “trap light” is red detuned of the $f = 9/2 \rightarrow f' = 11/2$ transition in ^{40}K and the $f = 2 \rightarrow f' = 3$ transition in ^{87}Rb , while the “repump light” is red detuned of the $f = 7/2 \rightarrow f' = 9/2$ and $f = 1 \rightarrow f' = 2$ transitions (see Fig. 2.8). To improve the quality of our MOT beams, we have fiber coupled the K and Rb trapping beams as well as the Rb repumping beam as shown in Fig. 2.9. Previously, we had used a single tapered amplifier to amplify all of the beams and found that the K and Rb light emerged with different divergences, making it impossible to efficiently fiber couple both colors. The amplifier for the K light is now unnecessary, because enough power for trapping the K atoms is generated by a 120-mW injection-locked laser [70]. The Rb and K beams are coupled into a single fiber, and we are able to achieve 70% and 50% efficiency for the K and Rb light, respectively. This scheme delivers 140 mW of Rb light (5% repump), 45 mW of K trap light, and 17 mW of K repump light to the 3-beam retro-reflected MOT.

Because the fiber-coupled MOT beams have Gaussian profiles, ease of alignment and its reproducibility have improved. More importantly, though, the

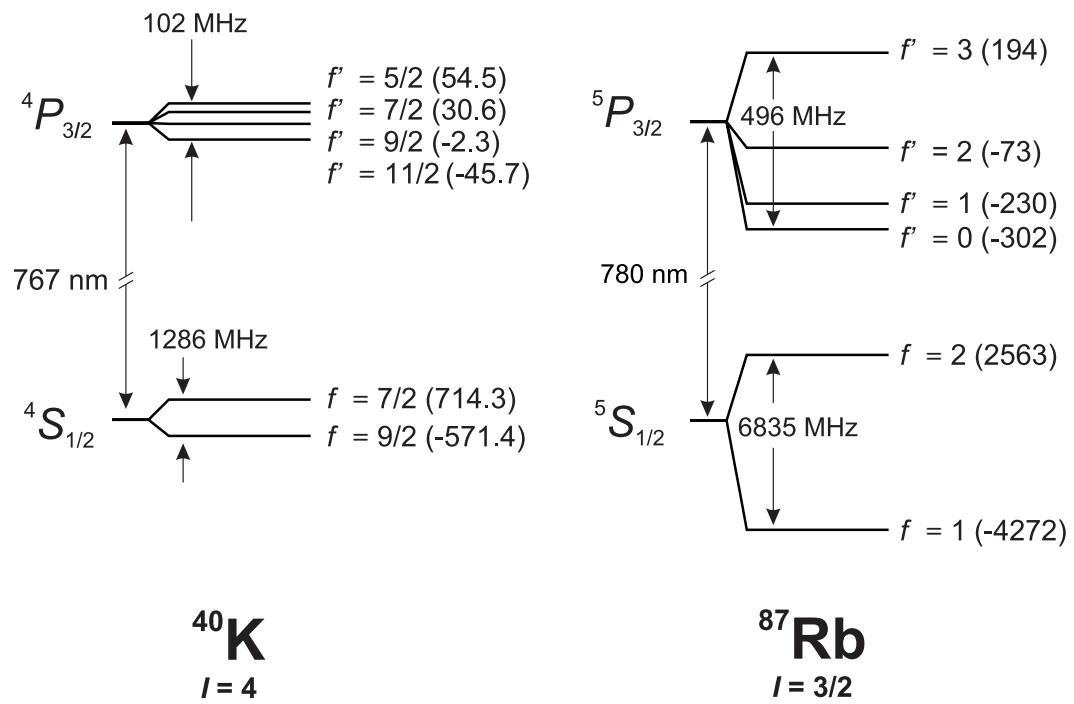


Figure 2.8: Hyperfine structure of the relevant ground and excited states of ^{40}K and ^{87}Rb with the splittings calculated from Ref. [71].

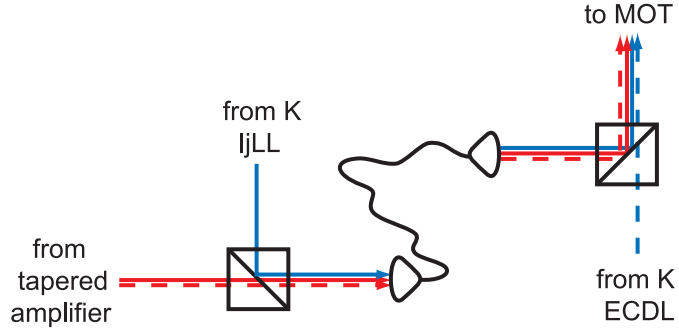


Figure 2.9: Fiber coupling the MOT light. The red lines represent the Rb trap and repump beams. The Rb beams emerge from a tapered amplifier and are combined with the K trap beam (solid blue line), which is generated by an injection-locked laser (IjLL). All three beams are coupled into the same fiber, and the output is directed toward the MOT after combining with the K repump beam (dashed blue line) which is generated by an external cavity diode laser (ECDL).

structure-free beams allow for lower temperatures and purer spin compositions in the quadrupole trap. Ideally, we would like to load cold, spatially small, and spin-polarized clouds into the quadrupole trap. The Rb MOT, however, is large in spatial extent due to strong radiation trapping [72]. A spatially large cloud will gain excess potential energy when transferred to the quadrupole trap, which will result in a higher temperature gas in the trap. To reduce the size of the Rb cloud, we apply a compressed MOT stage, or CMOT, in which we reduce the intensity of the repumping beam for 50 ms [73, 60]. Before the MOT beams were fiber coupled, we found that the positions of the MOT, CMOT, and quadrupole trap differed, presumably due to structure in the MOT beams. In transferring from one stage to the next, the atoms acquired additional kinetic energy due to the shifting trap centers, negating some of the benefits of the CMOT. Now, we find the traps are well overlapped, eliminating heating due to excess motion.

In addition to an improved CMOT stage, the Gaussian MOT beams have enabled the incorporation of a polarization gradient cooling stage, or optical molasses, for the Rb atoms [74]. For the molasses, the MOT magnetic-field gradient

is abruptly switched off, the Rb trap light frequency is shifted 40 MHz red of the cycling transition, and the MOT shim fields are changed. The shim fields are tuned by watching the expansion of the Rb MOT in real time using a small CCD camera hooked up to a TV monitor. The fields are set so the MOT expands slowly and uniformly over several seconds. In the experiment, however, the duration of the molasses stage is only 2 ms. Figure 2.10 shows a measurement of the relative temperature of the Rb atoms with and without the molasses stage. The atoms are loaded into a variable strength quadrupole trap, held in the trap for 400 ms, and recaptured into the MOT. The fraction recaptured is determined by comparing the measured MOT fluorescence before and immediately after the hold in the quadrupole trap. An atom with zero velocity will be trapped when the trapping force of the quadrupole field overcomes the force of gravity. Atoms with larger velocities (higher temperatures) will require greater trapping forces.

We can compare the fraction of atoms held by the quadrupole trap as a function of the trap strength to a simple model that calculates the fraction of atoms with energies less than the trap depth for a cloud with a given temperature. We assume the trap depth U for a given atom is given by

$$U = \mu\beta\frac{W}{2} - mg\frac{W}{2}, \quad (2.12)$$

where μ is the magnetic moment of the atom, m is the mass of the atom, β is the magnetic-field gradient, g is the acceleration due to gravity, and W is the width of the cross-sectional width of the MOT cell. We also assume that the momentum distribution of atoms in the MOT is given by

$$n(p) = \frac{N}{(2\pi m k_b T)^{3/2}} e^{-p^2/(2m k_b T)}, \quad (2.13)$$

where N is the number of atoms in the MOT, T is the temperature, and k_b is the Boltzmann constant. For an atom to be trapped by the quadrupole trap, we

require

$$\frac{p^2}{2m} \leq \frac{U}{2}, \quad (2.14)$$

which arises from the Virial Theorem for a linear trap (potential energy = $2 \times$ kinetic energy). We can compare the measured MOT recapture fraction to the calculated fraction of atoms that satisfy Eq. 2.14 to estimate the temperature and spin purity (see §2.3.2) of the cloud loaded into the quadrupole trap. Using the model, we estimate a temperature of $300 \mu\text{K}$ without the molasses and a temperature of $200 \mu\text{K}$ after the molasses stage. Applying the model to data taken before the MOT beams were fiber coupled indicates temperatures as high as $600 \mu\text{K}$. Therefore, by fiber coupling our MOT light, we were able to make a factor of 3 improvement in the temperature of the atoms loaded into the quadrupole trap.

After the CMOT and molasses stages, the atoms are cold ($\leq 200 \mu\text{K}$) but in a somewhat random distribution of spin states. Before loading the atoms into the quadrupole trap, we add a stage of optical pumping to spin-polarize each species as discussed below. Note that an optical pumping pulse has been applied the data shown in Fig. 2.10.

2.3.2 Spin state purification

Ideally, we would like to load the quadrupole trap with a pure sample of Rb atoms in the $|2, 2\rangle$ state and K atoms in the $|9/2, 9/2\rangle$ state. Any other mixture of spin states will be able to undergo spin-flip transitions that can heat the mixture and expel atoms from the trap. Because we load 10 times more Rb than K atoms into the quadrupole trap, we have strict requirements on the spin purity of the Rb atoms. A 10% spin impurity in Rb could obliterate the entire K population. To prepare as pure a sample as possible, after the molasses stage, optical pumping light is applied to both species for $<1 \text{ ms}$. A combination of repumping light and

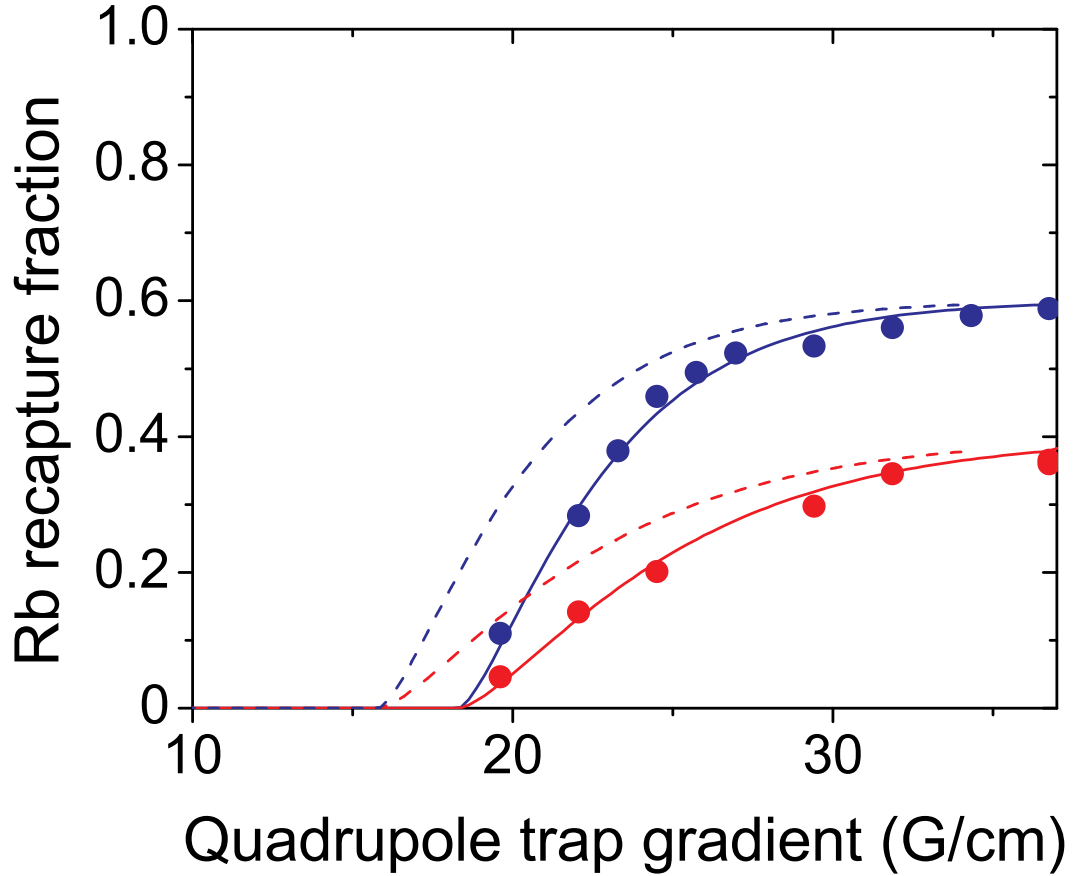


Figure 2.10: Effect of optical molasses on the temperature of the Rb MOT. Plotted is the fraction of Rb recaptured into the MOT after a 400 ms hold in the quadrupole trap as a function of the trap gradient. The atom clouds represented by the red points are loaded into the quadrupole trap after the CMOT stage. The blue points show atom clouds that have been further cooled by a 2 ms optical molasses, resulting in a steeper onset of trapping. The dashed lines are the result of a simple model for the fraction of atoms that can be trapped in the quadrupole trap. The blue line is the expected fraction for a 200 μK cloud with 80% of the atoms in the $|2, 2\rangle$ state, while the red line is for a 300 μK cloud with 50% of the atoms in the $|2, 2\rangle$ state. The solid lines are the dashed lines shifted by 2.5 G/cm to match the data. This shift may be due to an additional field, such as a MOT shim that is kept on during the transfer. All the curves have been scaled by 75% to account for the lifetime in the quadrupole trap.

Zeeman pumping light (σ^+ polarized light on the $f = 2 \rightarrow f' = 2$ Rb transition and $f = 9/2 \rightarrow f' = 9/2$ K transition) transfers the atoms into the stretched states. Since the different spin states have different magnetic moments, they require different quadrupole trap strengths to be trapped. Therefore, the method of measuring the fraction of atoms recaptured from varying strength traps can be used to measure the efficiency of the optical pumping in addition to monitoring the temperature of the cloud. Figure 2.11 compares the fraction of Rb atoms recaptured into the MOT with and without optical pumping as a function of trap strength. The Rb $|2, 2\rangle$ atoms have a magnetic moment of $\mu = \mu_B$ and can be trapped at 16 G/cm, while Rb $|2, 1\rangle$ and $|1, -1\rangle$ atoms have a magnetic moment $\mu = \frac{1}{2}\mu_B$ and require gradients greater than 32 G/cm. Here, μ_B is the Bohr magneton. Without optical pumping, all the Rb spin states are populated, and we see two clear steps as atoms with the different magnetic moments become trapped. We estimate that after optical pumping, more than 90% of the captured Rb atoms are in the $|2, 2\rangle$ state. The efficiency of the optical pumping is likely limited by the optical depth of the gas. Note that the data in Fig. 2.10 indicate that the optical pumping efficiency increases after the molasses stage, which is likely due to the decrease in optical depth of the expanded gas.

The Rb recapture data shown in Fig. 2.11 suggest an additional mechanism for further purifying the spin mixture, which was first implemented by Scott Papp [75]. By loading the atoms into a quadrupole trap with a gradient < 32 G/cm, only atoms in the $|2, 2\rangle$ state can be trapped. In the experiment, we load the atoms into a trap with a gradient of 29 G/cm in the vertical direction, wait 400 ms to ensure that unwanted spin states fall out of the trap, then increase the trap strength to 98 G/cm for the transport along the vacuum system. While the initial trap filters out all but one spin state of Rb, 7 spin states of K can be trapped. Thus, we must rely solely on optical pumping to purify the K atoms. However,

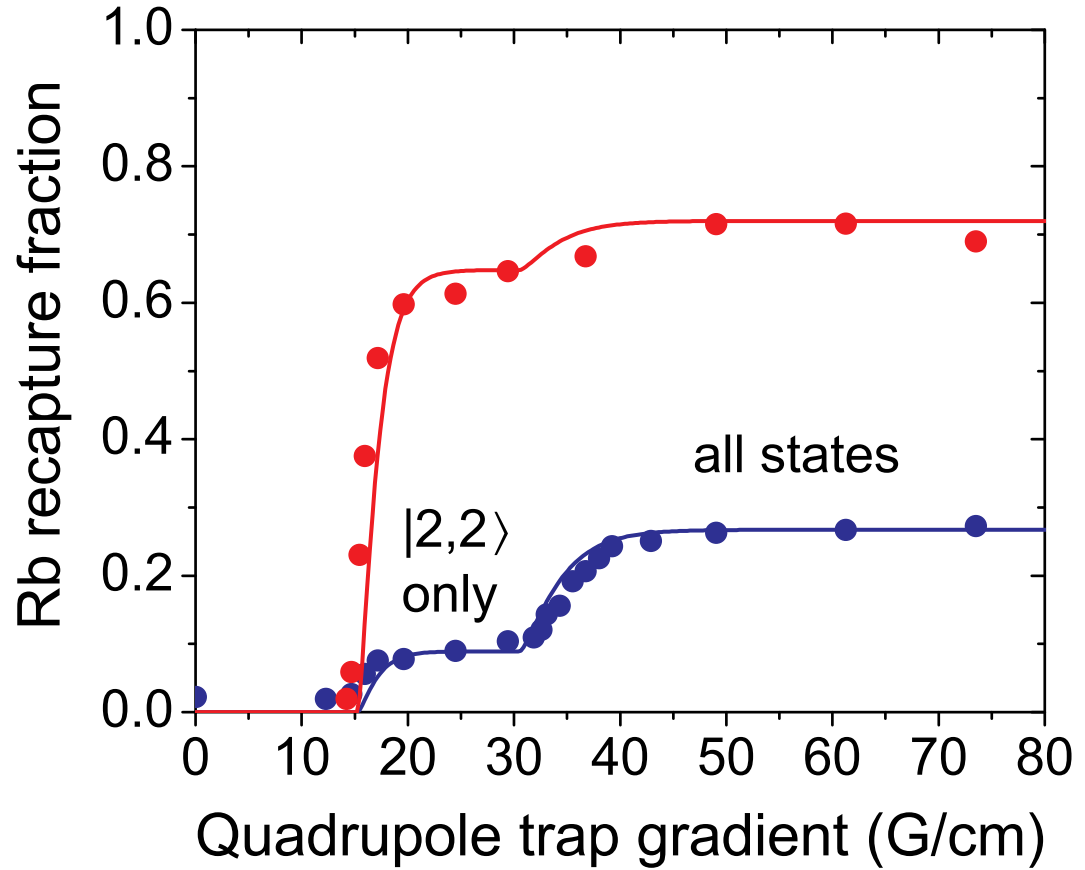


Figure 2.11: Rb spin states loaded into the quadrupole trap. The fraction of Rb atoms recaptured into the MOT after a 400-ms hold in the quadrupole trap as a function of the trap gradient is plotted for atoms clouds with (red points) and without (blue points) optical pumping. The curves are the results of a model for the atom fraction loaded into the quadrupole trap for a temperature of 100 μK and scaled by 77% to account for the lifetime in the quadrupole trap. Without optical pumping, the majority of the atoms are not in the desired $|2, 2\rangle$ state. With optical pumping, 90% of the atoms are in the $|2, 2\rangle$ state. Therefore, there is only a small increase in the recaptured fraction above 32 G/cm, the gradient at which $|2, 1\rangle$ and $|1, -1\rangle$ atoms begin to be trapped.

a small impurity in the K spin mixture will result in correspondingly small atom losses.

Because it is sensitive to temperature, spin state, and number, this technique of measuring the fraction of atoms recaptured from the quadrupole trap has proved to be a crucial tool for optimizing the initial stages of the experiment. For example, we are able set the duration of the optical pumping pulse so that each species is well polarized but the temperature is not increased. We are also able to ensure that the molasses reduces the temperature of the Rb gas without sacrificing atoms in either species. As a result, we are able to load into the quadrupole trap a spin-polarized gas comprised of > 70% of the atoms in the Rb MOT and > 60% of the atoms in the K MOT at a temperature of 100 μK .

2.3.3 Quadrupole trap to IP trap transfer

One point in the experiment where we are particularly susceptible to atom loss is in the transfer from the quadrupole trap to the IP trap. As shown in Fig. 2.12, the shapes of equilibrium clouds in the two traps are severely mismatched. In the quadrupole trap, the cloud is shaped like an $m\&m$, while in the IP trap, it is cigar-shaped. Because the cloud is initially too large in the radial direction and too small in the axial direction, if we abruptly turn off the quadrupole trap and turn on the IP trap, breathe modes are induced along three dimensions. While we cannot tighten the IP trap along the axial direction, we can weaken the confinement in the radial direction to make a round(ish) trap. By increasing the final trap strength of the quadrupole trap, we are able to match the radial cloud sizes in the traps, eliminating radial breathing. However, we are still left with a sizable mismatch along the axial dimension of the traps. When a cloud is loaded into the IP trap, the axial size begins to breathe about the equilibrium size in the IP trap (axial rms size, $\sigma_z = 1.3$ mm). If the atoms are too energetic, they

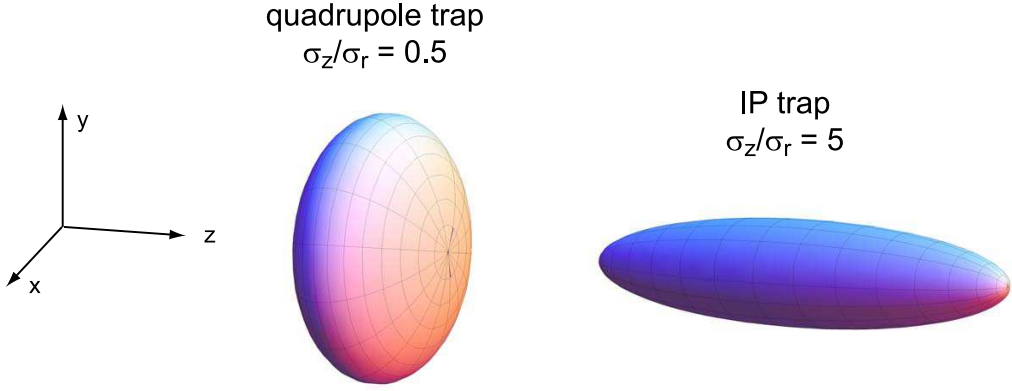


Figure 2.12: Schematic of the cloud shapes in the quadrupole and Ioffe-Pritchard traps. The traps are both cylindrically symmetric about the same axis, but differ by a factor of 10 in aspect ratio (σ_z/σ_r).

will splatter onto the science cell walls, which are only 5 mm away from the trap center ($< 4\sigma_z$). Figure 2.13 shows the measured fraction of Rb atoms transferred into the IP trap as a function of temperature. To calculate the expected fraction transferred to the IP trap, we use a model similar to that described in §2.3.1. We calculate the fraction of atoms whose energy is less than the trap depth of the IP load trap set by the science cell walls. The data show reasonable agreement with this simple model of the transfer and demonstrate nearly 100% transfer with our coldest clouds. Once the atoms are transferred, we increase the radial confinement to the full trap strength with a 5:1 aspect ratio. Figure 2.14 shows the current through the quadrupole and IP traps for the optimized transfer.

2.4 Too much of a good thing?

All our efforts to improve the K number in the early stages of the experiment led to a significant increase in the number of K atoms loaded into the IP trap. Prior to the new vacuum system, we could not measure the number of atoms in

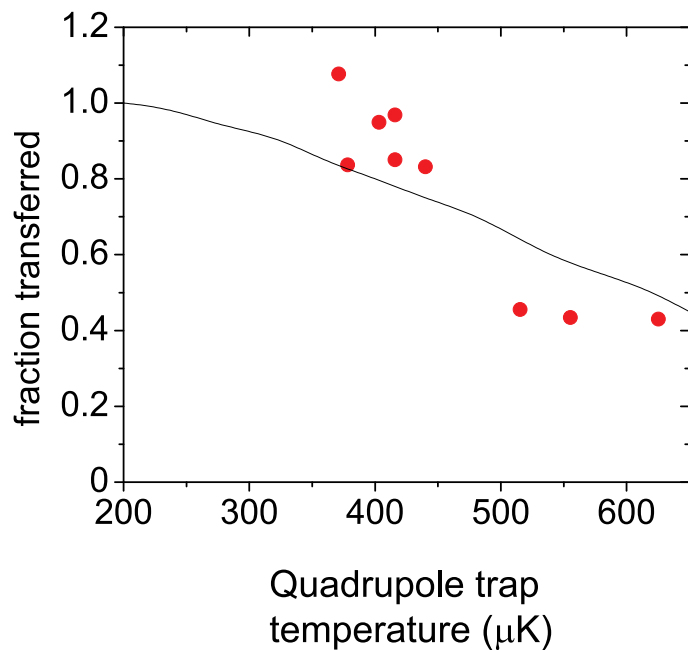


Figure 2.13: Temperature dependence of the fraction of atoms transferred to the IP trap. The measured fraction of Rb atoms transferred from the quadrupole trap to the compressed IP trap is plotted as a function of the temperature in the 400 A quadrupole trap (Q-trap). The solid line is the result of a model of the transfer.

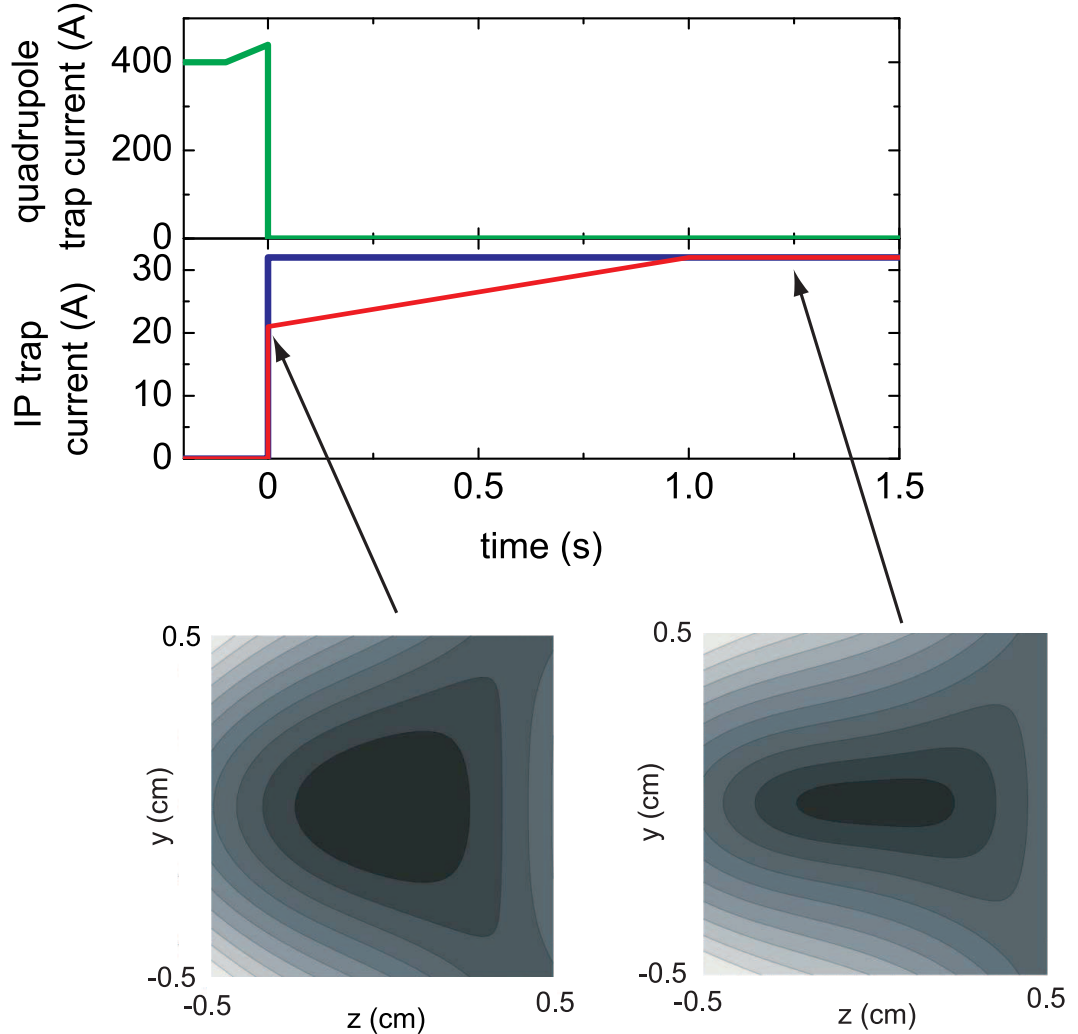


Figure 2.14: Quadrupole to IP trap transfer. Plotted are the currents for the optimized transfer from the quadrupole trap to the IP trap. The quadrupole trap current I is increased to decrease the radial size of the cloud before the transfer. The gradient of the quadrupole trap in the axial direction is equal to $I \times 0.49\text{G}/(\text{cm A})$. The IP trap is rounded by “bleeding” current from the IP bias coils (see Fig. 2.17). The red curve shows the current passing through the bias coils, while the blue curve shows the current passing through the IP radial and pinch coils. The lower plots show calculated magnetic-field contours of the initial IP trap (left) and the trap after compression (right) for $x = 0$.

the K cloud with absorption imaging until it was cooled below $10 \mu\text{K}$. Now, we are able to image the K cloud immediately after loading into the IP trap and at any time during the subsequent evaporation. We estimate that this corresponds to at least a factor of 5 increase in the optical depth of the K cloud loaded into the trap, and if we assume the K cloud is in thermal equilibrium with Rb, that translates to at least a factor of 5 more K atoms. Beyond the improvement in the number, an important consequence is that we are now able to probe both species at every stage of the experiment.

With such a plethora of K to play with, it seemed the world was our oyster. Soon, however, we encountered a new problem that had previously been inconceivable: too much K. Sympathetic cooling of the K atoms relies on the heat capacity of the Rb gas being greater than that of the K gas [76, 77]. Away from quantum degeneracy in both species, the heat capacity is given by $C_i = k_B N_i$, where k_B is the Boltzmann constant and N_i is the number of atoms in species $i = \{\text{K}, \text{Rb}\}$. This implies that the number of Rb atoms must be greater than the number of K atoms for efficient cooling. Figure 2.15 shows the number of atoms in each species as a function of the temperature before and after the experimental improvements detailed above. Here, we see clearly the increase in the K number. At $1 \mu\text{K}$, the K number is more than 10 times higher in the “After” plot than in the “Before”. Before the improvements, the low K number allowed the Rb to reach quantum degeneracy before the evaporation became inefficient. Now, the Rb evaporation efficiency begins to sharply decrease around $3 \mu\text{K}$, where the number of atoms in the two species become equal. At $3 \mu\text{K}$, both clouds are well above quantum degeneracy with $T/T_F = 2$ and $T/T_C = 6$. Here, T_F is the Fermi temperature for the K atoms and T_C is the critical temperature for Bose-Einstein condensation of the Rb atoms.

Most of our experiments require the atom gases to be quantum degenerate

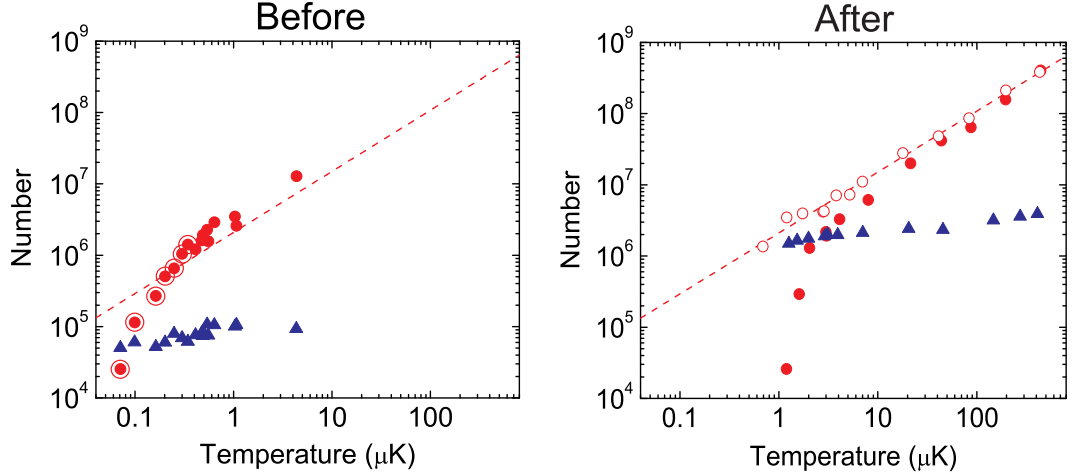


Figure 2.15: Evaporation in the magnetic trap. The two plots show the number of atoms N as a function of temperature T before and after the experimental improvements detailed in §2.2 and 2.3. The open red circles in the “After” plot show the number of Rb atoms when no K atoms are loaded into the trap (“Rb only”), while the filled red circles represent the Rb number in the presence of K (filled blue triangles). The filled circles with rings in the “Before” plot indicate that the Rb gas is a BEC. The dashed line is a fit of the “Rb only” data in the “After” plot to $N = A \left(\frac{T}{\mu K} \right)^b$ and is plotted in the “Before” plot for ease of comparison. The fit yields $A = (2.1 \pm 0.3) \times 10^6$ and $b = 0.86(2)$.

or nearly so. To achieve a more degenerate mixture, after evaporating to a few microKelvin in the magnetic trap, we transfer the atoms to a far-off-resonance optical dipole trap. This trap is generated by a single focused laser beam with a $1/e^2$ radius of $18 \mu m$ and a wavelength of $1090 nm$. By decreasing the power of the optical-trap beam, we simultaneously evaporate both species. This eliminates the heat capacity limitations imposed by sympathetic cooling, and we only require thermalizing interspecies collisions to keep the K cloud in thermal equilibrium. Thus, in the optical trap we are able to achieve quantum degenerate mixtures. Figure 2.16 shows time-of-flight absorption images of a nearly pure Rb BEC with 6.5×10^4 atoms and a K cloud of 1.8×10^5 atoms at $T/T_F = 0.2$ released from the same trap. Here, we determine T/T_F from a surface fit to a Thomas-Fermi distribution [78].

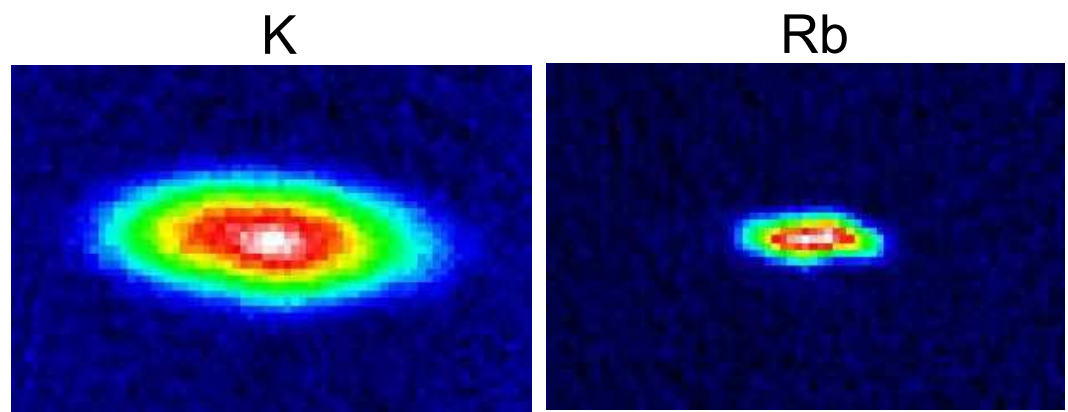


Figure 2.16: False-color absorption images of a degenerate Fermi gas and a Bose-Einstein condensate. The left image shows a cloud of 1.8×10^5 K atoms at $0.2 T_F$ after 10 ms of expansion from the optical trap. The right image shows a Rb BEC with 6.5×10^4 atoms after 20 ms of expansion. The calculated radial trap frequencies are 290 and 180 Hz for K and Rb, respectively, and the calculated axial frequencies are 3.1 and 1.6 Hz.

All of the experimental improvements detailed above have allowed us to achieve quantum-degenerate Bose-Fermi mixtures in the optical trap. However, for the experiments discussed in the rest of this thesis, we evaporate to temperatures slightly above T_C to avoid the high Rb atom densities that accompany the BEC transition.

2.5 Magnetic-field curvature compensation

In this and the following sections, I will discuss several new capabilities that were added to the experiment for the purpose of studying atoms and molecules near KRb Fano-Feshbach resonances. These include improved control over the homogeneity of the magnetic field, the ability to rapidly varying the strength of the field, and the ability to detect the atoms and molecules near the resonances.

Accessing the KRb Fano-Feshbach resonances requires large magnetic fields (> 450 G). We generate these fields with the cart coils with the direction of the current through one of the coils reversed from the quadrupole trap configuration. Because the coils are not in a proper Helmholtz configuration (where the radius of the coils is equal to their separation), the field is not uniform, but has a minimum in the axial direction. This is problematic for two reasons: (1) the Fano-Feshbach resonances we use are between high-field-seeking atomic states of Rb and K, and if the anti-trapping force of the magnetic field overwhelms the trapping force of the optical trap, which can occur during evaporation, the atoms are ejected from the trap. (2) Observing atom-molecule oscillations with long coherence times requires the magnetic field to be uniform across the atom/molecule cloud (see Chapter 5).

To cancel the curvature of this bias field, we apply an additional field generated by the axial coils of the Ioffe-Pritchard trap. The IP coils generate a field in opposition to that from the cart coils. Since the curvature depends on the current through the coils, an appropriately chosen current will cancel the magnetic-field

curvature, as shown in Fig. 2.17. Figure 2.18 shows the measured magnetic field along the axial direction of the cloud for 376 A through the cart coils and 4.76 A through the IP pinch and bias coils. The current through the IP coils was empirically optimized to minimize the magnetic-field variation across the atom cloud. The gradient implies that the IP and cart coils' fields are not centered on one another in one or more directions. Perfect cancellation requires the fields from the two sets of coils to be perfectly centered on one another in three dimensions, and we have found that the centers are offset by 1.1 mm in the vertical direction. Efforts are currently under way to correct this and achieve more uniform magnetic fields.

2.6 Fast magnetic-field pulse circuit and eddy current correction

Many of our experiments, particularly those discussed in Chapter 5, require rapid variations in the magnetic field near the Fano-Feshbach resonances. The cart coils that primarily generate the magnetic field have large inductances and are controlled by a servo with a bandwidth of 500 Hz. To achieve fast magnetic field ramps, we have installed a low inductance auxiliary coil pair controlled by a high-bandwidth servo. Two 1-inch diameter, single-loop coils separated by 32 mm are mounted concentrically with the IP axial coils. These auxiliary coils are connected to a capacitor charged to high voltage by a 160-V power supply as shown in Fig. 2.19 [3]. The auxiliary coils can generate a field of up to 50 G for 5 ms, and the bandwidth of the servo allows for magnetic-field ramp durations as short as 5 μ s. When added to the field generated by the cart coils, the auxiliary coils can generate rapid magnetic-field sweeps in the vicinity of the Fano-Feshbach resonances.²

² Note that the auxiliary coils also add inhomogeneity to the total magnetic field which must be compensated for with the IP axial coils as above, but this correction was neglected in the past.

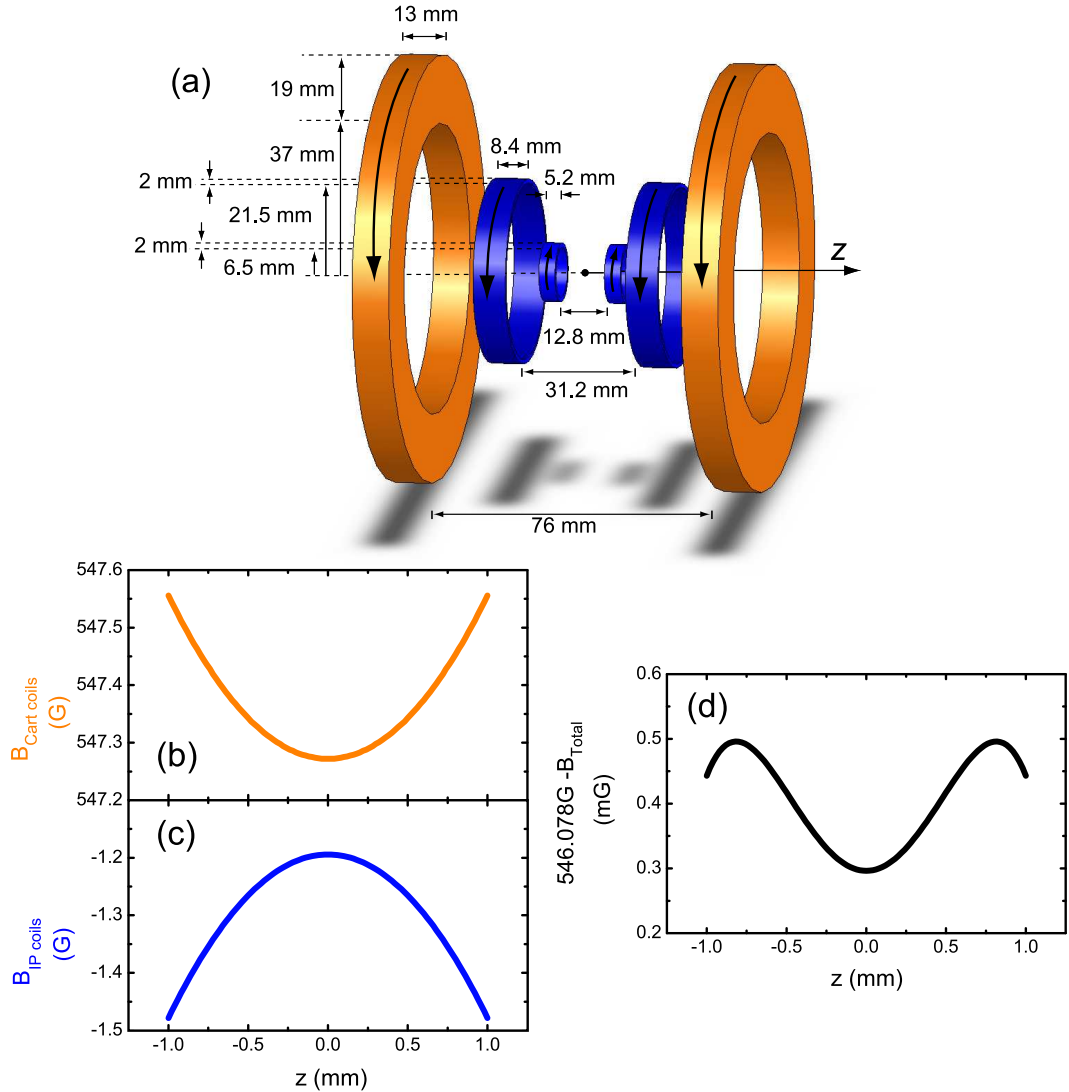


Figure 2.17: Magnetic-field curvature cancellation. A schematic of the coils used to generate a nearly uniform magnetic field is shown in (a). The cart coils, shown in orange, generate a large field with a small curvature. The axial coils of the Ioffe-Pritchard (IP) trap, shown in blue, generate a field with the opposite curvature. The magnetic field along the axis of the coils for the cart coils (calculated for a current of 388 A) and the IP axial coils (4.56 A) are shown in (b) and (c), respectively. The total field (assuming that the field centers are perfectly overlapped) is shown in (d). Notice the different scale. The current through the IP coils was chosen to minimize the magnetic-field variation over ± 1 mm. With this cancellation method, the magnetic-field variation can in principle be reduced to 0.2 mG. A typical rms cloud size along z at the end of evaporation in the optical trap is 200 μ m.

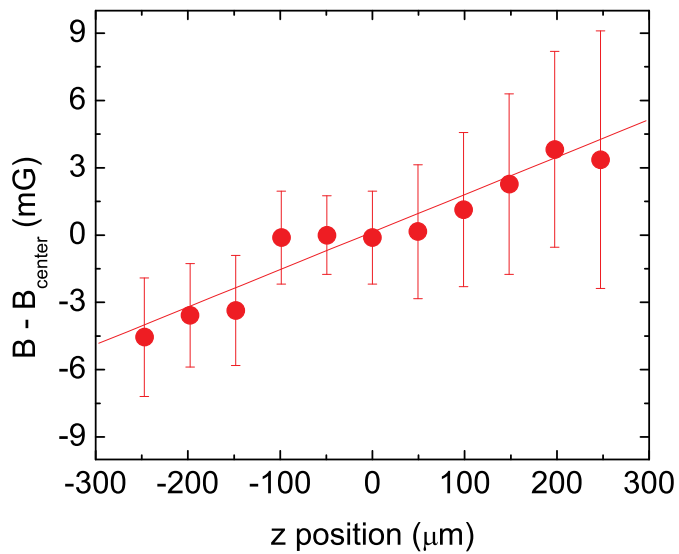


Figure 2.18: Measured axial magnetic-field inhomogeneity. The magnetic field along the axial direction of the cloud is measured using rf on the Rb $|1, 1\rangle \rightarrow |1, 0\rangle$ Zeeman transition for currents of 376 A through the cart coils and 4.76 A through the IP pinch and bias coils. The line is a linear fit to the data, yielding a gradient of 0.17 ± 0.7 G/cm.

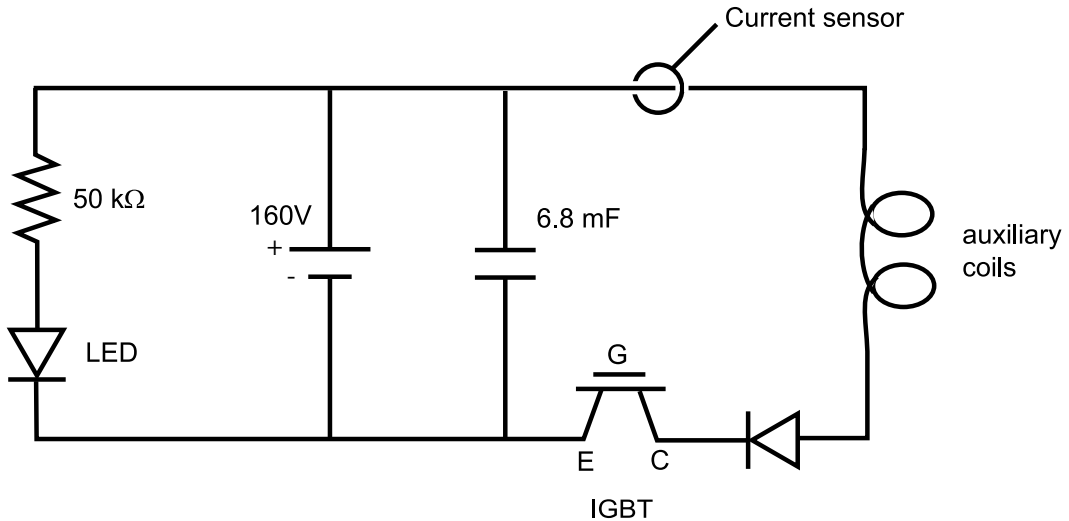


Figure 2.19: Circuit used to generate fast magnetic-field ramps. A Hall effect current sensor (Danfysik Ultrastab 866) monitors the current, and an insulated gate bipolar transistor, or IGBT, (Powerex CM200HA-24H) controls the current through the auxiliary coils.

Figure 2.20 shows a magnetic-field ramp generated by the auxiliary coils determined from the measured current through the coils. The calculated ramp rate is $5.5 \text{ G}/\mu\text{s}$. However, the actual magnetic-field ramp rate is much slower due to induced eddy currents. Figure 2.21 shows the total magnetic field after a downward magnetic-field ramp spanning 7.4 G with a modest ramp speed of $7.6 \text{ G}/\text{ms}$. At the end of the ramp, the expected change in magnetic field is undershot by nearly 20%, and the field takes more than 5 ms to decay to the correct value. We believe this deviation is due to eddy currents induced in the copper forms that house the IP coils. Such large eddy fields were unacceptable for nearly all of the experiments discussed in this thesis, particularly the atom-molecule oscillation experiments discussed in Chapter 5, which require precisely controlled fields with ramp speeds nearly 20 times faster. While replacing the IP trap forms with others made of non-conducting material may be an option for the future, we chose to actively compensate for the eddy currents with the current through the auxiliary

coils.

We model the eddy currents with a RL circuit that couples to the auxiliary coil circuit through a mutual inductance as shown schematically in Fig. 2.22. The magnetic flux through the eddy current circuit (right-hand circuit in Fig. 2.22) is given by

$$\Phi_2 = I_1 M_{21} - I_2 L_2, \quad (2.15)$$

where M_{21} is the mutual inductance, I_1 is the current through the auxiliary coils, and I_2 is the current through the eddy circuit. By applying Faraday's Law and Kirchhoff's Law to the eddy current circuit, we find

$$I_2 R_2 + \mathcal{E}_2 = I_2 R_2 - \frac{d\Phi_2}{dt} = I_2 R_2 + L_2 \frac{dI_2}{dt} - M_{21} \frac{dI_1}{dt} = 0. \quad (2.16)$$

The magnetic fields produced by each circuit are proportional to their respective currents ($B_1 = C_1 I_1$ and $B_2 = C_2 I_2$). Thus, we can recast Eq. 2.16 in terms of the magnetic fields as

$$\frac{R_2}{L_2} B_2 + \frac{dB_2}{dt} = \eta \frac{dB_1}{dt}, \quad (2.17)$$

where $\eta = \frac{C_2 M_{12}}{C_1 L_2}$. We can determine η and L_2/R_2 from measurements similar to that shown in Fig. 2.21.

For a linear ramp of the auxiliary magnetic field, the solution to Eq. 2.17 for the induced field is given by

$$B_2(t) = (B_2(0) - \zeta) e^{-t/\tau} + \zeta, \quad (2.18)$$

where the exponential decay time is $\tau = L_2/R_2$ and $\zeta = -\tau \eta \frac{dB_1}{dt}$. If $B_2(0)$ is zero, which can be ensured in the experiment, then ζ is the amplitude of the undershoot of the field. We find that η is 0.295 ± 0.011 .

By solving Eq. 2.17 over an entire ramp sequence, we can engineer the current in the auxiliary coils such that the auxiliary field and the eddy field sum to the desired ramp as shown in Fig. 2.23. The measured magnetic field and

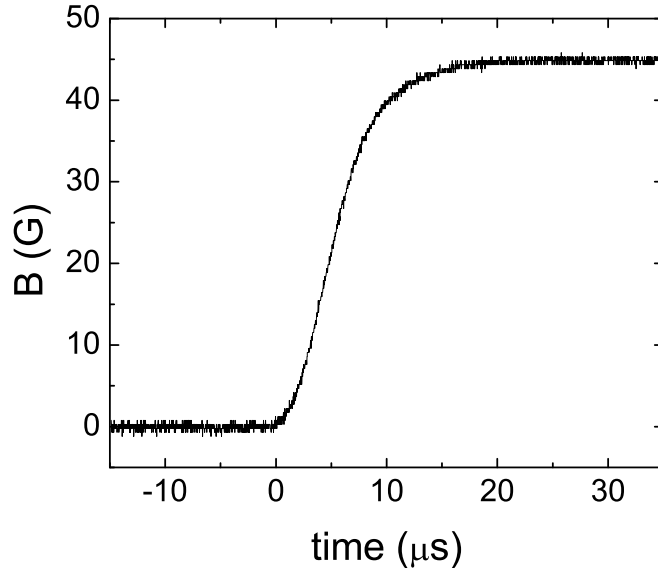


Figure 2.20: Magnetic-field ramp determined from the current through the auxiliary coils. The current implies a magnetic-field ramp rate of $5.5 \text{ G}/\mu\text{s}$.

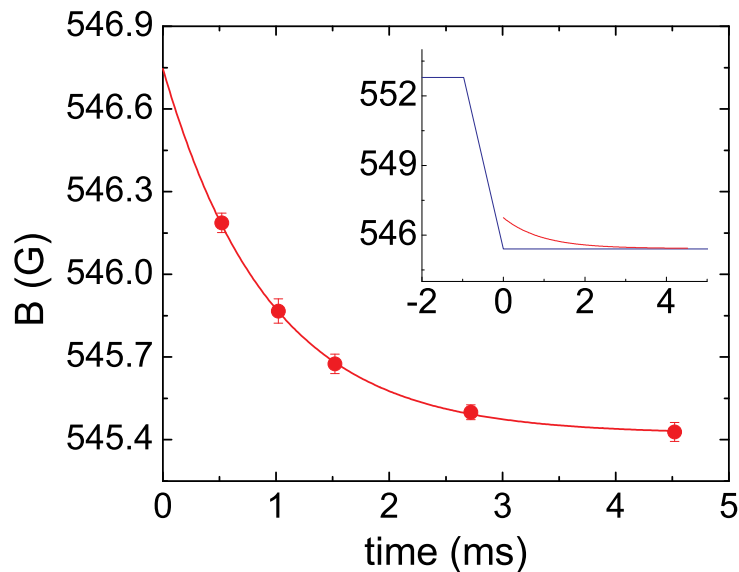


Figure 2.21: Decaying magnetic field after a magnetic-field ramp. The total magnetic field at the atoms, measured with rf π -pulses on the Rb $|1, 1\rangle \rightarrow |1, 0\rangle$ atomic Zeeman transition, is plotted as a function of time after the end of a $7.6 \text{ G}/\text{ms}$ ramp with the auxiliary coils. The red line is a fit to a decaying exponential $B = A \cdot e^{-t/\tau} + B_f$, yielding an undershoot of $A = (1.35 \pm 0.03) \text{ G}$ and a decay time of $\tau = (0.92 \pm 0.03) \text{ ms}$. The inset compares the fit to the expected magnetic-field ramp, shown in blue.

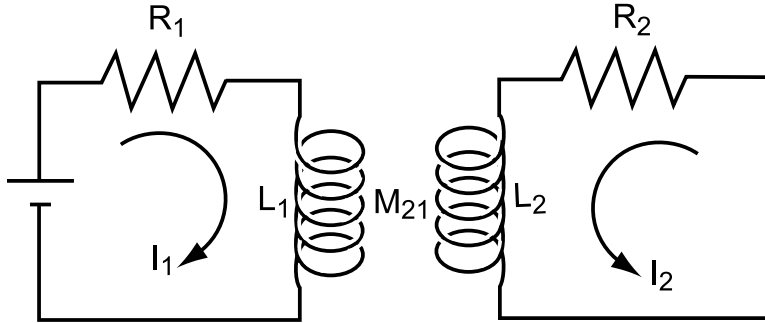


Figure 2.22: Schematic of the eddy current model. The left-hand circuit represents the auxiliary coil circuit shown in detail in Fig. 2.19, which is coupled to the eddy current circuit (right-hand circuit) by the mutual inductance M_{21} . Shown is the direction of the induced current I_2 for decreasing auxiliary-coil current I_1 ($\frac{dI_1}{dt} < 0$).

deviation from the desired 7.6 G/ms ramp with the eddy current compensation are shown in Fig. 2.24. During the entirety of the ramp, the magnetic field is within 80 mG of the expected field, and after the ramp ends, the field settles to within 20 mG of the final value in only 50 μs . When we perform ramps with speeds of 140 G/ms, we measure additional eddy fields that decay with a timescale of 90 μs as shown in Fig. 2.25. We model and correct for these smaller and faster eddy fields in the same manner and find the coupling parameter η to be 0.090 ± 0.005 . Figure 2.26 shows the calculated magnetic field for these fast ramps. With both levels of eddy current correction in place we are able to engineer ramps that span 2.4 G with speeds of 140 G/ms to within 35 mG of the desired fields as shown in Fig. 2.27.

2.7 High-field absorption imaging

While the fluorescence from atoms in the MOT is a useful diagnostic for calculating the number and temperature of the atoms in the MOT cell as discussed above (see §2.3.2), once the atoms leave the MOT cell, we rely on absorption imaging to extract information about the clouds. Detailed discussions of ab-

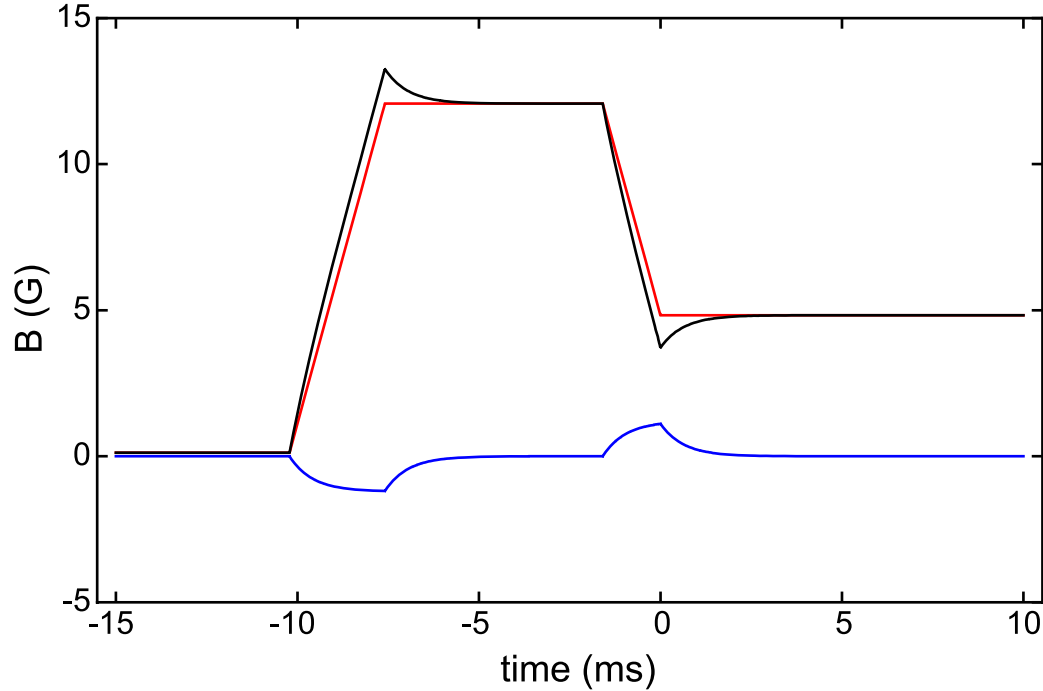


Figure 2.23: Magnetic-field ramps that compensate for eddy fields. The black curve shows the calculated auxiliary magnetic field that cancels the induced eddy field (blue line) to generate a trapezoidal ramp of the total field (red line).

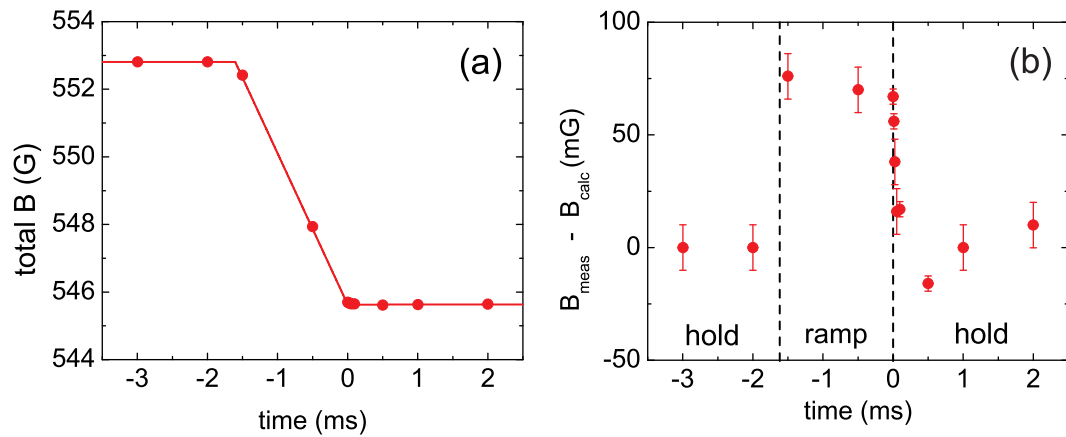


Figure 2.24: Magnetic-field ramps with eddy current compensation. The measured total magnetic field (\bullet) and the calculated magnetic-field ramp (red line) are shown as a function of time in (a). The difference between the measured and calculated field is shown in (b). The dashed vertical lines represent the hinge points of the ramp.

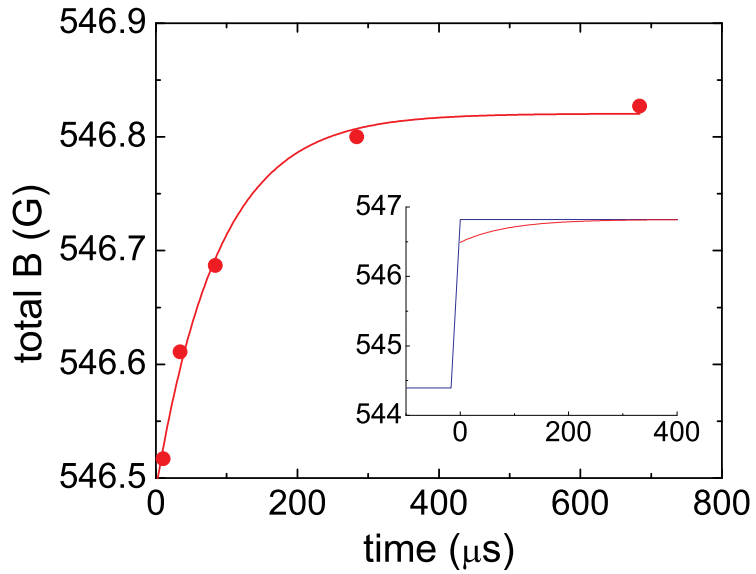


Figure 2.25: Decaying magnetic field after a fast magnetic-field ramp. The total magnetic field at the atoms, measured with rf π -pulses on the Rb $|1, 1\rangle \rightarrow |1, 0\rangle$ atomic Zeeman transition, is plotted as a function of time after the end of a 140 G/ms ramp with the auxiliary coils. The red line is a fit to a decaying exponential $B = A \cdot (1 - e^{-t/\tau}) + B_f$, yielding an undershoot of $A = (310 \pm 20)$ mG and a decay time of $\tau = (90 \pm 10)$ μs . The inset compares the fit to the expected magnetic-field ramp, shown in blue.

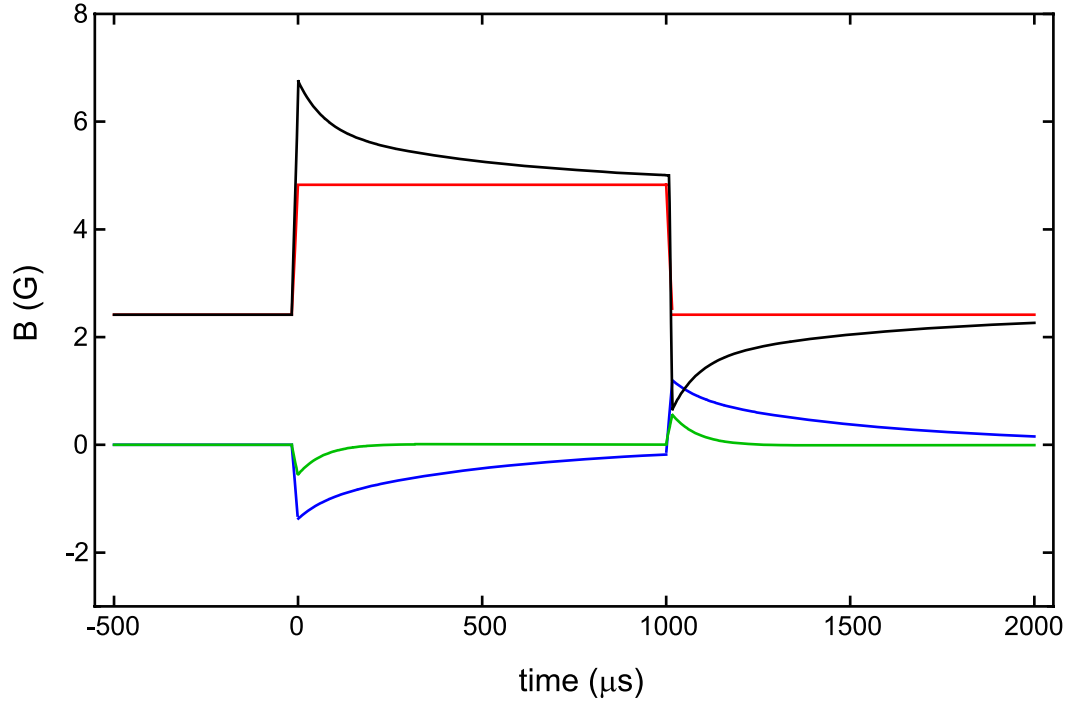


Figure 2.26: Magnetic-field ramps that compensate for eddy fields. The black curve shows the calculated auxiliary magnetic field that cancels the sum of the induced eddy fields (blue and green lines) to generate a trapezoidal ramp of the total field (red line).

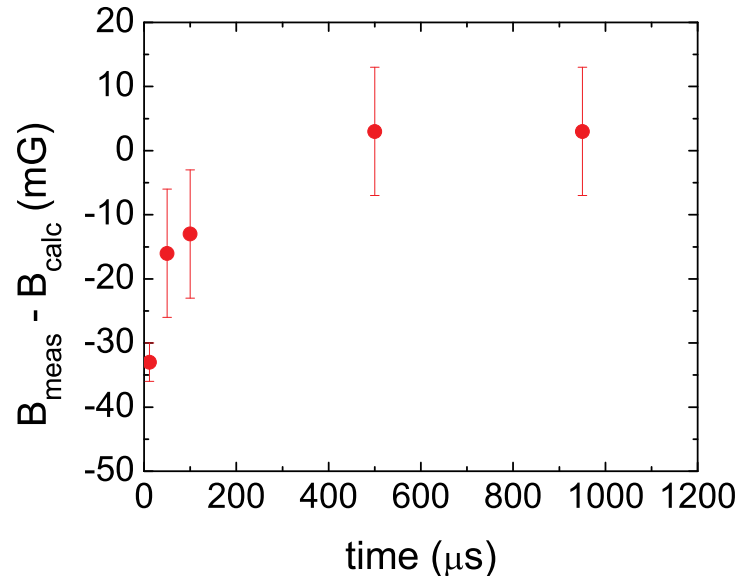


Figure 2.27: Measured magnetic-field deviation after a fast ramp. Plotted is the difference between the measured magnetic field and the total calculated field (red line in Fig. 2.26) after the 140 G/ms upward ramp.

sorption imaging can be found, for example, in Refs. [79] and [80]. In brief, a collimated beam of resonant laser light is directed toward the atom cloud, and its shadow is imaged onto a Roper Scientific back-illuminated CCD camera (MicroMax 1024B). The light integrates through one dimension of the cloud, rendering a two-dimensional image from which we can extract the atom number, temperature, and density.

For much of the experimental sequence, we are able to interrogate the atoms with low-field imaging. In this technique, all trapping fields are turned off, and the atoms are allowed to ballistically expand for 5 to 20 ms, depending on their number and temperature. A circularly polarized laser beam is directed toward the atoms along the axis of the vacuum system (in through the MOT cell, and out through the science cell—see Fig. 2.2). For imaging Rb, the light is tuned to the $f = 2 \rightarrow f' = 3$ atomic cycling transition, and for K, the light is tuned to the $f = 9/2 \rightarrow f' = 11/2$ transition. A small (3 G) magnetic field is directed along the axis of the probe beams to maintain quantization. By switching the direction of this field, we are able to image either the negative or the positive m_f atomic Zeeman states. Using the camera’s kinetics mode, we are able to take images of both the K cloud and the Rb cloud separated by only a few milliseconds, allowing us to probe both species in a single experimental run.

Many of our experiments involve manipulating the magnetic field in the vicinity of interspecies Fano-Feshbach resonances at fields above 500 G. An accurate measure of the number and temperature of the atoms and any molecules formed at the resonance requires the ability to image the clouds at these large magnetic fields. Due to the Zeeman effect, the K $|9/2, -9/2\rangle \rightarrow |11/2, -11/2\rangle$ cycling transition at these fields is shifted from the zero-field transition by more than 600 MHz, and the Rb $|2, 2\rangle \rightarrow |3, 3\rangle$ transition is shifted by more than 700 MHz. Figure 2.28 shows how the light for this high-field imaging is obtained from

the Rb and K lasers. At low fields, the atomic Zeeman states are nearly degenerate, and are not distinguished by the probe light. However, at these large fields, the transitions for imaging the two lowest-energy Zeeman states in K, $|9/2, -9/2\rangle$ and $|9/2, -7/2\rangle$ are separated by > 65 MHz, and the transitions for imaging the $|2, 2\rangle$ and $|2, 1\rangle$ states of Rb are separated by nearly 200 MHz. Thus, imaging at high fields enables spin-selective imaging of both species. For experiments with the Fano-Feshbach resonances, the Rb atoms are not in the $f = 2$ state, but in the $|1, 1\rangle$ state. To access the $f = 2 \rightarrow f' = 3$ cycling transition, we transfer the Rb atoms to the $|2, 2\rangle$ state via microwave adiabatic rapid passage. For this, we commissioned a coil from the JILA shop that is impedance-matched at 8.0 GHz [63]. The coil is also impedance-matched at 6.8 GHz, the frequency needed to prepare the Rb atoms in the $|1, 1\rangle$ state at low fields.

While we are able image to both species at high fields, our current imaging configuration is not optimal. As shown in Fig. 2.29, the probe beams are perpendicular to the large bias magnetic field. The beams, therefore, cannot be made to be σ^+ or σ^- polarized with respect to the field. The best option for this geometry is to linearly polarize the beams. This results in a factor of two decrease in the observed optical depth, i.e. a factor of two decrease in our signal. The optimal configuration would be a circularly polarized imaging beam along the magnetic field, resulting in an automatic factor of two increase in signal from the polarization and an additional increase in the optical depth due to integrating through the long direction of the atom cloud. Efforts are currently under way to install a second imaging axis along the magnetic field (dashed lines in Fig. 2.29).

2.8 Isolating the track controller that spews noise all over the lab

One problem that plagued our new and improved experimental setup from time to time was rf noise that was picked up by the IP trap. When measuring the

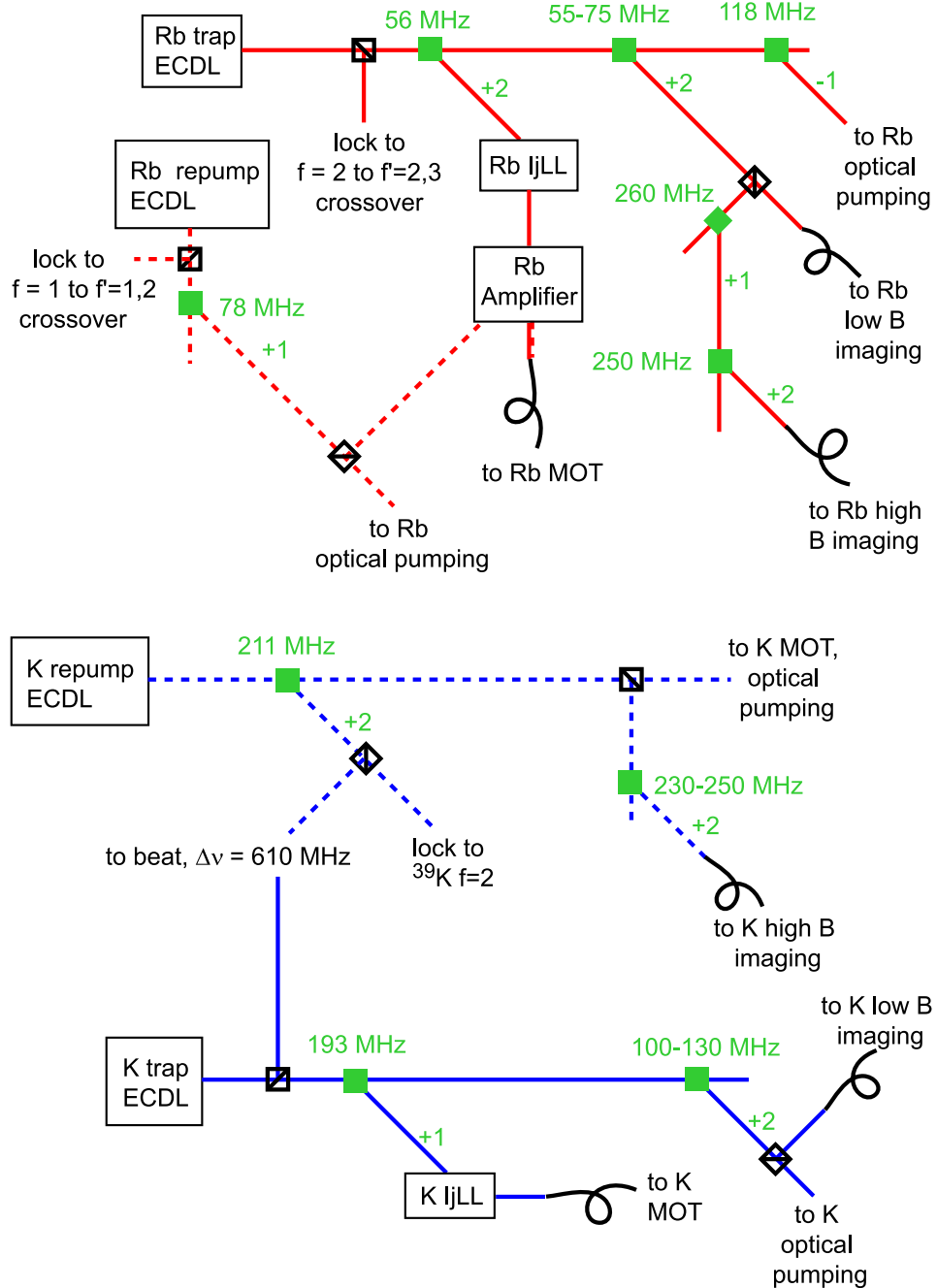


Figure 2.28: Laser frequencies for trapping, pumping, probing Rb and K. The K repump and Rb external cavity diode lasers (ECDLs) are each referenced to atomic transitions using saturated absorption spectroscopy [81], while the K trap ECDL is referenced to the K repump laser via an offset lock [75]. The green boxes are acousto-optic modulators (AOMs) with the numbers 1 and 2 representing a single- or double-passed AOM and the + and - indicating whether the light is shifted blue or red. The loops represent optical fibers.

pick-up with a spectrum analyzer, we observed noise peaks around 2 and 5 MHz. These frequencies are particularly detrimental to atoms in the magnetic trap as they are able to drive Zeeman transitions to untrapped states in low-energy atoms. For comparison, the trap bottom corresponds to 2.1 MHz for Rb and 0.9 MHz for K. The result of this rf noise was a severe reduction in the trap lifetime from 200 s to 40 s, rendering the magnetic-trap evaporation, which takes 60-70 s, hopelessly inefficient.

This rf noise would disappear occasionally, often coinciding with changes to the IP trap current servos or with changes to the IP trap circuit itself.³ Inevitably, though, the noise would rear its ugly head after a few hours, days, or weeks. Since we believed we were influencing the noise with changes to the IP trap circuitry, we thought the rf must have been originating in the power supply, the servos, or a ground loop in the system. After many months of this mysterious rf coming and going, we were able to determine the source: the Aerotech Soloist, the controller for the track for the quadrupole coils.

Shortly after the overhaul of the vacuum system, due to a malfunction in its communications with the experiment control computer, we replaced the BA Intel-lidrive that had previously controlled the track with Aerotech's latest controller, the Soloist. This new controller, while having the advantage of more user-friendly controls, has the disadvantage that it broadcasts harmonics of 80 kHz up to 25 MHz as shown in Fig. 2.30. The noise was transmitted via the various inputs and outputs of the Soloist to the control computer, the TTL controls for all the equipment in the lab, the power lines, and, of course, the IP trap. To isolate the controller, we built a mu-metal enclosure around the Soloist. However, the transmission lines to and from the Soloist also required isolation. We improved the shielding of the TTL inputs, and the coaxial cable that carries the trigger signal

³ Note that the data in the §2.4 were taken during one such "happy time".

for the cart has been moved from the cable tray above the optics table, where the noise is easily transmitted to nearby cables, to below the table, where no other cables pass. Additionally, we now use a fiber-optic USB cable to transmit signals to and from the control computer, and the AC power passes through a noise suppressor to prevent the Soloist from contaminating the AC for other equipment in the lab. These steps to isolate the track controller have eliminated the rf pick-up at the IP trap and the associated lifetime problems, allowing for the experiments discussed in the rest of this thesis.

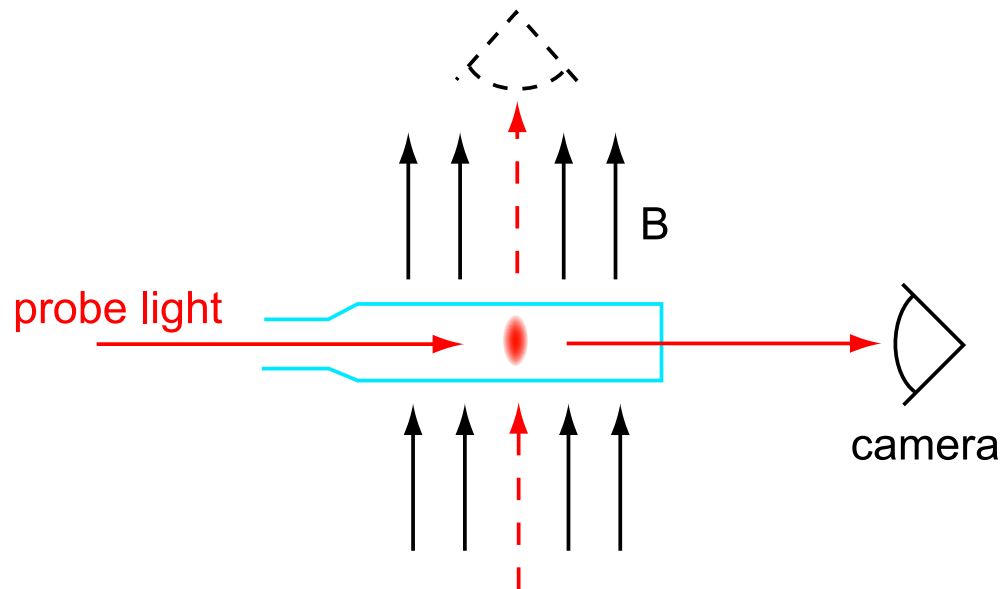


Figure 2.29: Schematic of the high-field imaging configuration (top view). Currently, atom clouds (red oval) are imaged with probe beams perpendicular to the magnetic field. The dashed lines represent a proposed new imaging axis along the magnetic field.

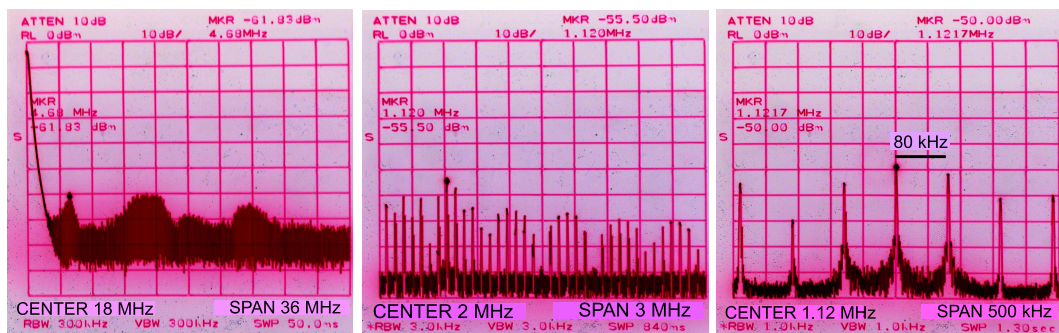


Figure 2.30: Noise broadcast by the Soloist cart controller. Shown are spectrum analyzer traces of rf picked up by a 1-in diameter coil placed in close proximity to the Soloist. Harmonics of 80 kHz are observed up to 25 MHz.

Chapter 3

Creating molecules with a Fano-Feshbach resonance

The critical tool that has enabled all of the experiments detailed in this thesis is the interspecies Fano-Feshbach resonance. Magnetic-field tunable Fano-Feshbach resonances provide the knob with which we can control the interactions between colliding atoms and allow us to coax unpaired atoms into forming molecules. I will begin this chapter with a brief introduction to Fano-Feshbach resonances and how they affect atomic scattering properties. I will then describe how we are able to exploit the resonances to create and probe KRb molecules.

3.1 Fano-Feshbach resonances

A full calculation of atom interactions at a Fano-Feshbach resonance requires detailed knowledge of interatomic potentials and the coupling between many atomic energy states [82, 83, 84, 85]. For example, a Fano-Feshbach resonance involving ^{40}K atoms in the $|9/2, -9/2\rangle$ state and ^{87}Rb atoms in the $|1, 1\rangle$ state can couple the atoms to eleven other pair states. However, the atomic interactions near resonance are typically dominated by the coupling between only two states and can be described by a two-level Hamiltonian [86, 87]. Here, I will use this simplified two-level picture to illustrate the features of Fano-Feshbach resonances.

The potential energy of two colliding S -state alkali-metal atoms can be

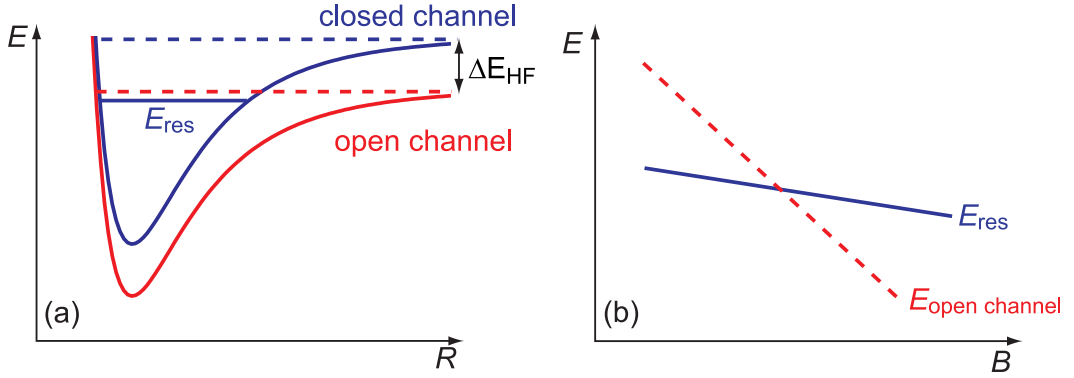


Figure 3.1: Schematic of a Fano-Feshbach resonance. (a) A Fano-Feshbach resonance results from coupling between the threshold of an open channel of the interatomic potential and a bound state in a closed channel. At zero magnetic field, the dissociation thresholds are split by the hyperfine energy ΔE_{HF} . (b) An external magnetic field causes the energy of each state to vary according to the Zeeman effect, which can lead to level crossings.

generically described by a potential that is repulsive at small internuclear distances, R , and has a van der Waals attraction that goes as $1/R^6$ at large R , as shown schematically in Fig. 3.1a. Hyperfine interactions cause the energy levels of the possible collision channels (labeled by the quantum numbers f and m_f of the pair) to split. An atom pair entering an elastic collision in a lower channel with kinetic energy less than the hyperfine splitting ΔE_{HF} cannot exit the collision in the upper channel due to energy conservation. Thus, a channel is said to be “closed” if the energy of the colliding atoms is less than that channel’s dissociation threshold and “open” otherwise. In ultracold atom gas experiments, collision energies are $\lesssim 1 \mu\text{K}$, while hyperfine energy splittings can be 10s to 100s of mK. Therefore, the different channels are well-resolved by the colliding atoms.

It is possible for a bound state in a closed channel to be nearly degenerate with the dissociation threshold of an open channel, as drawn in Fig. 3.1a. As illustrated in Fig. 3.1b, due to the Zeeman effect the energy difference between channels can be magnetic-field dependent. A Fano-Feshbach arises when

the dissociation threshold of an open channel, which is coupled to a closed channel, becomes nearly degenerate with a bound state in that closed channel. The interchannel coupling is provided by the Coulomb, or exchange, interaction, which couples together different hyperfine states at short internuclear distances [85, 88]. When two atoms collide, the strong electrostatic interactions can overcome the hyperfine interaction, allowing spin flips to occur. This interchannel coupling creates a “dressed” molecule state, which is a linear superposition of the open and closed channel states. The magnetic-field at which this dressed molecular state goes through threshold is known as the Fano-Feshbach resonance position B_0 and is in general shifted from the field at which the bare states cross [86].

As we know from the theory of low energy scattering (see for example, Ref. [89] and [90]), when a bound state is introduced into a scattering potential, the s -wave scattering length diverges. The scattering length near a Fano-Feshbach resonance is given by [88, 91]

$$a(B) = a_{\text{bg}} \left(1 - \frac{\Delta}{B - B_0} \right), \quad (3.1)$$

where a_{bg} is the background scattering length for atoms in the open channel, and the magnetic-field width of the resonance Δ is defined as the difference between B_0 and the field at which $a = 0$. Figure 3.2 shows the magnetic-field dependence of the calculated interspecies scattering length for the Fano-Feshbach resonance used in the majority of the experiments in this thesis.

3.2 Locating the resonances with atom loss

It has been shown both theoretically [93, 94, 95, 96, 97] and experimentally [91, 98, 99, 100, 101] that the increased scattering lengths for elastic collisions at Fano-Feshbach resonances are accompanied by increased inelastic collision rates. The predominant inelastic collisions in ultracold atom gas experiments are spin

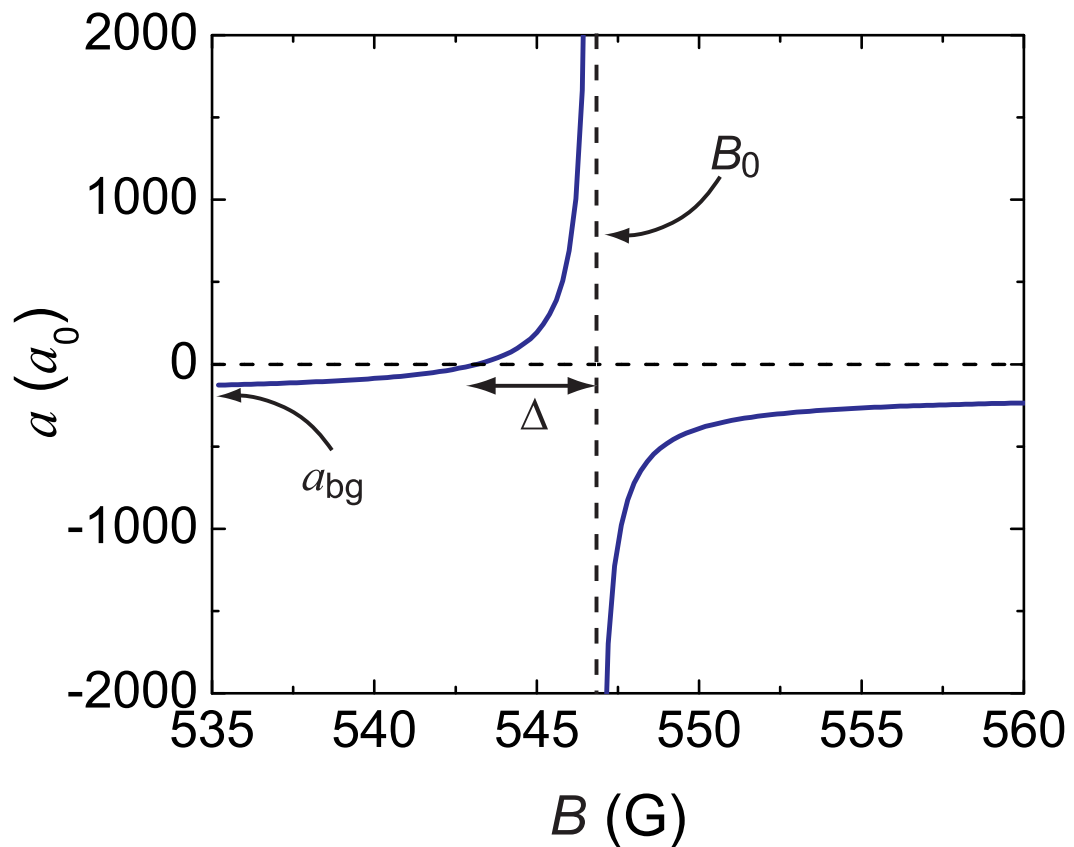


Figure 3.2: Magnetic-field dependence of the scattering length at a Fano-Feshbach resonance. The interspecies scattering length is calculated for the Fano-Feshbach resonance between ^{40}K atoms in the $|9/2, -9/2\rangle$ state and ^{87}Rb atoms in the $|1, 1\rangle$ state at $B_0 = 546.76$ G [11, 92, 19, 64, 37]. The calculation uses $\Delta = -3.6$ G [64] and $a_{bg} = -185 a_0$ [92], where a_0 is the Bohr radius.

relaxation, in which one or both atoms “spin flip” into a lower energy state, and three-body recombination, in which three atoms collide, allowing two to form a molecule with the third carrying away the binding energy. Both of these mechanisms can result in heating and loss of atoms from the trap. Thus, one signature of a Fano-Feshbach resonance is magnetic-field dependent atom loss. We originally identified four Fano-Feshbach resonances between ^{40}K atoms in the $|9/2, -9/2\rangle$ state and ^{87}Rb atoms in the $|1, 1\rangle$ state by measuring the number of atoms in the trap after a long (1 s) hold at a variable magnetic field [11]. These initial experiments were performed with a relatively high temperature ($14 \mu\text{K}$) and a number ratio of $N_{\text{Rb}}/N_{\text{K}} = 10$.

Upon achieving the improved conditions discussed in §2.4, we set about remeasuring the positions of the Fano-Feshbach resonances by observing losses. We prepared the mixture in an optical trap with radial and axial frequencies of 340 and 4.4 Hz for Rb and 495 and 6.3 Hz for K. The number of atoms in each species varied from day to day from $4 - 7 \times 10^4$ K atoms and $6 - 9 \times 10^4$ Rb atoms at a temperature of 320 nK, corresponding to $0.8 - 0.9 T_F$ and $2.0 - 2.3 T_C$. Here, T_F is the Fermi temperature for the K gas, and T_C is the critical temperature for Bose-Einstein condensation for Rb. Figure 3.3 shows the locations of three Fano-Feshbach resonances between ^{40}K and ^{87}Rb in their lowest energy states. For each resonance, the number of atoms remaining in each species after a variable hold time at B_{hold} was measured. The hold time was chosen such that for all values of B_{hold} no more than 80% of the initial number in each species was lost from the trap. Additionally, it was confirmed for each resonance that loss was observed in both species and that no losses were observed if only one species was present. In Figs. 3.3b and c, the atom loss feature at the Fano-Feshbach resonance appears asymmetric. We attribute this asymmetry to losses incurred when the magnetic field is ramped across the resonances. A schematic of the time-dependent magnetic

field is shown in Fig. 3.3a.

Figures 3.3d and 3.3e show number loss and corresponding heating at the Fano-Feshbach resonance at 515 G. Both show a double-peaked structure, indicating that this resonance is a *p*-wave resonance [102].¹ The existence of a *p*-wave resonance in this mixture had been predicted in Ref. [102], but which of the four originally observed Fano-Feshbach resonances was the *p*-wave resonance became the subject of some confusion. Due to the high temperature of the initial observations [11], the doublet structure could not be resolved. Our calculations suggested that the 495 G resonance was a *p*-wave resonance [11], while a subsequent calculation from the LENS group constrained by the observation of many additional resonances in several spin states ascribed *p*-wave character to the 515 G resonance [92]. This later identification was confirmed by S. Ospelkaus *et al.*, with the observation of the doublet structure of the 515 G resonance through a measurement similar to that shown in Fig. 3.3d, but in finer detail [19].

3.3 KRb Feshbach molecules

If experiments can be performed on timescales short compared with those for the atom losses and heating at a Fano-Feshbach resonance, the divergence of the *s*-wave scattering length (Fig. 3.2) and the introduction of a bound state (Fig. 3.1) can be exploited. Some of the initial experimental work with Fano-Feshbach resonances employed magnetic-field control of atomic interactions to improve evaporation efficiency in ^{85}Rb [99] and ^{133}Cs [103] and to control the size of and induce collapse in a BEC [104, 16]. In recent years, however, much experimental work has been directed toward the production of large samples of ultracold molecules via magnetic-field sweeps across Fano-Feshbach resonances

¹ For the data in Fig. 3.3, we were limited to steps of 40 mG by the resolution of the DAC that controlled the magnetic field. This limitation was later eliminated by the introduction of the ‘Fast B’ circuit discussed in §2.6.

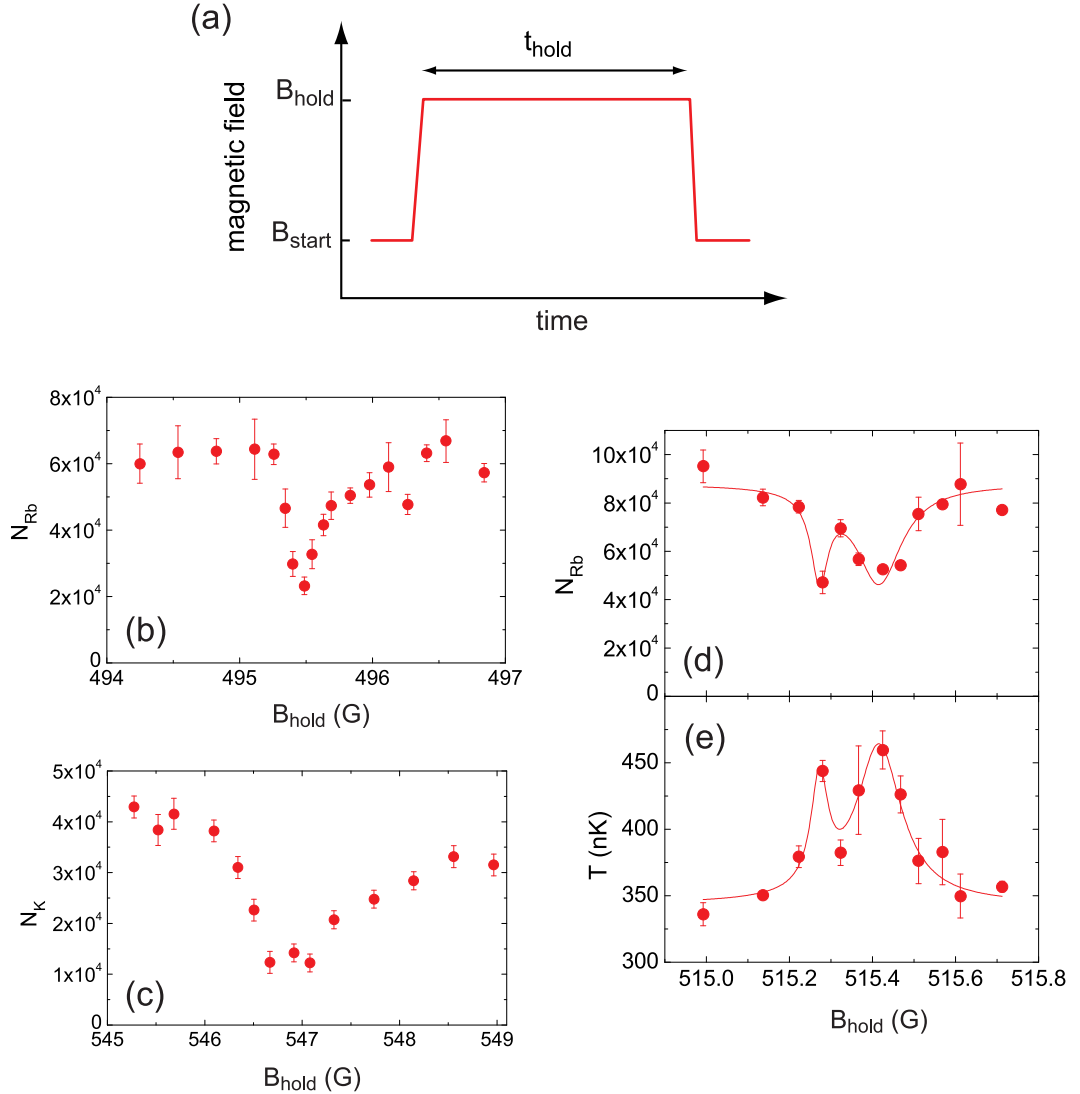


Figure 3.3: Magnetic-field dependent atom loss at Fano-Feshbach resonances between ^{40}K atoms in the $|9/2, -9/2\rangle$ state and ^{87}Rb atoms in the $|1, 1\rangle$ state. The resonances are approached from below as shown in (a). For each resonance, B_{start} is at least 5 G below the peak of the loss. Plotted in (b)-(d) is the measured atom number in one species after a variable hold time at a magnetic field B_{hold} in the vicinity of three Fano-Feshbach resonances between ^{40}K and ^{87}Rb atoms in their lowest energy states. The hold times are 100 ms in (b), 40 ms in (c), and 400 ms in (d). Shown in (e) is the increase in temperature associated with the atom loss at resonance. The lines are guides to the eye. In all the plots, the error bars represent the statistical error of repeated data points.

[105, 8]. This “magneto-association” technique has been shown to convert as much as 90% of a sample of ultracold atoms into highly vibrationally excited Feshbach molecules [61].

3.3.1 Magnetic-field sweeps

Since Fano-Feshbach resonances arise from the coupling of an atom pair state to a bound state, it is possible to associate free atoms into molecules with time-dependent magnetic fields. A variety of methods have been used to create Feshbach molecules. These include applying rapid magnetic-field pulses [44] and oscillating magnetic fields [62] near a resonance. The simplest technique for associating atoms into Feshbach molecules is to sweep the magnetic field through the resonance [105]. As shown schematically in Fig. 3.4, atoms initially prepared on the high-field side of the resonance can be converted to molecules by sweeping the magnetic field downward in time. Molecules can be created if the ramp speed is slow compared to the two-body physics of the Fano-Feshbach resonance. If the ramp is too fast, however, the atoms will remain in the atom pair state after the ramp. It is this method of using adiabatic magnetic-field sweeps that we employed to begin creating KRb Feshbach molecules.

There are several Fano-Feshbach resonances between K $|9/2, -9/2\rangle$ atoms and Rb $|1, 1\rangle$ atoms (see Fig. 3.3, Ref. [92]). We choose to create KRb molecules using the resonance near 547 G because it is the widest accessible resonance between these two states. To make molecules, we prepare a mixture of 8×10^4 Rb atoms and 2.5×10^5 K atoms in an optical trap with radial trapping frequencies of 560 Hz for Rb and 730 Hz for K and axial frequencies of 7.2 Hz for Rb and 10.4 Hz for K. The temperature of the mixture is 300 nK, which corresponds to $1.2 T_C$ and $0.3 T_F$. For the 547 G resonance, the molecule state exists only on the low-field side of the resonance. A magnetic-field sweep to create molecules must,

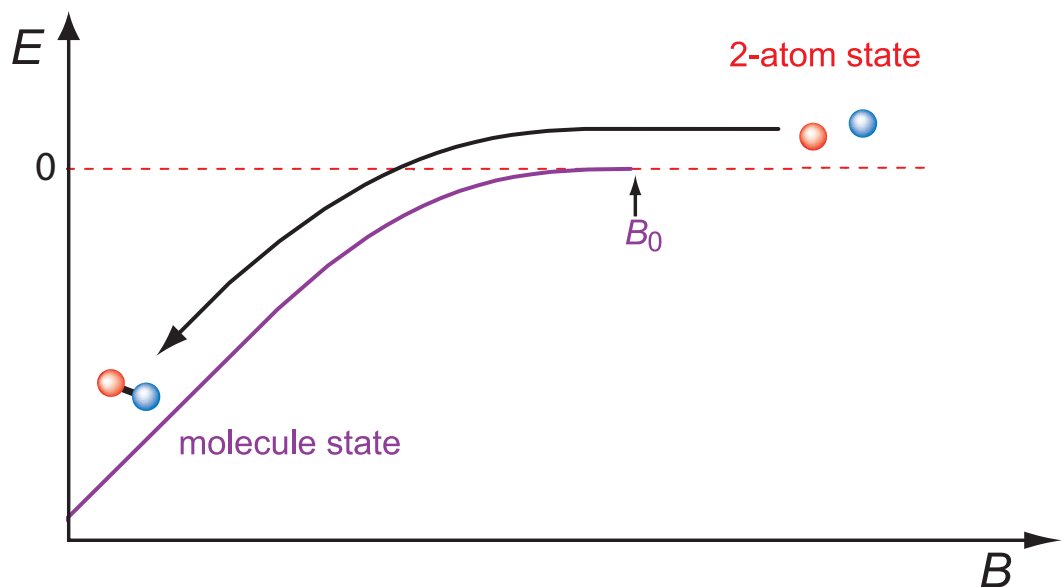


Figure 3.4: Molecule association with magnetic-field sweeps. At the Fano-Feshbach resonance, the energy of the 2-atom state and the molecule state are degenerate. By preparing the atoms on the high-field side of the resonance, then sweeping the field downward through resonance, atoms can be converted into Feshbach molecules.

therefore, begin above the resonance. We prepare the atoms on the high-field side of the resonance by first slowly increasing the magnetic field to 542.1 G during the optical trap evaporation, then rapidly sweeping the magnetic field up through the resonance to 549.9 G at a speed of 140 G/ms. To create molecules, we then sweep the magnetic field down through the resonance to 543.6 G as shown in Fig. 3.5a. To see the effect of the magnetic-field sweep, we measure the number of remaining Rb atoms using resonant absorption imaging. The gas is released from the trap and imaged after 2 ms of expansion. The Rb probe light is not sensitive to the molecules. Therefore, molecule creation results in a perceived loss of atoms. The measured number of Rb atoms remaining after the sweep through resonance is shown as a function of the ramp speed in Fig. 3.5b. For these data, the $1/e$ ramp speed for molecule creation is $\dot{B}_{1/e} = (26 \pm 7)$ G/ms.

The observed atom loss from magnetic-field sweeps through resonance is consistent with molecule creation, but as we have seen in Fig. 3.3, Fano-Feshbach resonances can also cause real atom losses. To verify that we are adiabatically creating molecules, we can check that the apparent atom loss is reversible. We sweep the magnetic field through resonance at a speed of 3.3 G/ms, then reverse the sequence as shown in Fig. 3.5b. The sweep back up through resonance dissociates the molecules, causing them to “reappear” as unbound atoms that we are then able to image. Figure 3.5d compares the measured number of Rb atoms after such a double-sweep experiment with the number left after a single sweep. The number of atoms remaining after two sweeps is larger than after only one sweep, indicating that some of the atoms were not lost but transferred to the molecule state after the first sweep. The number of molecules recovered by the upward sweep equals the difference between the two curves in Fig. 3.5d. For the shortest hold time, we recover 3×10^4 molecules. By varying the time between the two sweeps, we can measure the lifetime of the molecules. At the hold field

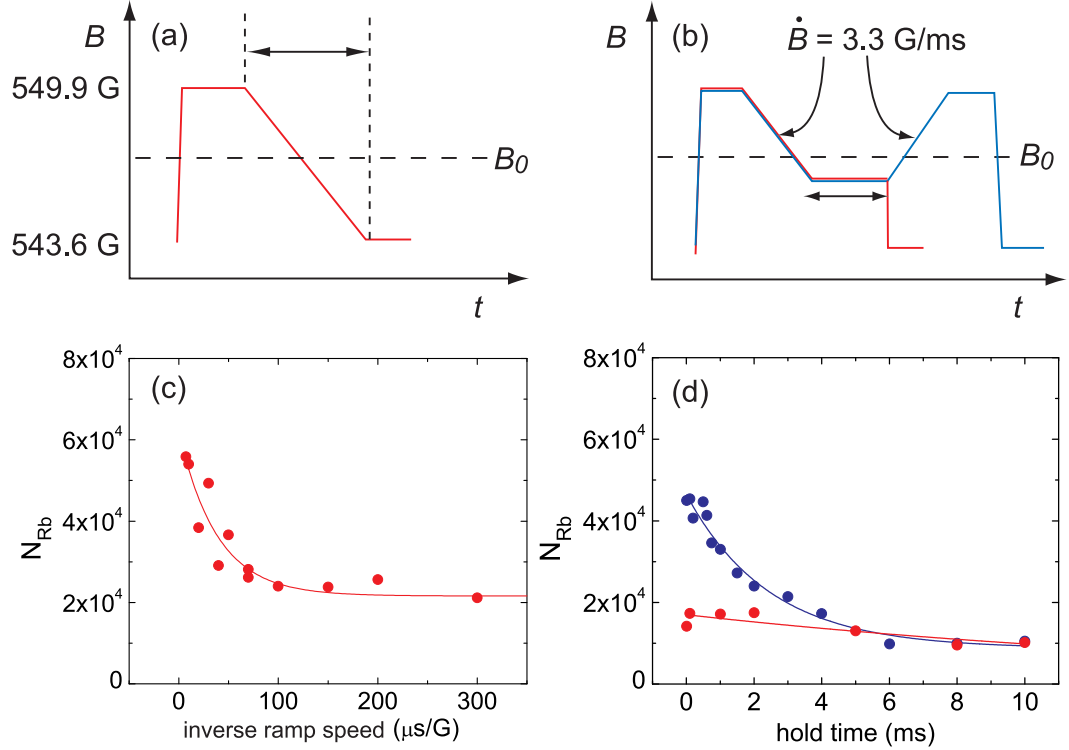


Figure 3.5: Molecule creation via magnetic-field sweeps through a Fano-Feshbach resonance. A schematic of the time dependent magnetic field for creating molecules is shown in (a). The measured number of Rb atoms N_{Rb} remaining after the molecule creation ramp as a function of the inverse ramp speed ($1/\dot{B}$) is shown in (c). Before the resonance is crossed, the measured number of Rb atoms is $N_{\text{Rb}} = 8 \times 10^4$. The line is a fit to $N_{\text{Rb}} = A e^{-\beta/\dot{B}} + y_0$, yielding $A = (4.0 \pm 0.6) \times 10^4$ and $\beta = (26 \pm 7)$ G/ms. Note that the number of Rb atoms remaining after the fastest sweeps indicates an initial loss of 2×10^4 Rb atoms, which may be due to the first resonance crossing. (b) shows a schematic of the magnetic-field sweeps used to measure the molecule lifetime in (d). (d) The blue points show the measured number of Rb atoms after a slow sweep back up through resonance as a function of the hold time at $B = 546.27$ G. To account for any atom loss at the hold field, this number is compared with the number of atoms remaining after the molecule creation sweep and hold (red points). Subtracting the two curves, which are exponential fits to the data, yields the number of molecules recovered by the second sweep $N_{\text{mol}} = (3.1 \pm 0.2) \times 10^4$ and the $1/e$ lifetime $\tau = (2.0 \pm 0.4)$ ms.

of $B = 546.27$ G, we observe a decay in the number of atoms (red points in Fig. 3.5d), and to accurately measure the molecule lifetime, we must subtract this atom loss. For the molecules in Fig. 3.5d, the $1/e$ lifetime is (2.0 ± 0.4) ms.

Comparing the initial number of Rb atoms, 8×10^4 , with the number measured after one and two sweeps, we observe losses that are not recovered by the second sweep. We believe this is due to the enhanced 3-body and atom-molecule collision rates associated with the resonance [106, 107].

3.3.2 Density dependence of molecule creation sweep rates

Theoretical calculations for the adiabatic association of molecules with magnetic-field sweeps in single-species experiments have shown that the $1/e$ ramp speed depends linearly on the atom gas density [86, 108]. Measurements of the adiabatic ramp speed for varying densities in ^{85}Rb experiments are consistent with a linear dependence [61]. We have measured the $1/e$ ramp speeds for a variety of Rb and K densities as shown in Fig. 3.6. We vary the density by changing both the relative number in the two species and the strength of the optical trap. We define the two-species density as $2\sqrt{\langle n_{\text{K}} \rangle \langle n_{\text{Rb}} \rangle}$, where $\langle n_i \rangle = \frac{1}{N_i} \int n_i^2(r) d^3r$ is the average number density of species i . This generalization from the single-species case arises from the fact that the number of possible pairs in a single species is $N(N - 1)/2 \approx N^2/2$, while the number of possible pairs in the mixture is $N_{\text{K}}N_{\text{Rb}}$ [109]. The measured $1/e$ ramp speeds are inconsistent with the expected linear dependence on the two-species density, but instead show a quadratic dependence on the density. This suggests that our generalization to two species is incorrect. However, these measurements were performed observing only atom loss (not directly imaging molecules—see §3.4 below). Our measurements of molecule number are always smaller than the observed atom loss, indicating atom and/or molecule loss during the sweep. Therefore, the measured sweep speeds may be

a convolution of molecule creation and loss rates. Future efforts will be focused on understanding (and minimizing) loss mechanisms, and studying the density dependence of molecule creation rates.

3.3.3 Why we no longer use a 1075 nm broadband laser

Prior to the results shown in Fig. 3.5, our initial experiments creating molecules were performed in an optical trap formed from a multi-longitudinal mode 1075 nm fiber laser. We were able to observe loss with a single downward sweep through the Feshbach resonance, while no loss was observed with a single upward sweep. This was suggestive of molecule formation, but double sweep experiments similar to that shown in Figs. 3.5c and d yielded small numbers of atoms returning with lifetimes much shorter than 1 ms. Zirbel and coworkers demonstrated that the short molecule lifetime was due to the optical trap light [70]. We believe the trap light excites the Feshbach molecules to the lowest vibrational states of the 3(1) excited state potential, as shown in Fig. 3.7. We now use a multi-longitudinal mode fiber laser at a wavelength of 1090 nm for the optical trap. The energy of a photon from this laser is too small to excite bound-bound transitions to the 3(1) state. While the 2(1) states are accessible, these are not expected to be strong transitions [110]. With this laser forming the optical trap, we have observed molecule lifetimes as long as 10 ms, which are likely limited by collisions with unbound atoms [106].

3.4 Molecule imaging

The fact that we are able to recover missing atoms with additional magnetic-field sweeps indicates that we are, in fact, creating molecules with the initial downward sweep through the resonance. This method of comparing the number of missing atoms after a molecule association sweep with the number recovered

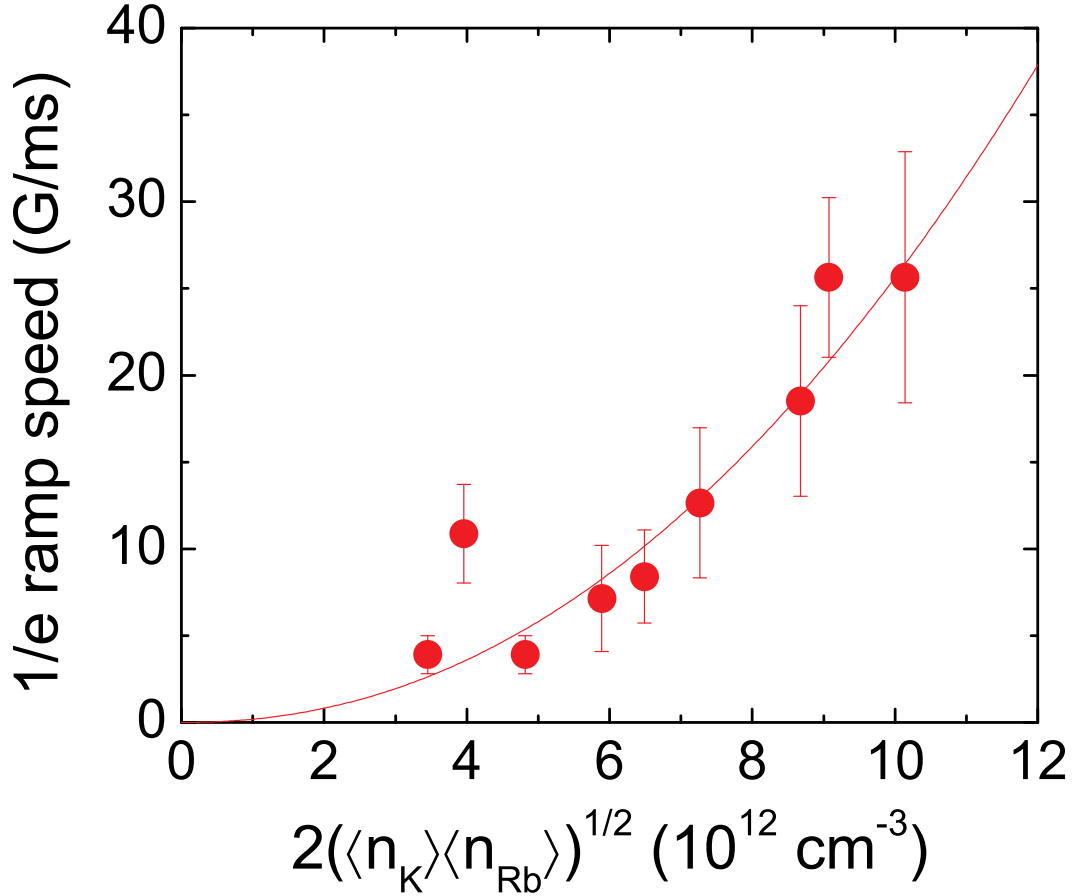


Figure 3.6: Measured density dependence of adiabatic magnetic-field sweep speeds. The number of atoms remaining after magnetic-field sweeps through the Fano-Feshbach resonance were measured as a function of the sweep speed as in Fig. 3.5c, for mixtures with varying densities. The $1/e$ sweep speed $\dot{B}_{1/e}$ is plotted as a function of the two-species density $n_{KRb} = 2\sqrt{\langle n_K \rangle \langle n_{Rb} \rangle}$. The line is a fit of the data to $\dot{B}_{1/e} = A \cdot n_{KRb}^b$, yielding $A = (3.7 \pm 0.3) \times 10^{-27} \text{ cm}^6$ and $b = 2.1 \pm 0.2$.

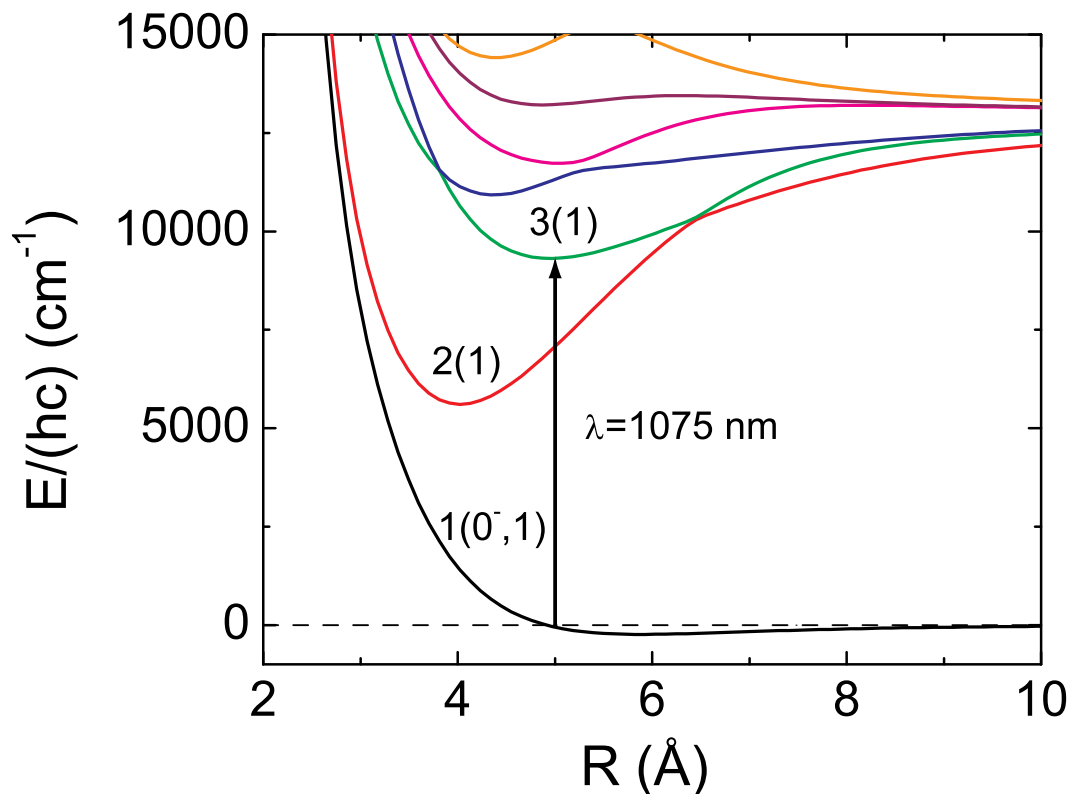


Figure 3.7: KRb molecular potentials. Laser light with a wavelength of 1075 nm can excite transitions from the Feshbach molecule state to vibrational states in the 3(1) or 2(1) excited molecular potentials. (This figure was produced using the potential energies of the KRb molecule from Ref. [111].)

with a dissociation sweep will underestimate the molecule number if there are any additional atom or molecule losses as the Fano-Feshbach resonance is traversed again. Additionally, if the fraction of atoms converted to molecules is small, an accurate measurement of the molecule number is difficult due to typical shot-to-shot atom number variations of 7%. To avoid these limitations, we image the molecules directly.

We detect the molecules with spin-selective absorption imaging using light tuned to the K $|9/2, -9/2\rangle \rightarrow |11/2, -11/2\rangle$ cycling transition [112, 64]. This light is sensitive to molecules and unbound K atoms. To avoid imaging the unbound atoms, we use a 30- μ s pulse of rf tuned to the K atomic Zeeman transition to transfer the atoms to the previously unoccupied $|9/2, -7/2\rangle$ Zeeman state with 99% efficiency. We typically image the molecules at $B = 546.04$ G. Because their binding energy of $h \times 140$ kHz is large compared to the spectral width of the rf pulse, the molecules are unaffected by the pulse. A 50- μ s pulse of probe light is then applied after 0 to 5 ms of expansion from the trap. Presumably, the first photon incident upon a molecule causes it to dissociate, while subsequent photons scatter off the newly unbound K atom.

We are able to image the molecules at magnetic fields within 1 G of the Fano-Feshbach resonance. This range is large compared to that expected for the case of homonuclear molecules at a similar resonance. This is because the energy difference between the molecular ground and excited electronic potentials varies more slowly with internuclear separation R for the case of heteronuclear molecules than for the homonuclear case. For homonuclear molecules, the excited electronic potential varies as $1/R^3$, while the ground potential varies as $1/R^6$. For heteronuclear molecules, both potentials vary as $1/R^6$, allowing for a wider range of binding energies over which the molecules can absorb imaging light tuned to the atomic resonance.

3.5 Locating the resonance with molecule sweeps

As we have seen in §3.2, we can locate a Fano-Feshbach resonance by observing atom losses, but a more precise determination of its position can be obtained by observing the Feshbach molecules. To measure the position of the resonance, we observe the dissociation of molecules in a low density mixture [6] with the magnetic-field sequence shown in Fig. 3.8a. Molecules are created with a slow magnetic-field sweep through the resonance. The optical trap is then abruptly turned off to allow the atom/molecule mixture to ballistically expand and the density to drop. The magnetic field is then increased to a value B_{hold} near the Fano-Feshbach resonance, then decreased to $B = 546.04$ G to image any remaining molecules. If B_{hold} is above the resonance, the molecules dissociate. Performing this measurement on the expanded gas ensures that the atom density is sufficiently low that no molecules are formed with the final ramp through resonance and that many-body interactions are negligible. The observed number of molecules decreases sharply at $B_0 = (546.66 \pm 0.06)$ G as shown in Fig. 3.8b, and in good agreement with Refs. [64] and [37]. This method offers a much more precise measurement of the Fano-Feshbach resonance than the 3 G wide loss feature observed in Fig. 3.3.

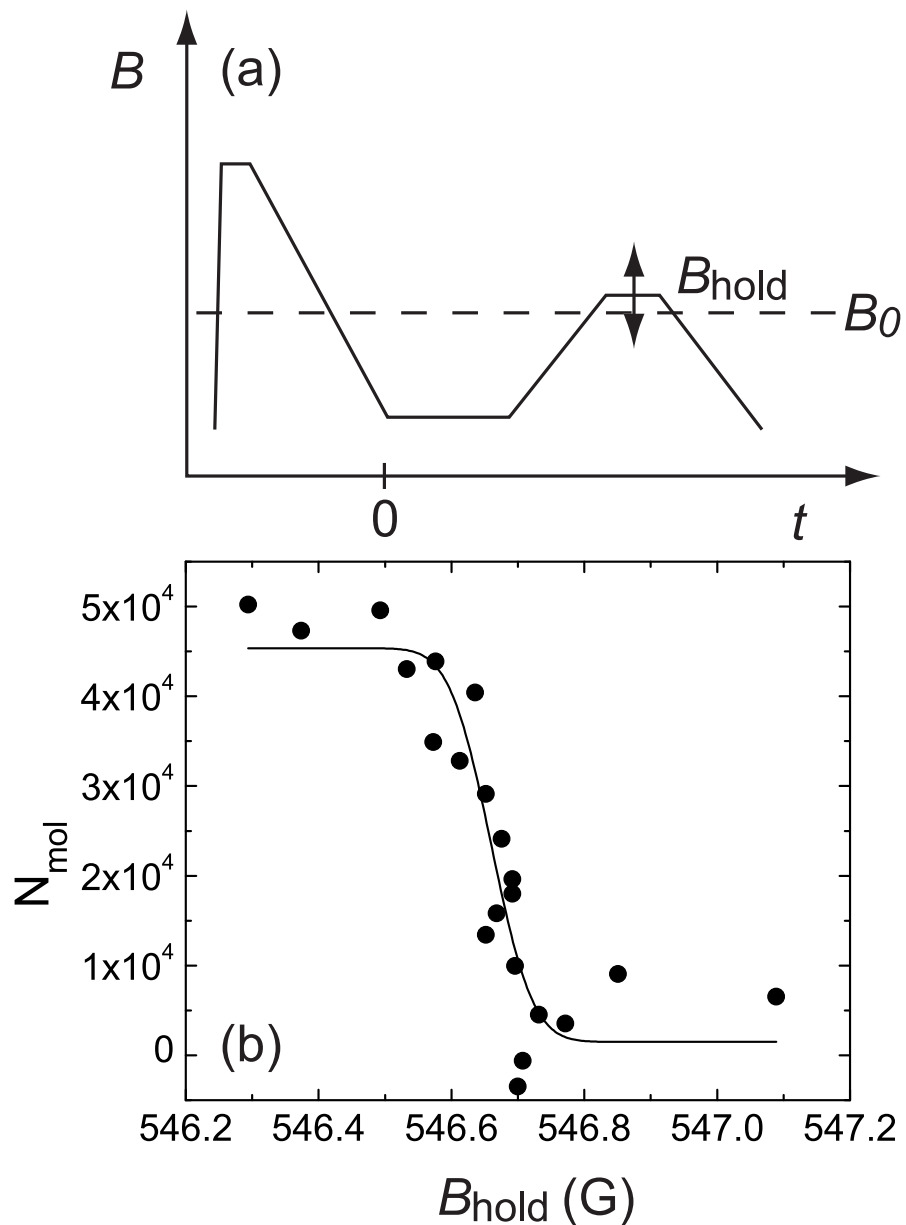


Figure 3.8: Determination of the Fano-Feshbach resonance position via molecule dissociation. A schematic of the magnetic-field sequence for creation and dissociation of molecules is shown in (a). The measured number of molecules N_{mol} as a function of B_{hold} is shown in (b). A fit of the data to an error function yields the Fano-Feshbach resonance position $B_0 = (546.66 \pm 0.06)$ G, where the uncertainty is given by the 10%-90% width.

Chapter 4

Semiclassical Monte Carlo simulations of molecule conversion

In the previous chapter, I showed that we can associate ultracold atoms into molecules with adiabatic magnetic-field sweeps through a Fano-Feshbach resonance. This technique had become widely used in single-species experiments by 2003, but how the final molecule fraction depends on experimental conditions was not studied in detail experimentally until 2005. Hodby *et al.* proposed that molecule conversion via an adiabatic sweep should depend on the phase space density of the atomic gas [61]. An adiabatic sweep smoothly alters the atom pairs' wavefunctions, but does not change the number of radial nodes in the two-atom wavefunction. Thus, Hodby *et al.* argued, for a pair of atoms to be converted into a molecule, they must have originally been sufficiently close in phase space for the pair wavefunction to be converted into that of a bound molecule. They developed a semiclassical Monte Carlo simulation to test this hypothesis and found that the experimentally measured molecule conversion efficiency in the cases of identical bosons and a two-component Fermi gas are described equally well by this model. The simulation was later extended and shown to successfully predict molecule conversion in a two-species Bose gas [63]. In this chapter, I will discuss the extension of the simulation to include Bose-Fermi mixtures for the purpose of designing experiments that maximize the fraction of molecules created.

4.1 Monte Carlo simulation

The Monte Carlo simulation was developed to describe the fraction of atoms converted to molecules in the limit of slow magnetic-field sweeps. It does not address the dynamics of molecule formation, nor does it describe the timescales of the adiabatic sweeps. The simulation operates on three simple assumptions: (1) Any atom can form a molecule with any other atom in the single-species case, or any non-identical atom in the case of two-component samples, if the two are sufficiently close in phase space, (2) Once a molecule is formed, the two atoms remain paired, and (3) The system is static—there are no losses, no collisions, and no motion over the timescale of the conversion. This implies that three-body recombination is so slow that it can be ignored, and the only mechanism for molecule formation is magnetoassociation. The simulation first generates an ensemble of particles whose randomly assigned positions and momenta follow the correct distributions for trapped bosons and/or fermions. The simulation program searches for a partner for each atom in turn, forming a molecule if the pair of atoms satisfies the phase space criterion

$$|\Delta r_{\text{rel}} \Delta v_{\text{rel}} \mu| < \frac{\gamma}{2} h, \quad (4.1)$$

where Δr_{rel} is the spatial separation of the two atoms, Δv_{rel} is their relative velocity, μ is reduced mass, h is Planck's constant, and γ is an experimentally determined constant.¹

The conversion fraction predicted by the simulation was compared to experiments with an uncondensed Bose gas of ^{85}Rb atoms and a two-component Fermi gas of ^{40}K atoms taken over a wide range of phase space densities of the gas [61]. Figure 4.1, reproduced from Ref. [61], shows the measured molecule fraction and

¹ Equation 4.1 differs from Eq. 3 in Ref. [61] by a factor of 2 because I have made the substitution $m \rightarrow 2\mu$.

prediction from the Monte Carlo simulation. The molecule conversion efficiency increases with increasing phase space density (decreasing T/T_F in Fig. 4.1 b) as expected, and the experimental data agree very well with the simulations. The results are best fit values of $\gamma = 0.44 \pm 0.03$ for the boson data and $\gamma = 0.38 \pm 0.04$ for the fermion data, indicating that molecule association is governed by the same physics in both cases.

4.2 Two-component systems

The ^{85}Rb and ^{40}K experiments showed that molecule formation via adiabatic sweeps depends on the phase space density of the atom gas, and in both cases, the conversion fraction approaches 100% as the quantum degeneracy of the atom gas increases. There are, however, factors in addition to the phase space density that can affect the conversion efficiency in two-component systems. The ^{40}K experiments were performed with a nearly 50/50 mixture of two spin states that experienced the same trapping potential, leading to identical spatial and momentum distributions for the two spin components. If the two components have different spatial profiles, quantum degeneracies, or numbers of particles, the overall efficiency of molecule conversion will change. In the ^{40}K experiment, it was observed that by changing the ratio of the two spin states, the fractional conversion of the spin state having fewer atoms could be increased [113].

The Monte Carlo simulation has been extended to include heteronuclear mixtures of bosons and compared to experiments in which Feshbach molecules were associated from an ultracold mixture of ^{85}Rb and ^{87}Rb [63]. Using the value of γ determined from the single-species boson experiment [61], the simulation correctly predicted the molecule conversion efficiency. While previous experiments had shown monotonic increases in molecule conversion with phase space density (see Fig. 4.1), in this experiment, the measured molecule fraction follows a peaked

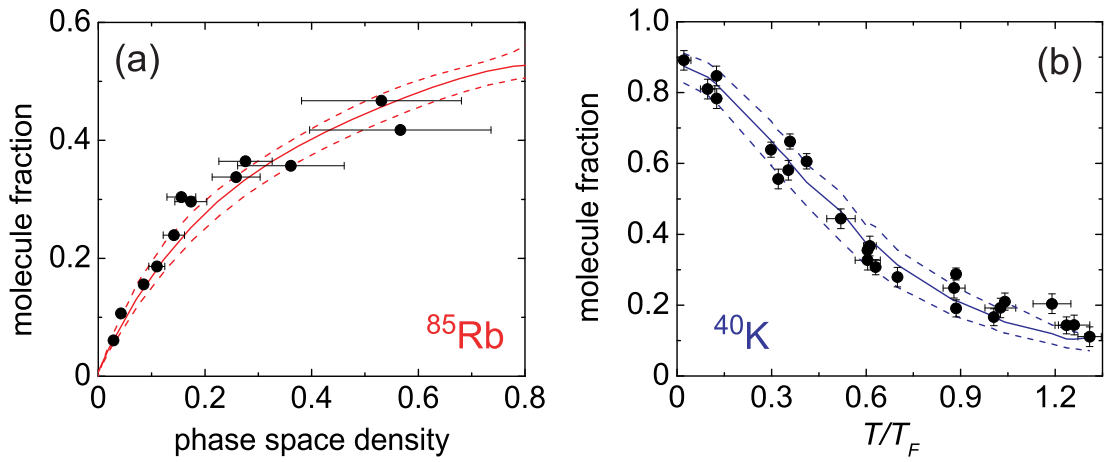


Figure 4.1: Temperature dependence of the molecule conversion in single-species experiments. The measured fraction of ^{85}Rb atoms converted into molecules as a function of phase space density for an uncondensed sample is shown in (a), and the fraction of ^{40}K atoms converted into molecules as a function of the degeneracy of the two-component Fermi gas is shown in (b). The solid circles (\bullet) are experimental data, while the lines are the best fits to Eq. 4.1 for the Monte Carlo simulation. (Figure reproduced from Ref. [61].)

curve as function of quantum degeneracy as shown in Fig. 4.2. The temperature of ^{87}Rb is varied across the BEC transition, but the ^{85}Rb gas remains uncondensed due to a smaller number of atoms. The fraction of ^{85}Rb atoms converted into molecules increases as the ^{87}Rb gas cools, approaching T_C , the critical temperature for Bose-Einstein condensation, but then decreases as the ^{87}Rb condensate fraction increases. Above T_C , the spatial profiles and momentum distributions of the two clouds are similar, and as in the single-species case, higher phase space density results in a larger conversion fraction. Below T_C , a significant fraction of the ^{87}Rb atoms are in the condensate. The uncondensed ^{85}Rb cloud has a spatial extent and momentum distribution that are much larger than the BEC's. This reduced overlap causes reduced molecule conversion despite the increased quantum degeneracy.

4.3 ^{40}K - ^{87}Rb Bose-Fermi mixture in particular

In a Bose-Fermi mixture, we expect the molecule conversion to behave similarly to the ^{85}Rb - ^{87}Rb mixture experiment discussed above. If the temperature of the mixture is brought below T_C for the bosons, there will be a reduction in the spatial overlap of the boson and fermion clouds, causing a reduction in the molecule conversion efficiency. We have adapted the Monte Carlo simulation to accommodate a mixture of bosons and fermions and have compared the predicted molecule fraction to data from another ^{40}K - ^{87}Rb experiment at JILA [64].

In this experiment, the molecules are not created by magnetic-field sweeps, but by rf association [112]. For this process, the atoms do not begin in the Fano-Feshbach resonant state. ^{87}Rb atoms in the $|1, 1\rangle$ state and ^{40}K atoms in the $|9/2, -7/2\rangle$ states are prepared on the low-field side (molecule side) of the Fano-Feshbach resonance at $B_0 = 546.76$ G; this resonance affects collisions between Rb $|1, 1\rangle$ atoms and K $|9/2, -9/2\rangle$ atoms Rf photons tuned to the K

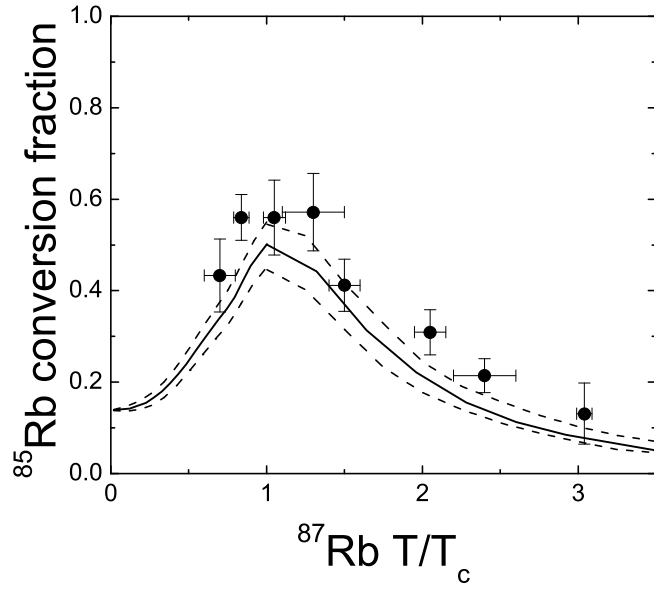


Figure 4.2: Temperature dependence of the molecule conversion in a bosonic mixture of ^{85}Rb and ^{87}Rb . The measured fraction of ^{85}Rb atoms converted to molecules as a function of the ^{87}Rb degeneracy is shown. Throughout the experiment, the ^{85}Rb gas remains uncondensed. The solid circles (\bullet) are experimental data, and the lines represent the molecule fraction predicted by the Monte Carlo simulation using $\gamma = 0.44 \pm 0.03$. (Figure reproduced from Ref. [63].)

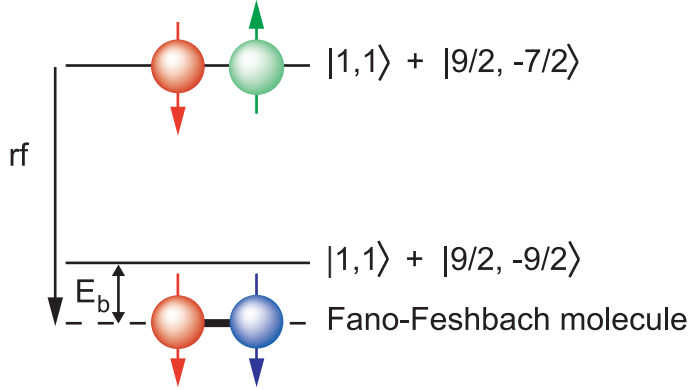


Figure 4.3: A simplified energy level diagram for rf association. Atoms start in the $|1,1\rangle + |9/2, -7/2\rangle$ state and are transferred into the molecular state via an rf photon detuned from the $K |9/2, -7/2\rangle \rightarrow |9/2, -9/2\rangle$ Zeeman transition by an amount equal to the molecule binding energy E_b .

$|9/2, -7/2\rangle \rightarrow |9/2, -9/2\rangle$ atomic Zeeman transition can create atom pairs whose interactions are controlled by the nearby resonance. An rf photon blue detuned from the $|9/2, -7/2\rangle \rightarrow |9/2, -9/2\rangle$ transition by the molecule binding energy can create a Feshbach molecule. A schematic of the energy levels involved in the association is shown in Fig. 4.3.

To create molecules, a mixture of 3×10^5 Rb atoms and 1×10^5 K atoms are assembled in a trap with radial trapping frequencies of 211 and 136 Hz and axial trapping frequencies of 4 and 2 Hz, for K and Rb, respectively, at a temperature of $T/T_C = 0.8$ and a magnetic field of $B = 546.17$ G. A transverse rf field is applied with a frequency that is swept from 80.132 to 80.142 MHz in 2 ms. These frequencies correspond to the energy splitting between the $|9/2, -7/2\rangle$ and $|9/2, -9/2\rangle$ plus 90 to 100 kHz, spanning the 95 kHz molecule binding energy. The sweep creates Feshbach molecules via rf adiabatic rapid passage, and as discussed in §3.4, the number of molecules created can be measured with direct imaging.

The fraction of K atoms converted to molecules as a function of temperature is shown in Fig. 4.4. The temperature is varied by holding the mixture in the trap

for a variable time after the evaporation ends. Instabilities in the optical trap strength and position cause heating, resulting in an increase in temperature while the number of atoms remains constant. As expected, above T_C , the molecule fraction increases as the temperature decreases due to the increased phase space density, but decreases below T_C as the spatial overlap decreases. The solid line in Fig. 4.4 shows the molecule fraction predicted by the Monte Carlo simulation using $\gamma = 0.44$, and the dashed lines represent the uncertainty in the conversion due to uncertainties in the measured numbers, temperature, and trapping frequency. The predictions from the model are scaled by 0.70 to account for observed molecule losses due to collisions with unbound atoms on the timescale of the rf sweep.

While the Monte Carlo simulation was originally developed to describe molecule association by adiabatic magnetic-field sweeps through resonance, we expect that it will also describe Feshbach molecules created via rf association. The model was shown to correctly predict the fraction of atoms converted to molecules through a similar technique in ^{85}Rb by Thompson *et al.* [62]. In that experiment, atoms were prepared in the Fano-Feshbach resonant state, and molecules were associated by modulating the magnetic field at a frequency equal to the molecule binding energy. Here, we see that the simulation does correctly predict the fraction of atoms converted to molecules via rf association *and* for the case of a Bose-Fermi mixture.

Since we are able to accurately predict the molecule conversion efficiency with the Monte Carlo simulation, we can use it to design experiments to optimize the molecule fraction. The data in Fig. 4.4 were taken with a 3:1 Rb to K number ratio in a weak optical trap with significant gravitational sag between the two atomic gases. Now, we ask: how do these and other experimental parameters impact the molecule fraction?

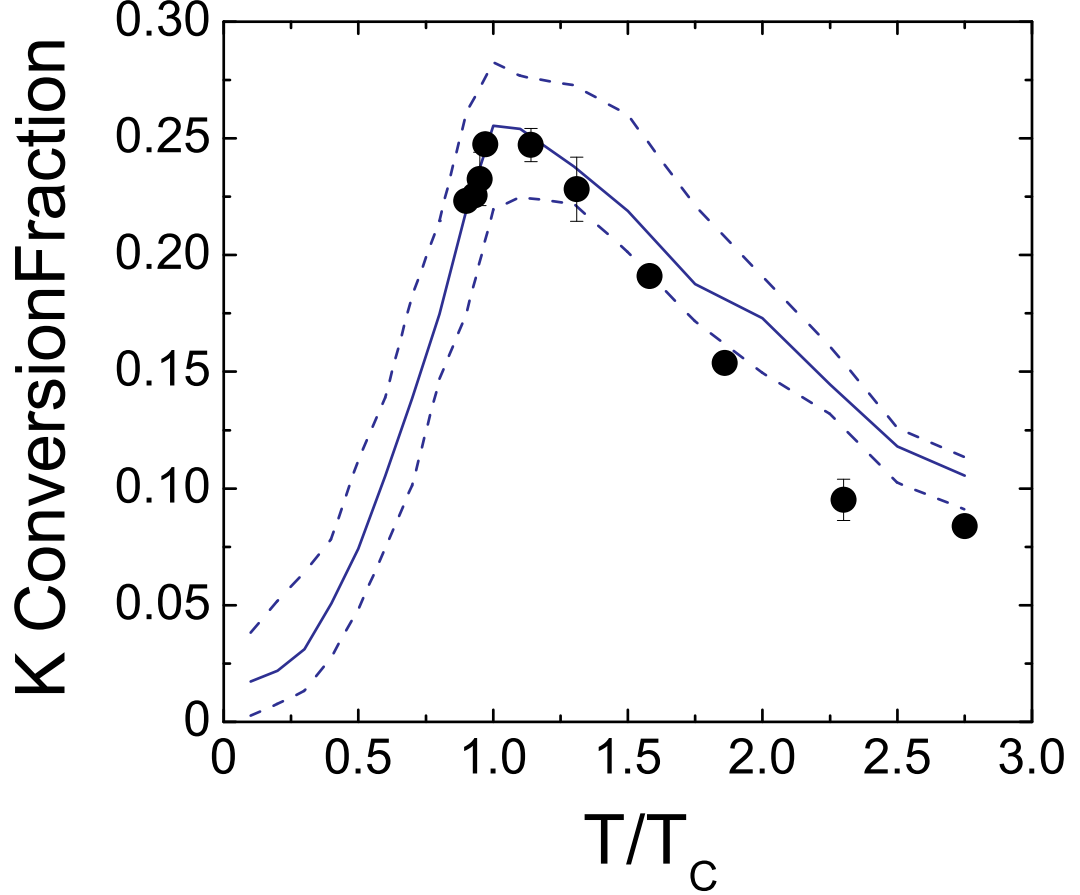


Figure 4.4: Temperature dependence of the molecule conversion in a Bose-Fermi mixture of ^{87}Rb and ^{40}K . The fraction of K atoms converted to molecules is plotted as a function of T/T_C for the Rb atoms. The solid circles (\bullet) are experimental data, while the lines are the result of the Monte Carlo simulation for $N_{\text{Rb}}/N_{\text{K}} = 3$, taking into account the effects of gravitational sag and uncertainties in the trap frequencies and atom numbers. This figure differs from Fig. 3 in Ref. [64] in that the data above T_C are shifted to higher temperature due to correcting an error in the calculated trapping frequencies. Also, the simulated conversion fraction has been scaled to correct for the atom-number dependence in the simulation, which results in lower conversion fraction below T_C and larger conversion fraction above T_C for larger atom number. The simulation was originally run for 16 000 atoms, while the experiment was performed with 400 000 atoms.

4.3.1 Number ratio

Let us consider the effect of the number ratio on molecule conversion. For the purpose of elucidation, we consider a mixture of equal numbers of two Boltzmann gases (atoms that are sufficiently hot that we need not consider whether the particles are bosons or fermions), which we label A and B . Let us assume that molecule conversion is less than one hundred percent. Now, if we double the number of particles in B while keeping the temperature fixed, we have doubled the number of possible partners for a given atom in species A . This is likely to increase the number of pairs that satisfy the phase space criterion Eq. 4.1, resulting in a larger fraction of species A converted into molecules.

As we have seen above, to associate a significant fraction of atoms into molecules, the atom gas must be nearly quantum degenerate. Therefore, we must take into account whether the atoms are bosons or fermions, and whether one species Bose condenses. Figures 4.5 and 4.6 show the results of the Monte Carlo simulation for a trapped mixture of fermionic ^{40}K and bosonic ^{87}Rb . As expected, the fraction of atoms of one species converted to molecules depends on the number of atoms in the other species. For all cases, the molecule fraction is maximized when $T = T_C$ as we have seen in Figs. 4.2 and 4.4. With an excess of fermions at T_C for the bosons (see Figs. 4.5 a and b), the simulation predicts 80% of the Rb population to be converted into molecules with a number ratio of $N_{\text{K}}/N_{\text{Rb}} = 3$, while a number ratio of $N_{\text{K}}/N_{\text{Rb}} = 4$ yields 90% conversion efficiency. For an excess of bosons, however, the molecule conversion fraction for the K atoms does not exceed 70% even with number ratios as high as $N_{\text{Rb}}/N_{\text{K}} = 25$.

To understand this difference we must consider the phase space density of each species individually. If the number of bosons at T_C is fixed and the number of fermions increases, the number of possible partners for the bosons increases,

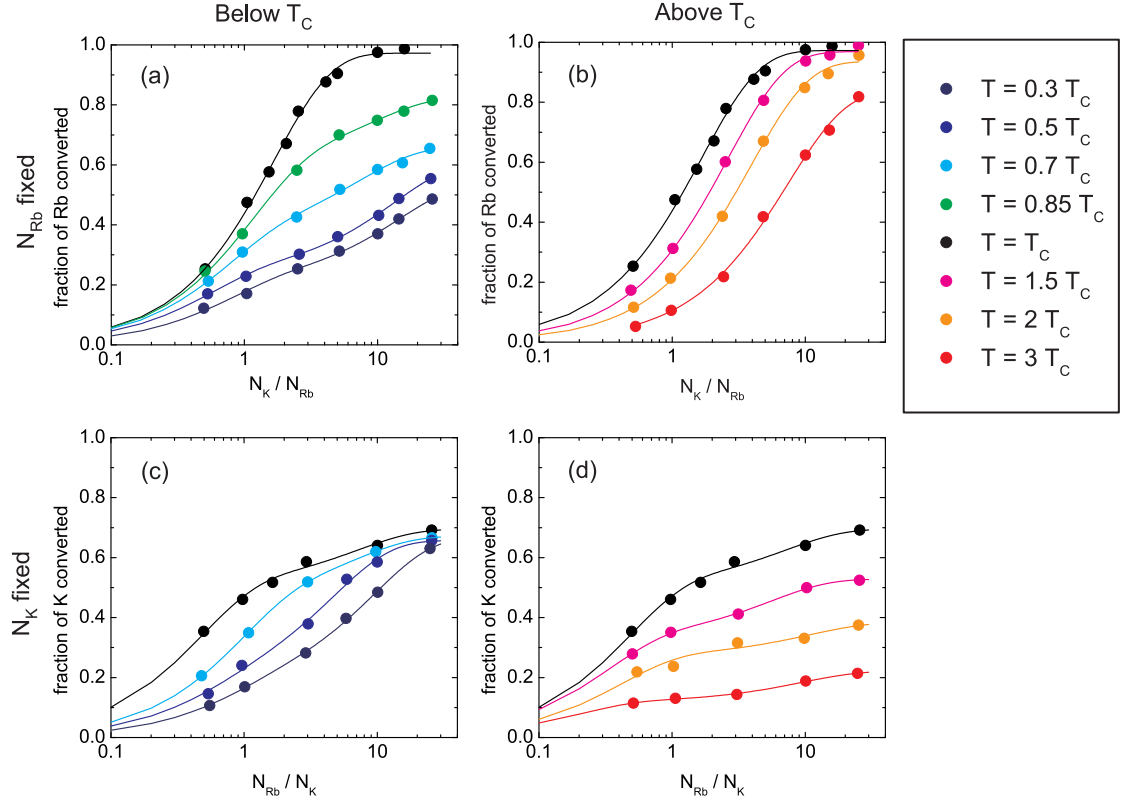


Figure 4.5: Effect of number ratio on molecule conversion for fixed T_C . Plotted are the results of the Monte Carlo simulation for molecule conversion for various temperatures and number ratios of K and Rb confined in an isotropic trap. (a) and (b) show the fraction of Rb atoms converted into molecules as a function of the ratio of K to Rb atoms with the Rb number fixed. Here, T_C is constant, but T/T_F decreases with increasing N_K . For clarity, (a) shows the conversion fraction for $T \leq T_C$, while $T \geq T_C$ is shown in (b). (c) and (d) show the fractional conversion of K atoms into molecules while varying the Rb number. Here, T_C and T/T_F increase with increasing N_{Rb} . Each closed circle (\bullet) represents a single run of the Monte Carlo simulation, and the lines, which are double-exponential fits, are intended only as a guide to the eye.

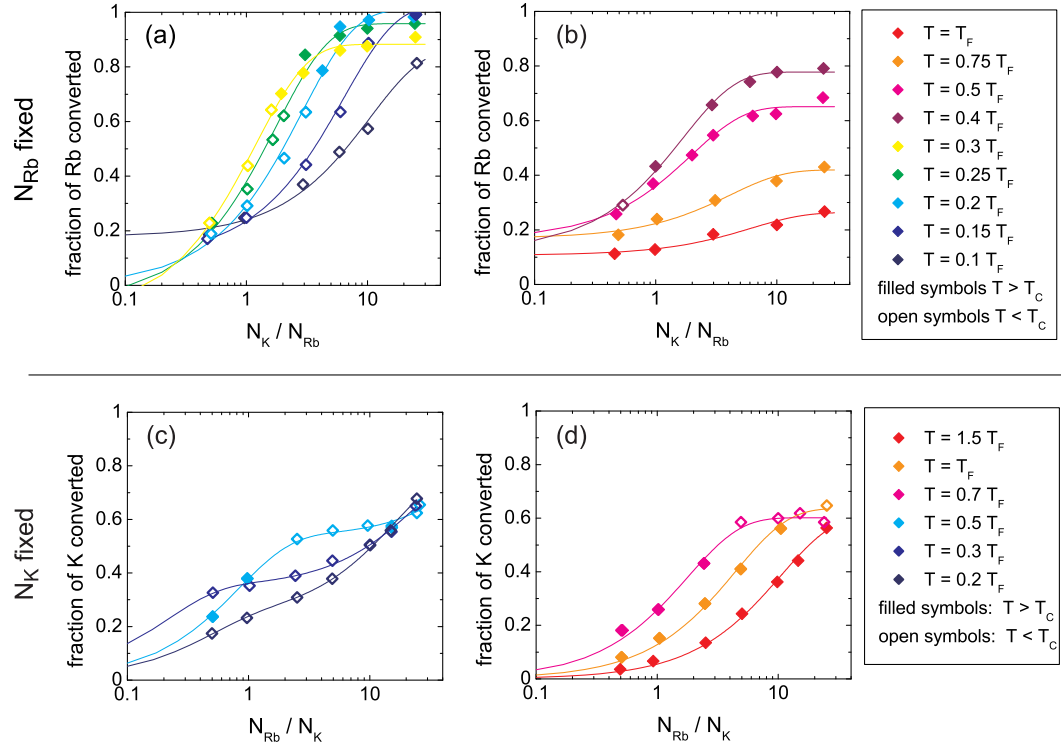


Figure 4.6: Effect of number ratio on molecule conversion for fixed T_F . Plotted are the results of the Monte Carlo simulation for molecule conversion for various temperatures and number ratios of K and Rb confined in an isotropic trap. The fraction of Rb atoms converted into molecules as a function of the ratio of K to Rb atoms with the Rb number fixed is shown in (a) and (b). Here, T is constant, and T/T_C increases with increasing N_K . The fraction of K atoms converted into molecules as a function of the ratio of Rb to K atoms with the K number fixed is shown in (c) and (d). Here, T is constant, and T/T_C decreases with increasing N_{Rb} . The filled symbols represent points where $T/T_C > 1$, and the open symbols represent points where $T/T_C < 1$. The lines are guides to the eye.

increasing the likelihood of making molecules (see Figs. 4.5a and b). Since the temperature is fixed and the number of fermions increases, the phase space density of the fermions increases. This increased phase space density results in an increase in the molecule fraction as in the simple example above. If, instead, we have a fixed number of fermions at T_C with varying boson number (see Figs. 4.5c and d), the situation becomes slightly more complicated. As the number of bosons increases, the number of possible partners for the fermions increases, but T_C increases as well. Since the number of fermions is fixed, the phase space density of the fermions decreases due to the increased temperature. It is this competition between the increased number of possible partners and the decrease in the phase space density of the fermions that leads to lower conversion fraction for an excess of bosons than an excess of fermions. Alternatively, we could fix the number of fermions and the temperature and vary the number of bosons as in Figs. 4.6c and d. In this case, the phase space density of the fermions remains constant. As the number of bosons increases, the number of possible pairs increases as does the phase space density of the bosons, leading to an increase in molecule conversion. If we began at T_C as in the previous example, any increase in number will cause the bosons to condense leading to a reduction in spatial overlap. Here, it is the competition between the increased number of partners and the reduced spatial overlap that leads to lower conversion fraction for an excess of bosons.

From the simulations, we find that by operating near T_C for the bosons with a modest excess of K atoms, we can expect the majority of the Rb atoms to be converted into molecules. We have compared this prediction with the number of atoms that disappear from detection in adiabatic sweep experiments. The mixture is prepared in an optical trap with radial trapping frequencies of 560 Hz for Rb and 730 Hz for K and axial frequencies of 7.2 Hz for Rb and 10.4 Hz for K. With $N_{\text{Rb}} = 7 \times 10^4$ and a number ratio of $N_{\text{K}}/N_{\text{Rb}} = 3.6 \pm 0.5$, the temperature of the

mixture, 350 nK, corresponds to $1.4 T_C$ for the bosons and $0.4 T_F$ for the fermions. Figure 4.7 shows experimental data for the number of Rb atoms remaining after a magnetic-field sweep through resonance as a function of the inverse ramp speed. If we assume all the missing atoms have been converted to molecules, the observed molecule fraction for adiabatic sweeps agrees well with the simulation. Here, we find that $(66 \pm 6)\%$ of the Rb atoms are converted to molecules. Note, however, that fewer than 20% of the K atoms are converted to molecules. From this point forward, I will use the term “molecule fraction” to mean the fraction of the lower-number species that is converted to molecules since the maximum possible number of molecules is set by the lower-number species.

4.3.2 Gravitational sag

The calculations in §4.3.1 assumed that the two species are spatially centered on the same point. In the experiment, the Rb and K atoms experience a different gravitational sag, causing the cloud centers to be separated in the vertical direction by an amount $\Delta y = g \left(\frac{1}{\omega_{\text{Rb}}^2} - \frac{1}{\omega_K^2} \right)$. Here, g is the acceleration due to gravity and ω_K and ω_{Rb} are the angular trapping frequencies in the vertical direction for K and Rb, respectively. Figure 4.8 shows the predicted molecule fraction as a function of the separation of the cloud centers. The molecule conversion begins to drop steeply when the cloud separation becomes comparable to the rms widths of the clouds. For the data in Fig. 4.4, the gravitational sag was nearly twice the rms widths of the clouds, resulting in a 30% reduction in the peak molecule conversion efficiency when compared with the case with no gravitational sag. However, the experiments in Fig. 4.7 and all of the experiments discussed in Chapters 3 and 5 were performed with clouds whose differential gravitational sag was less than half the rms cloud size, where the effects of sag on the molecule conversion can be safely neglected.

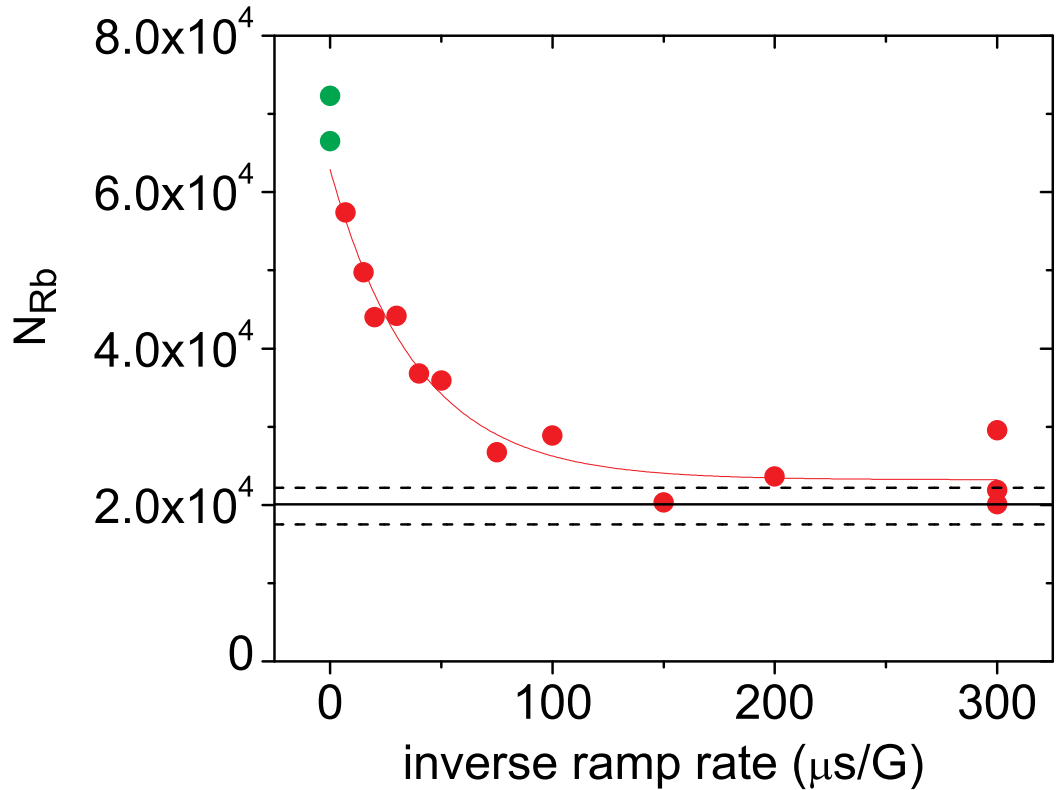


Figure 4.7: Adiabatic molecule conversion with an excess of fermions. Initially, a mixture is prepared with $N_{\text{K}}/N_{\text{Rb}} = 3.6 \pm 0.5$ at $T/T_C = 1.4$ (green points). The red points show the number of Rb atoms remaining after a magnetic-field sweep through resonance. The black solid line shows the Monte Carlo prediction for the number of atoms remaining after adiabatic molecule conversion, while the dashed lines represent the uncertainty in the molecule number due to the uncertainty in the initial atom numbers. The observed loss corresponds to $(66 \pm 6)\%$ of the Rb atoms.

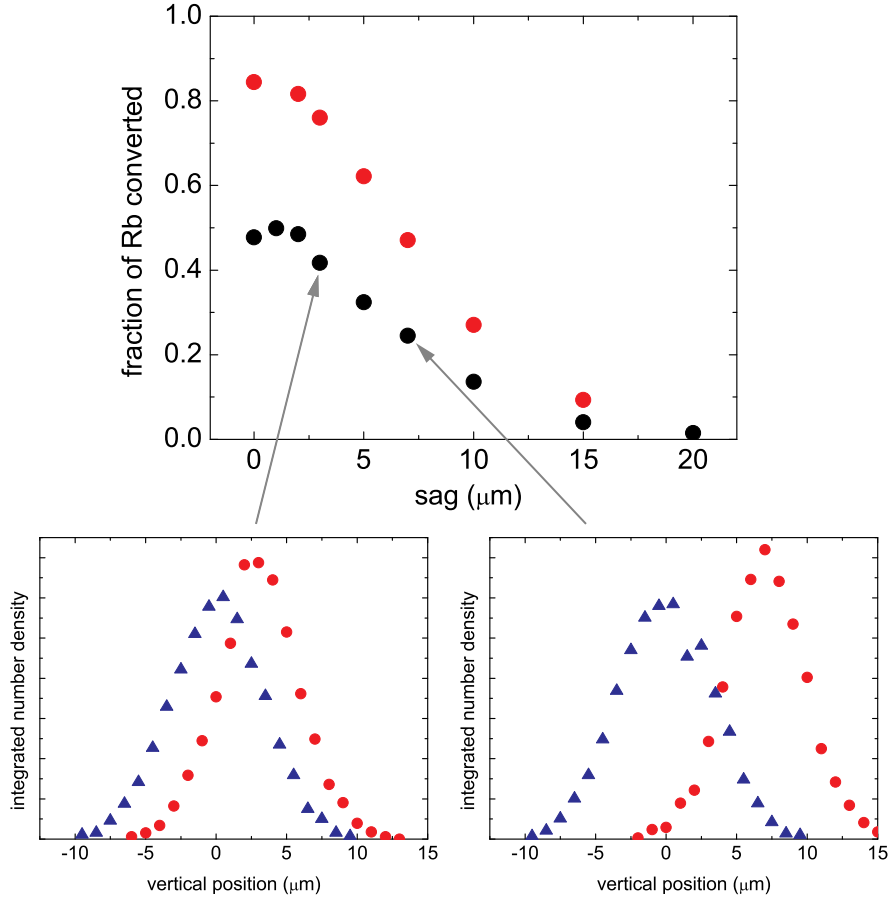


Figure 4.8: Effect of gravitational sag on molecule conversion. The upper plot shows the simulated molecule fraction as a function of the cloud separation for $N_{\text{K}}/N_{\text{Rb}} = 1$ (red circles) and $N_{\text{K}}/N_{\text{Rb}} = 3$ (black circles) at $T = T_C$ for atoms confined in an isotropic trap. The lower plots show the simulated vertical profiles of the integrated number density for Rb (red circles) and K (blue triangles) with cloud separations of 3 and 7 μm . The rms sizes of the clouds are 3 and 4 μm for the Rb and K clouds, respectively.

4.3.3 Molecule conversion in expansion

Some of the experiments that will be discussed in Chapter 5 required atomic gases with low densities. While there are many ways to reduce the density of a sample, one method we employed was to release the atoms from the trap, allowing the clouds to ballistically expand before creating molecules. When a cloud is released from the trap, the atoms fly apart with the momentum they had in the trap, rapidly increasing the spacing between particles (and, thus, reducing the density). This also has the effect of locally cooling the cloud. That is, as the cloud expands, it separates itself into velocity classes—the atoms that remain near the center of the cloud have small velocities, while the atoms that are on the outskirts of the cloud have the largest velocities. If we were to divide the cloud into shells, each shell would contain a smaller distribution of velocities than the initial cloud, effectively cooling the sample.

What impact does expansion have on the molecule fraction? The criterion for molecule creation requires $\Delta r_{\text{rel}}\Delta v_{\text{rel}}$ be small. The distribution of Δr_{rel} of all possible pairs increases as the cloud expands, while the distribution of Δv_{rel} remains the same. We might naïvely expect that the molecule fraction should simply be inversely proportional to the mean interparticle spacing. However, it is the product $\Delta r_{\text{rel}}\Delta v_{\text{rel}}$ that determines if a molecule is made. In expansion, an atom's position and momentum are correlated, so it becomes increasingly likely for two neighboring atoms (atoms with small Δr_{rel}) to have similar velocities (small Δv_{rel}). For the cases we have investigated with the Monte Carlo simulation, the molecule fraction decreases as the cloud expands, but the local cooling in the gas causes it to decrease more slowly when compared with a simple dilation of the cloud. Figure 4.9 shows the expected molecule fraction as a function of expansion time for two Bose gases with equal masses and identical position and momentum

distributions. The solid circles show the molecule fraction for a cloud of atoms whose positions follow the form

$$x_i(t) = x_{i0} + \frac{p_{i0}}{m} \cdot t, \quad (4.2)$$

where x_{i0} and p_{i0} are the atom's position and momentum in the trap, with the subscript $i = x, y, z$ representing the cardinal directions. m is the mass, and t is the expansion time. To identify the effect of local cooling in expansion, the Monte Carlo simulation was also performed for a simple dilation of the cloud (open circles in Fig. 4.9)

$$x_i(t) = x_{i0} \sqrt{1 + \omega_i^2 t^2}, \quad (4.3)$$

where ω_i are the angular trapping frequencies. The density of the atom cloud retains the proper dependence on expansion, but the momentum remains uncorrelated with position. Clearly, local cooling in expansion maintains a larger fraction of pairs with small relative velocity despite the increase in the interparticle spacing.

If, instead of identical atoms, we have two components with different masses and magnetic moments, we must additionally take into account the reduction in spatial overlap from the gases expanding at different rates. This is the case in our mixture of K and Rb. For expansion times long compared to the trapping period, the ratio of the sizes will become $\frac{\sigma_K}{\sigma_{Rb}} \approx \frac{\sigma_{0K}\omega_K}{\sigma_{0Rb}\omega_{Rb}}$, where $\sigma_{0K,Rb}$ represents the in-trap rms size of the atom cloud. The K trapping frequencies in the optical trap are typically 40 – 50% greater than the Rb trapping frequencies due mainly to the smaller mass but also due to additional trapping forces provided by the inhomogeneous magnetic field. For a mixture with similar sizes in the trap, the K cloud will rapidly become larger than the Rb cloud as they expand. Figure

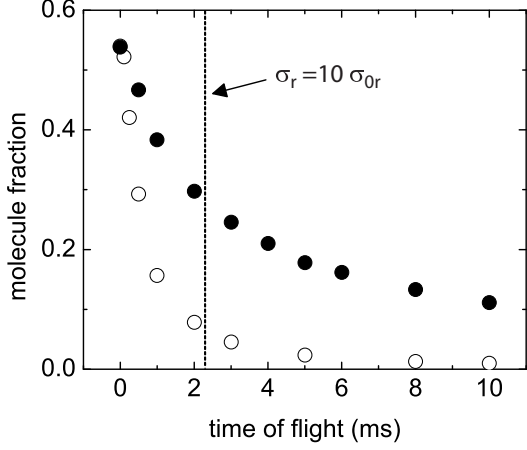


Figure 4.9: Molecule conversion in expansion for two identical Bose gases at $T = T_C$. The solid circles (\bullet) show the fraction of molecules converted in the Monte Carlo simulation as a function of expansion time from a trap with a radial trapping frequency of 690 Hz and an axial trapping frequency of 9.0 Hz. The atom clouds expand according to the atoms' momenta in the trap, causing the position and momentum of each atom to be correlated. For comparison, the open circles (\circ) show the molecule fraction for a dilation of the atom cloud, where the position of each atom is scaled by a constant factor, irrespective of its momentum. The density for a given expansion time is the same as that of the solid circles, but the momentum and position of a given particle are uncorrelated. At the dashed line, the radial size has increased tenfold.

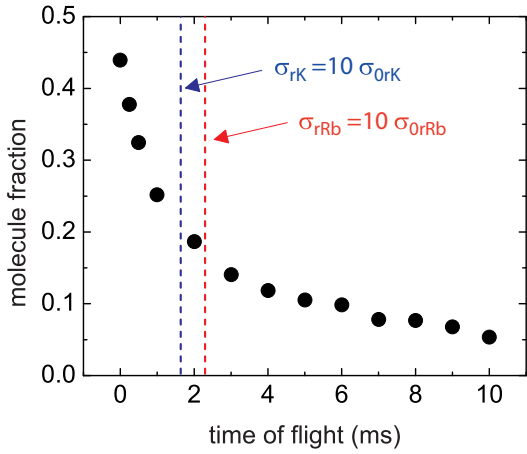


Figure 4.10: Simulation of molecule conversion in expansion for equal numbers of Rb and K at $T = T_C$. The K atoms experience trapping frequencies that are 1.4 times greater than the Rb trapping frequencies. The two atom clouds, whose sizes are initially similar, expand at different rates, causing a reduction in the spatial overlap at longer expansion times.

4.10 shows the expected molecule fraction for a gas with equal numbers of ^{40}K and ^{87}Rb at $T = T_C$. In comparison with Fig. 4.9, the expected molecule fraction decreases more rapidly with expansion time due to the mismatch of the spatial extent of the two species. After 2 ms of expansion from the trap, the density of the clouds has decreased by two orders of magnitude, while the molecule fraction has only decreased by a factor of 2.3. Therefore, we can access a wide range of densities with comparatively small effects on the molecule conversion by releasing the atoms from the trap before making molecules.

From the Monte Carlo simulations, we now have guidelines for maximizing the molecule fraction: (a) the temperature of the mixture must be near to T_C , (b) there should be more fermions than bosons, (c) the trap should be sufficiently tight in the vertical direction such that the differential gravitation sag is smaller than the rms size of the cloud, and (d) if we are willing to accept a hit in molecule conversion, we can allow the mixture to expand from the trap to access lower densities.

Chapter 5

Coherent atom-molecule oscillations

Armed with the knowledge of how to make large samples of molecules, we were then ready to look for coherent atom-molecule oscillations. After all, more molecules should translate to larger amplitude oscillations. In this chapter, I present our studies of atom-molecule coherence. Starting with an ultracold mixture of ^{87}Rb and ^{40}K atoms, we create superpositions of atom pairs and molecules. The superpositions are generated by pulsing an applied magnetic field near an interspecies Fano-Feshbach resonance to coherently couple atom and molecule states. Rabi- and Ramsey-type experiments show oscillations in the molecule population that persist as long as $150\ \mu\text{s}$ and have up to 50% contrast. The frequencies of these oscillations are magnetic-field dependent and are consistent with the predicted molecule binding energy. This new type of quantum superposition involves particles of different statistics (i.e. bosons and fermions). In the same spirit of experiments that showed that the coherence properties of a BEC are not necessary to observe spatial matter-wave interference [114], we show that coherent atom-molecule superpositions can be created without a BEC.

5.1 Rabi and Ramsey oscillations in the atom + photon system

The pioneering experiments of Rabi and Ramsey demonstrated some of the earliest examples of quantum control [47, 48, 49]. These experiments showed that

by resonantly coupling two quantum states with an external field, a superposition can be created and coherently manipulated. Probably the clearest example this type of quantum coherence is the system of a two-level atom in a near-resonant radiation field. This system is treated rigorously in many textbooks (see, for example, Ref. [89] and [115]), so I will only highlight some of the key points here. One particularly intuitive description of the atom + photon system is the so-called “dressed atom picture” in which the eigenstates of the atom are modified, or dressed, by a quantized radiation field. We consider the Hamiltonian

$$H = H_a + H_{\text{rad}} + H_{\text{int}}, \quad (5.1)$$

where H_a is the bare atom Hamiltonian, H_{rad} is the radiation energy, and H_{int} is the atom-field interaction that couples the atomic levels. A schematic of the energy level diagram of the the first two terms is shown in Fig. 5.1. The energy levels of the bare atom are shifted by $n \times \hbar\omega$, where n is the number of photons in the radiation field. If the photon energy $\hbar\omega$ is close to the energy difference between the ground and first excited state $\hbar\omega_0$, the interaction matrix H_{int} mixes the two states, creating the eigenstates $|1\rangle$ and $|2\rangle$, which are hybrids of the bare states $|e, n\rangle$ and $|g, n+1\rangle$ as shown in Fig. 5.2.

The interaction matrix can be written in the $\{|g, n+1\rangle, |e, n\rangle\}$ basis as

$$H_{\text{int}} = \hbar \begin{pmatrix} \delta & \frac{\Omega}{2} \\ \frac{\Omega}{2} & 0 \end{pmatrix}, \quad (5.2)$$

where the on-resonant Rabi frequency Ω is a measure of the coupling between the two states, which depends on the intensity of the field, and $\delta = \omega - \omega_0$ is the detuning of the radiation frequency from the transition frequency.¹ By diagonalizing H_{int} , we find the dressed states

¹ Here, time dependence has been eliminated by invoking the rotating wave approximation.

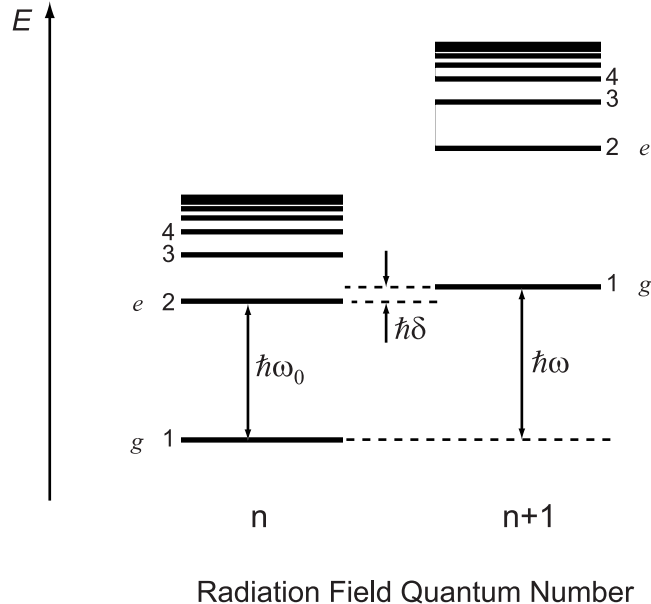


Figure 5.1: Energy level diagram for an atom in a radiation field. The energy levels of the bare atom are shifted by the energy in the radiation field, $n \times \hbar\omega$. When the photon energy approaches the level splitting $\hbar\omega_0$, the states $|e, n\rangle$ and $|g, n+1\rangle$ become nearly degenerate. (Figure adapted from Ref. [116].)

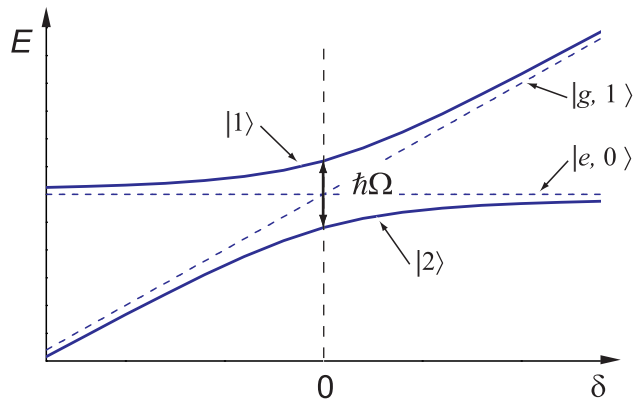


Figure 5.2: Eigenstates of the dressed atom. Plotted are the energies of the dressed states $|1\rangle$ and $|2\rangle$ as a function of the detuning of the radiation field from the atomic resonance (solid lines). The dashed lines represent the energies of the bare states $|e, 0\rangle$ and $|g, 1\rangle$. On resonance, the energy difference between the coupled states is $\hbar\Omega$.

$$|1\rangle = \sin \theta |g, n+1\rangle + \cos \theta |e, n\rangle \quad (5.3)$$

$$|2\rangle = \cos \theta |g, n+1\rangle - \sin \theta |e, n\rangle, \quad (5.4)$$

where $\tan 2\theta = -\frac{\Omega}{\delta}$, and the eigenenergies are $E = \frac{\hbar}{2} (\delta \pm \sqrt{\Omega^2 + \delta^2})$. As shown in Fig. 5.2, the dressed states $|1\rangle$ and $|2\rangle$ form the branches of a hyperbola whose asymptotes are the bare states $|e, n\rangle$ and $|g, n+1\rangle$, and their energy difference is $\Delta E = \hbar \Omega_{\text{eff}}$, where $\Omega_{\text{eff}} = \sqrt{\Omega^2 + \delta^2}$. The dressed atom picture results in an avoided crossing. If an atom begins in the ground state in a radiation field that is sufficiently detuned from resonance, it can be transferred to the excited state by adiabatically sweeping the radiation frequency through resonance. Precisely on resonance, the atom is in an equal superposition of ground and excited states. The probability of a transition from the ground state after a time t with the field at a fixed detuning is

$$P(t) = \frac{\Omega}{\Omega_{\text{eff}}} \sin^2 \left(\frac{\Omega_{\text{eff}} t}{2} \right). \quad (5.5)$$

The probability of finding the atom in the excited state oscillates in time, and the frequency corresponds to the energy difference between the dressed states. With an ensemble of atoms, the population in the excited state is $N \times P(t)$, where N is the number of atoms. On resonance, the population oscillates with 100% contrast. Away from resonance, the amplitude of these Rabi oscillations decreases, and the frequency increases.

The observation of Rabi oscillations can be a very precise method for measuring the energy difference between coupled energy states. However, precise frequency measurements require long interrogation times. For experiments, this means that the intensity and frequency of the radiation as well as any external fields must be constant in time. Ramsey's method of separated oscillatory fields

reduces these stability requirements by reducing the time the driving field interacts with the atoms.

Ramsey's method uses two short interaction pulses separated in time (or space) by a time of free evolution that can be long compared to the interaction time as shown schematically in Fig. 5.3a. If the time t_1 is chosen such that the atoms experience a $\pi/2$ pulse (that is, they undergo one quarter of a Rabi oscillation), the atoms will be in an equal superposition of ground and excited states after the pulse. During the time t_2 , the states evolve freely, acquiring a relative phase due to the energy difference between the two states. The second $\pi/2$ pulse interferometrically "reads out" the phase, with the final population in each state depending sinusoidally on the phase difference acquired during t_2 . This sequence is analogous to a Mach-Zehnder interferometer (see Fig. 5.3c). The first pulse acts as a beamsplitter, and the relative phase acquired during t_2 is analogous to the path length difference of the two arms of the interferometer. The second pulse can be thought of as the second beamsplitter, which recombines the two paths, with the intensity at the detector depending on the interference of the two beams. If the pulses in a Ramsey experiment are not $\pi/2$ pulses, the resulting oscillations will have less than 100% contrast, as in the case of an interferometer with beamsplitters that are not 50/50.

As we have seen above and in Chapter 3, the systems of an atom in a radiation field and two atoms colliding near a Fano-Feshbach resonance can both be described by an avoided crossing between two coupled energy states. In the former system, two internal states of an atom are coupled by a near-resonant oscillating field. In the latter system, the state of two free atoms is coupled to that of a bound molecule by a magnetic field. As in the atom + photon system, atoms near a Fano-Feshbach resonance can undergo Rabi and Ramsey oscillations. The population can oscillate between unbound atom pairs and bound

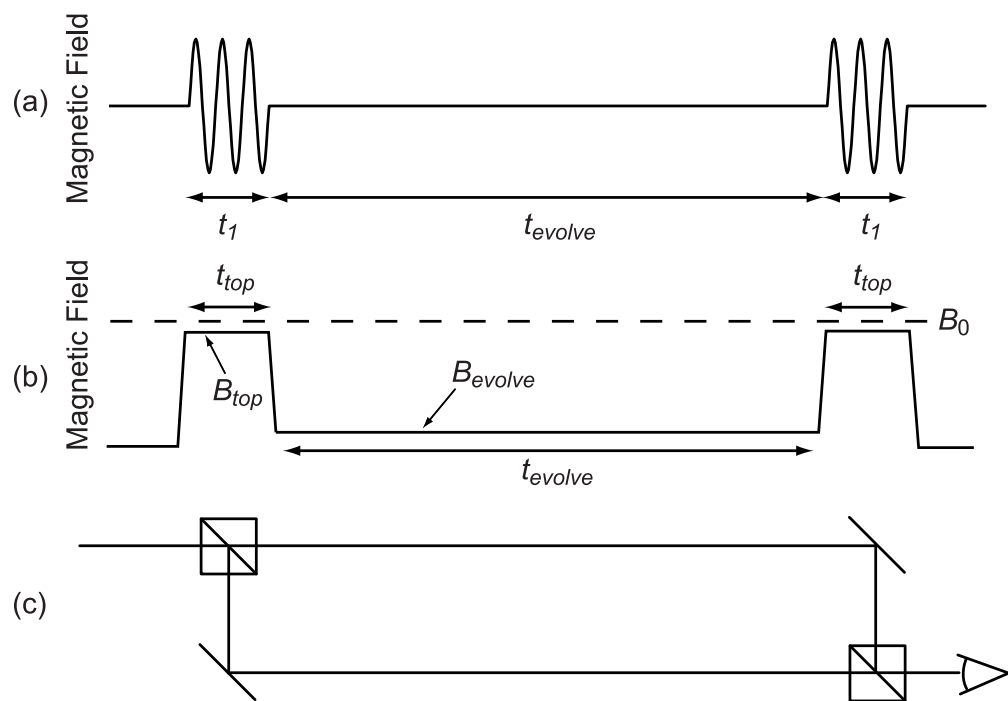


Figure 5.3: Ramsey's method of separated oscillatory fields and analogous systems. (a) Ramsey's method. Two oscillatory fields are applied for a short time t_1 , separated by a free evolution time t_{evolve} . (b) Schematic of the magnetic-field pulse sequence to observe Ramsey-like oscillations between atoms and molecules near a Fano-Feshbach resonance (B_0). (c) A Mach-Zehnder optical interferometer.

molecules. Figure 5.3b shows a schematic of a magnetic-field sequence used in our experiment to induce Ramsey oscillations between atoms and molecules. Here, the two oscillating fields are replaced by two pulses toward resonance. As discussed in Refs. [117] and [8], the first pulse creates a coherent superposition of atoms and molecules by providing overlap between the interparticle spacing (which is typically $10\,000\,a_0$ in experiments) and the mean dimer size

$$\langle r \rangle = \frac{a}{2}, \quad (5.6)$$

where a is the s -wave scattering length, which diverges at the resonance. The superposition evolves during the time t_{evolve} according to the energy difference between the atom and molecule states at B_{evolve} . The second pulse overlaps the states again, such that the final population in each state depends on the relative phase between the atom and molecule states at the end of t_{evolve} .

5.2 Criteria for observing oscillations

I have argued above that the system of two atoms near a Fano-Feshbach resonance is analogous to that of a two-level atom in a radiation field. Theoretically, Rabi- and Ramsey-type atom-molecule oscillations can be observed, but what are the criteria for experimental observation? Previous experiments that observed atom-molecule oscillations began with identical bosons prepared in a single energy state in either a BEC or a tightly confining optical lattice [44, 45, 54]. We pose the questions: Can an atom-molecule superposition be demonstrated with an incoherent ensemble of atoms, such as non-condensed bosonic atoms, fermionic atoms [55, 56, 57], or a mixture of different atomic species [58, 59]? As demonstrated below, the answer to this question is yes, but there are several criteria that must be met to observe atom-molecule oscillations.

For any Rabi or Ramsey experiment, we require a detection technique that

distinguishes between the two coupled states. As discussed in Chapter 3, we can selectively image either unbound atoms or molecules. We also need the coherence time of the oscillation to be long compared with its period. If the coherence time is too short (or the period too long), the oscillations will be overdamped, and no oscillations will be observed. It is this criterion that can make a BEC or optical lattice advantageous, though not necessary. A pair of atoms will oscillate with a frequency defined by the energy difference between the atom pair and molecule states. If every atom pair has the same energy, and all the molecules also share a single energy state, then all of the pairs will oscillate with the same frequency. Then the coherence time is likely to be limited by collisions, molecule loss, or spatial inhomogeneities in the magnetic field. In our Bose-Fermi mixture, the atom pairs are described by a distribution of energies. This leads to a distribution of oscillating frequencies, which will cause the macroscopic population oscillation to dephase in time. Narrower energy distributions should lead to longer coherence times, implying that mixtures with low absolute temperatures will have the longest coherence times.

Additionally, we require magnetic-field ramps that are sufficiently fast to induce oscillations. If magnetic-field ramps such as those drawn in Fig. 5.3b are too slow, an atom pair state will adiabatically follow an eigenstate toward and away from resonance, and no oscillations will be observed. Diabatic ramps are necessary to project the atom pair state into multiple states for the final population to oscillate. The magnetic-field ramp rate required for diabaticity depends on the density of the sample [86, 118, 61]. As discussed in §2.6, our magnetic-field ramp durations cannot be shorter than $5 \mu\text{s}$, and a typical ramp to induce atom-molecule oscillations spans 0.5 G, resulting in a typical maximum ramp speed of 100 G/ms. With these ramp speeds, we have found that we only observe oscillations in mixtures with peak densities $\lesssim 3 \times 10^{13} \text{ cm}^{-3}$ (see §5.3.3

and 5.4.2).

5.3 Ramsey oscillations

In this section, I discuss the experimental observation of Ramsey-type oscillations in our Bose-Fermi mixture. We began with a Ramsey experiment (as opposed to the conceptually simpler Rabi experiment) because in the ^{85}Rb experiment that first demonstrated atom-molecule oscillations, Rabi-like oscillations were only observed “over a very limited range” of magnetic fields [44].

The details of the experimental apparatus are described in Chapter 2. Here, I describe the experimental conditions for our observations of Ramsey oscillations in the trapped mixture, which henceforth will be referred to as the “typical intrapar trap conditions.” We prepare an ultracold Bose-Fermi mixture of ^{87}Rb atoms in the $|1, 1\rangle$ state and ^{40}K atoms in the $|9/2, -9/2\rangle$ state. The atoms are confined in a far-off-resonance optical dipole trap formed by a single laser beam with a wavelength of 1090 nm focused to a $1/e^2$ radius of 18 μm . The gas mixture is evaporatively cooled by decreasing the power of the optical-trap beam. Following the evaporation, the optical trap power is adiabatically increased so that the final measured trap frequencies are 350 Hz for Rb and 490 Hz for K in the radial direction and 5.2 Hz for Rb and 8.1 Hz for K in the axial direction. In this trap, we have 8×10^4 Rb atoms and 2×10^5 K atoms at a temperature of 200 nK, which corresponds to $1.2 T_C$ and $0.3 T_F$, where T_C is the critical temperature for Bose-Einstein condensation of the Rb gas and T_F is the Fermi temperature of the K gas. These conditions correspond to the criteria for large molecule fraction discussed in the previous chapter. The peak densities of the Rb and K clouds are $n_{\text{Rb}}^0 = 1.1 \times 10^{13} \text{ cm}^{-3}$ and $n_{\text{K}}^0 = 1.3 \times 10^{13} \text{ cm}^{-3}$, respectively. During the evaporation, we turn on an applied magnetic field of 542 G, preparing the mixture near to the interspecies Fano-Feshbach resonance at $B_0 = 546.76\text{G}$.

5.3.1 Empirical optimization

We began looking for oscillations with a magnetic-field sequence similar to that used in the ^{85}Rb double-pulse experiment [44] with the parameters scaled to account for the different density, background scattering length, and resonance width in our mixture. The sequence is shown schematically in Fig. 5.3b. At the end of the sequence, we image the molecule cloud with the technique discussed in §3.4. After significantly reducing the density of atoms in the trap (for a discussion see §5.3.3 below), we were able to observe oscillations in the molecule number with amplitudes of nearly 5 000 molecules. To maximize the molecule oscillation amplitude, we then set about empirically optimizing each of the magnetic-field ramp parameters.

Figure 5.4 shows some of the optimizations of the magnetic-field sequence. In these experiments, the amplitude of the oscillation in the molecule population was measured with $B_{\text{evolve}} = 546.1$ G, and each parameter (B_{start} , B_{top} , t_{top} , and all the ramp speeds) was varied in turn. Note that a multidimensional optimization in parameter space was not performed.² Although, in retrospect, such a search, particularly between t_{top} and B_{top} , would have ensured a global maximum in the oscillation amplitude. From the optimizations, we can make several observations. The dependence on B_{top} (Fig. 5.4b) indicates that for a hold time of 15 μs , the largest amplitude oscillation is not at the Feshbach resonance, but at 546.6 G. If we assume that the maximum occurs when the pulse corresponds to a $\pi/2$ pulse, this would imply a Rabi frequency of $2\pi \times 17$ kHz at 546.6 G, but, as we shall see below, we were unable to observe Rabi flopping under these conditions. The decay of the amplitude as the pulse approaches the resonance may, instead,

² By this, I mean fixing the value of one parameter, say t_{top} , and varying the value of another, say B_{top} , then choosing another t_{top} and varying B_{top} , and so on, until an optimum is found in the 2D space.

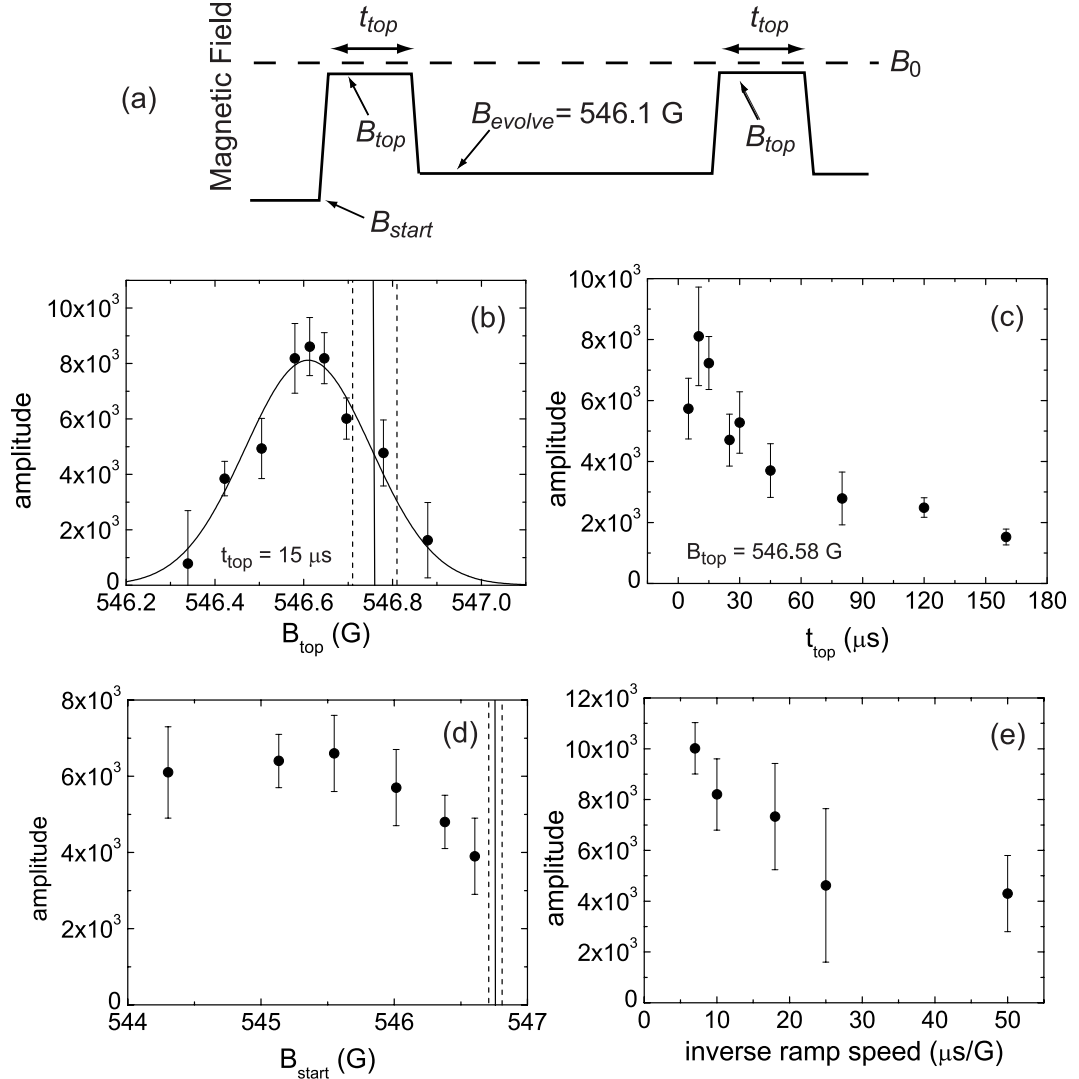


Figure 5.4: Empirical optimization of Ramsey oscillations. A schematic of the magnetic-field pulse sequence is shown in (a) with the optimization parameters labeled. In (b)-(d), the oscillation amplitude was measured over two to four periods of the oscillation at B_{evolve} . Plotted in (b) is the amplitude as a function of the pulse height with $t_{top} = 15 \mu\text{s}$. (c) shows the dependence on t_{top} , the hold time at $B_{top} = 546.58 \text{ G}$. The amplitude as a function of the starting field for the first pulse is shown in (d). As a representative plot for the ramp speed optimization, the amplitude as a function of the inverse ramp speed for the third ramp is shown in (e). The vertical lines in (b) and (c) indicate the position of the Fano-Feshbach resonance and its uncertainty.

be due to increased collisions causing decoherence on the timescale of the pulse. The interspecies collision rate is given by

$$\Gamma_{\text{KRb}} = \langle n_{\text{KRb}} \rangle \sigma \langle v \rangle. \quad (5.7)$$

Here, $\langle n_{\text{KRb}} \rangle = \frac{1}{N_<} \int n_{\text{K}}(r) n_{\text{Rb}}(r) d^3 r$, where n_{K} and n_{Rb} are the number density of K and Rb, respectively, and $N_<$ is the number of atoms in the species with fewer atoms. $\langle v \rangle = \sqrt{8k_b T / (\pi \mu)}$ is the mean relative velocity between K and Rb atoms at a temperature T , where μ is the K and Rb reduced mass and k_b is the Boltzmann constant, and $\sigma = 4\pi a^2$ is the interspecies collision cross section with the scattering length a given by Eq. 3.1. Above 546.6 G, Γ_{KRb} exceeds 30 kHz, and we expect that any particle colliding with an atom pair would destroy the atom-molecule superposition. Similarly, the time dependence in Fig. 5.4c may indicate a Rabi frequency or increased decoherence due to spending too much time near the resonance.

In Fig. 5.4d, the amplitude of the oscillation is shown as a function of the magnetic field at which the first pulse starts. We find that the pulse must start below 546 G for maximum amplitude. This corresponds to a detuning of 0.8 G, which is smaller than the peak-to-zero width of the Fano-Feshbach resonance, $\Delta = 3.6$ G [64]. Though, the decrease in amplitude near the resonance is most likely due to slower ramp speeds. Recall from §2.6 that we are limited to ramp speeds of $\dot{B}_{\text{max}} = \frac{B_{\text{top}} - B_{\text{start}}}{5 \mu\text{s}}$. Below 546 G, the ramp speeds are 140 G/ms (7 $\mu\text{s}/\text{G}$), but at 546.6 G, the maximum ramp speed is 30 G/ms (30 $\mu\text{s}/\text{G}$). In Fig. 5.4e, we see that slower ramps (larger inverse ramp speeds) induce smaller oscillations. For the 0.7 G ramp in Fig. 5.4e, the maximum ramp speed is 140 G/ms, which is 5× faster than the $1/e$ ramp speed required for adiabatic molecule conversion at these densities (see Fig. 4.7). When these ramp speeds become comparable, the oscillation amplitude drops to about half the maximum value.

The optimized pulse sequence begins after a slow (3 G/ms) ramp to 545.80 G and consists of two trapezoidal pulses with 15 μs holds at $B_{\text{top}} = 546.58$ G, separated by a variable hold time t_{evolve} at B_{evolve} . The outer ramps have speeds of 140 G/ms, while the inner ramps have speeds of \dot{B}_{max} . This optimized sequence results in oscillations with peak-to-peak amplitudes of 10^4 molecules, which is 10% of N_{Rb} . At B_{top} , the calculated molecule size is 1800 a_0 ; this is comparable to the typical distance between nearest-neighbor Rb and K atoms, which is approximately $\langle n_{\text{KRb}} \rangle^{-1/3} = 10\,500 a_0$.

Figure 5.5 shows the measured molecule population N_{mol} after the optimized double pulse for two different values of B_{evolve} . The right-hand axes show the number of molecules normalized by the number of molecules created by an adiabatic sweep through resonance N_{max} . The number of molecules oscillates as a function of t_{evolve} , as expected for an atom-molecule superposition. Note, however, that the peak-to-peak amplitudes of the oscillations are only 30% of N_{max} .

5.3.2 Frequency dependence on B

The data in Fig. 5.5a and 5.5b show markedly different oscillation frequencies. We have measured the oscillation frequency for various values of B_{evolve} and find that the frequency corresponds to the predicted binding energy of the molecules. Figure 5.6 shows the measured oscillation frequency ν_{osc} as a function of magnetic field. The solid curve is a fit to the universal prediction for the molecule binding energy near the resonance [119],

$$E_b = \frac{\hbar^2}{2\mu_{\text{KRb}}(a - \bar{a})^2}. \quad (5.8)$$

Here, μ_{KRb} is the ^{40}K and ^{87}Rb reduced mass, $\bar{a} = 68.8 a_0$ is the van der Waals length of the long range potential, and $a = a_{\text{bg}}[1 - \Delta/(B - B_0)]$ is the *s*-wave scattering length with $a_{\text{bg}} = -185 a_0$ [92]. From the fit, we extract the resonance

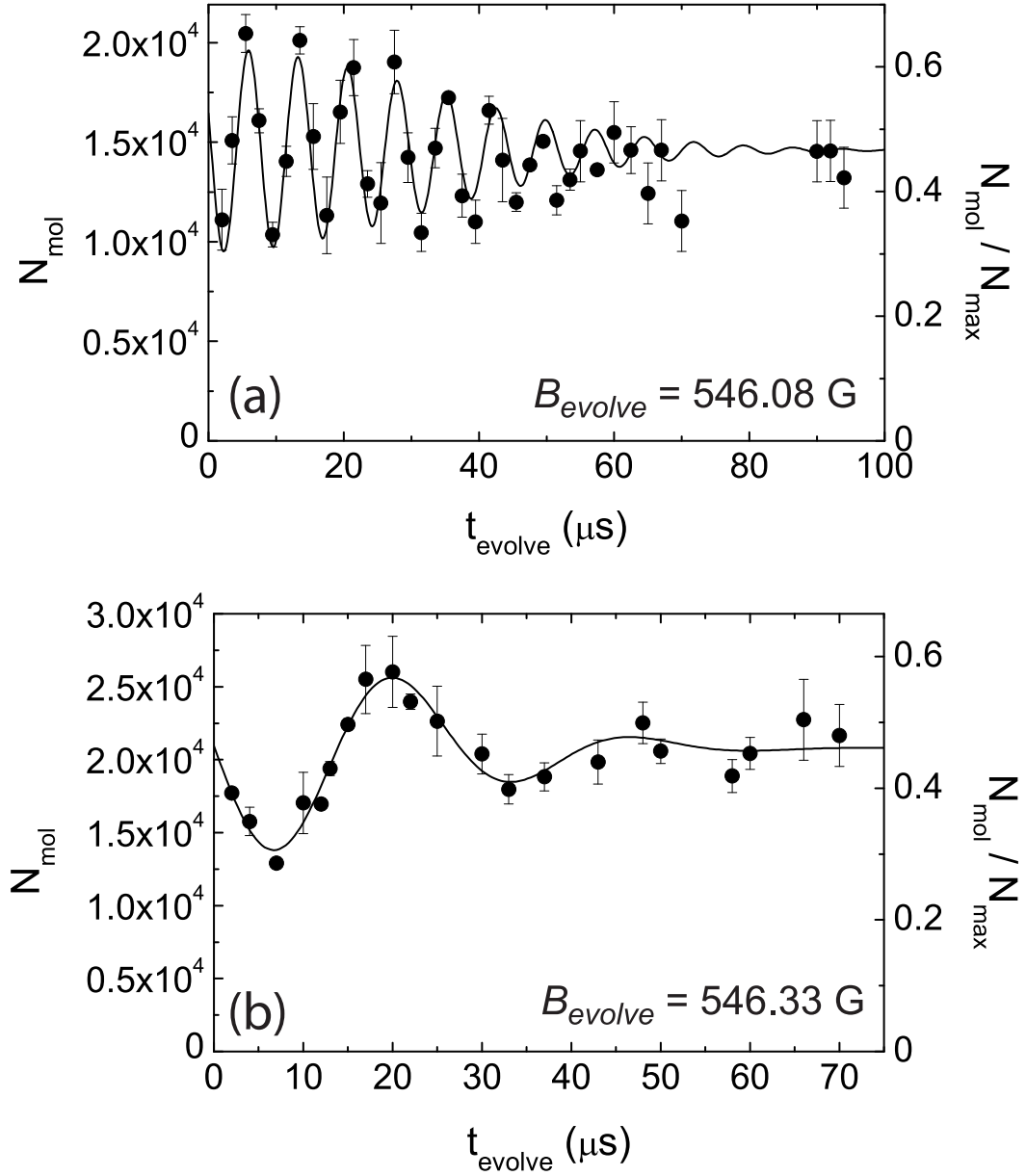


Figure 5.5: Ramsey-type atom-molecule oscillations. The molecule number N_{mol} is shown as a function of the hold time at $B_{\text{evolve}} = 546.08 \text{ G}$ in (a) and 546.33 G in (b), which correspond to detunings from the Fano-Feshbach resonance of $\Delta B = 0.68 \text{ G}$ and 0.43 G , respectively. The right-hand axes show the measured molecule number normalized by the maximum number of molecules associated by an adiabatic sweep through resonance, N_{max} . The lines are fits to $N_{\text{mol}} = Ae^{-t^2/(2\sigma^2)} \sin(2\pi\nu_{\text{osc}}t - \phi) + y_0$, yielding an oscillation frequency $\nu_{\text{osc}} = (136.5 \pm 1.3) \text{ kHz}$ and rms damping time $\sigma = (32 \pm 5) \mu\text{s}$ for the data in (a) and $\nu_{\text{osc}} = (36 \pm 2) \text{ kHz}$ and $\sigma = (22 \pm 4) \mu\text{s}$ for the data in (b).

position $B_0 = (546.76 \pm 0.06)$ G and width $\Delta = (-3.6 \pm 0.1)$ G, in agreement with Ref. [64]. The width is larger than the theoretical width quoted in Ref. [92].

5.3.3 Amplitude dependence on density

Prior to the observations of the atom-molecule oscillations discussed above, we attempted to induce Ramsey oscillations in mixtures with peak densities of $5 \times 10^{13} \text{ cm}^{-3}$, resulting in no observable oscillations. In the ^{85}Rb experiment, it was observed that when the density of the BEC was increased by an order of magnitude, the fractional amplitude of the oscillations significantly decreased [3]. We reasoned that we might be operating with prohibitively large densities, so we reduced the density of our trapped mixture to the conditions described above and were immediately rewarded with oscillations. Figure 5.7 shows the observed oscillation amplitude as a function of the peak K density. For these data, the mixture is initially prepared in the typical in-trap conditions. To vary the density, the power in the optical trap is then increased, resulting in the larger trapping frequencies. The number in each species and ratio of Rb and K densities remain relatively constant while the density varies. Note that the temperature of the gases increases with increasing density, but the measured T/T_C and T/T_F of the sample remain constant. Since molecule conversion via magnetic-field sweeps depends on the phase space density of the sample and not on the absolute temperature [61], we might expect that the amplitude of oscillations induced by magnetic-field pulses should also be independent of temperature. Therefore, we ascribe the decrease in oscillation amplitude to the increase in density.³ There are a number of possible explanations for the amplitude of the oscillations to decrease as the density increases. The criterion for adiabaticity depends on density [61, 86], so

³ We did not measure N_{\max} as a function of density, but as in the single-species case [61], we expect N_{\max} to be density-independent.

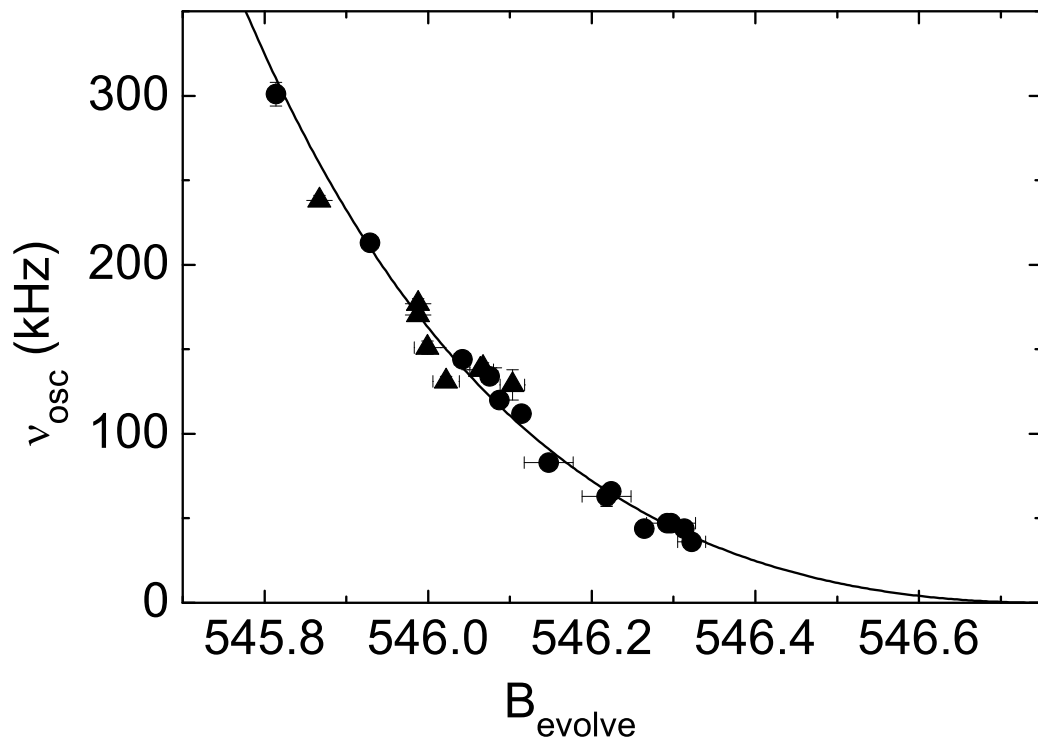


Figure 5.6: Magnetic-field dependence of the measured oscillation frequency for the molecule number in Ramsey-type double-pulse experiments. The circles (\bullet) correspond to double-pulse experiments performed with the atoms confined in the optical trap, while the triangles (\blacktriangle) represent experiments performed after 1 ms of expansion from the trap. The solid line is a fit to the universal prediction for the molecule binding energy given by Eq. 5.8 yielding the resonance position $B_0 = (546.76 \pm 0.06)$ G and width $\Delta = (-3.6 \pm 0.1)$ G.

as the density increases, the “fast” ramp speeds become less and less diabatic and are less able to create the atom-molecule superposition necessary to observe oscillations. For these data, the magnetic-field ramp speeds are 100 G/ms, which is 3.8 times faster than the $1/e$ ramp speed ($\beta = (26 \pm 7)$ G/ms) for adiabatic molecule creation at a K density of 1×10^{13} cm $^{-3}$ (see Fig. 3.5c). At a density of 3×10^{13} cm $^{-3}$, we expect the adiabatic ramp speed to be 3×26 G/ms = 78 G/ms, which is comparable to the ramp speed of the pulses. As we have seen in Fig. 5.4e, when these speeds become comparable the oscillation amplitude drops by a factor of two. Also, increased density causes an increase in the collision rate, which could increase the rate of decoherence of the superposition. Another possible cause for the reduced amplitude with increased density is an increase in the spread of relative velocities of the atom pairs due to the increased temperature (see §5.5.1). If this were a significant effect, we would expect the decreased amplitude to be accompanied by shorter coherence times, but we observe similar coherence times. Whatever the cause, it seemed clear that further lowering the atom densities was likely to increase the oscillation amplitude.

5.3.4 Ramsey oscillations in expansion

In general, it can be difficult to significantly alter the density of atoms in the trap. The factor of 5 reduction in density we had already achieved was introducing instabilities in the daily running conditions. To further reduce the density in the trap seemed a tall order. One simple method of reducing the density of the atomic gas is to allow the cloud to ballistically expand from the trap. With small changes to the expansion time, the density can change by orders of magnitude.

For experiments performed in expansion, we were no longer concerned with reducing the density in the trap and were able to load all of our atoms into the optical trap. At the end of evaporation, we have 1×10^6 Rb atoms and 6×10^5 K

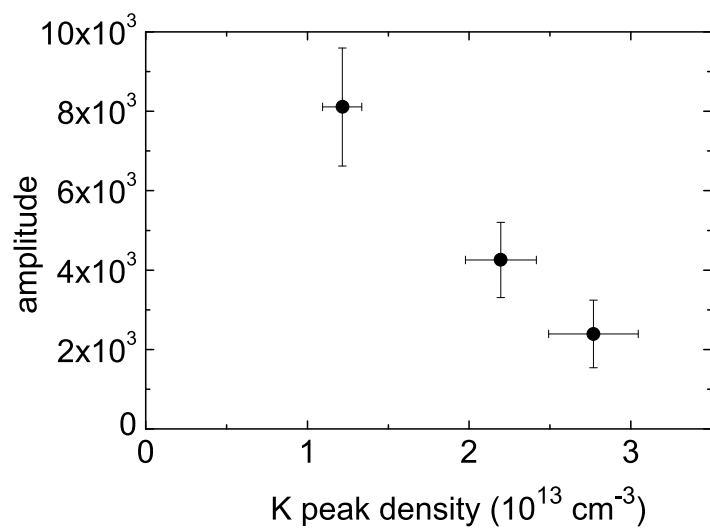


Figure 5.7: Density dependence of the molecule oscillation amplitude in Ramsey-type experiments. Plotted are the amplitudes of the molecule population oscillations for various densities achieved by varying the trapping frequency of the optical trap.

atoms at 1200 nK in an optical trap with radial trapping frequencies of 690 and 970 Hz for Rb and K, respectively. The temperature corresponds to $T/T_C = 1.6$ for Rb and $T/T_F = 0.7$ for K. After 1 ms of expansion, the peak densities are $n_{\text{Rb}}^0 = 3 \times 10^{12} \text{ cm}^{-3}$ and $n_{\text{K}}^0 = 7 \times 10^{11} \text{ cm}^{-3}$. For these conditions, which will be referred to as the “typical expansion conditions”, we find N_{max} is $(9.2 \pm 0.6) \times 10^4$, which is 15% of N_{K} , and the $1/e$ ramp speed for adiabaticity is $(9.1 \pm 1.0) \text{ G/ms}$.

The double pulse sequence was again empirically optimized for these new conditions. Again we found that the optimum amplitude was achieved with our fastest ramp speeds, but the optimum time spent near the resonance increased. Figure 5.8 shows the oscillation amplitude as a function of t_{top} . At $B_{\text{top}} = 546.58 \text{ G}$, we observe an optimum in the hold time at $50 \mu\text{s}$. This implies a Rabi frequency of $2\pi \times 5 \text{ kHz}$, in agreement with the expected frequency from the binding energy curve in Fig. 5.6. The triangles in Fig. 5.6 correspond to experiments performed after 1 ms of expansion using a hold time of $50 \mu\text{s}$ at the top of the optimized pulses. The goal of performing experiments after allowing the gas to expand was to increase the oscillation amplitude, but the observed amplitude did not increase. This is likely due to a competition between larger oscillations due to lower densities and smaller molecule fractions due to decreasing phase space density as the cloud expands (see §4.3.3). As discussed below, the low densities achieved by releasing the atoms from the trap did, however, enable the observation of Rabi oscillations.

5.4 Rabi oscillations

5.4.1 Ramsey oscillations without Rabi oscillations?

Since we can observe clear Ramsey oscillations, and Ramsey oscillations are induced by two pulses that are ideally each one quarter of a Rabi oscillation, shouldn’t we be able to observe Rabi oscillations? Under this supposition, we

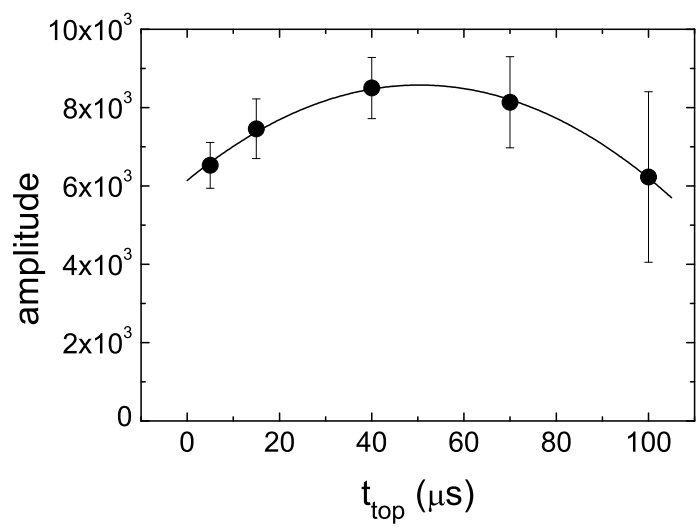


Figure 5.8: Empirical optimization of pulse time for a cloud after 1 ms of expansion from the trap. The line is a parabolic fit to identify the optimum t_{top} .

began to look for Rabi oscillations with single pulses toward the Fano-Feshbach resonance. However, as shown in Fig. 5.9, single-pulse experiments under the same conditions (typical in-trap conditions) as successful double-pulse experiments do not yield oscillations in the molecule population. Instead, we observe a monotonic increase in the molecule number that exponentially approaches a value less than N_{\max} . If we take this to be a critically damped oscillation, we can take the calculated frequency as an upper limit on the oscillation frequency at B_{top} . For the green data, whose B_{top} is similar to that used in the double pulse experiments, we estimate a Rabi frequency of $\leq 2\pi \times (5.1 \pm 0.7)$ kHz. This is in better agreement with the $2\pi \times 3.5$ kHz we would expect from the binding energy curve in Fig. 5.6 than with the $2\pi \times 17$ kHz implied by the empirical pulse optimization (see Fig. 5.4). These data indicate that decoherence mechanisms on the timescale of 10's of microseconds prevent the observation of Rabi oscillations. How, then are we able to observe Ramsey oscillations?

We can think of the $15\text{-}\mu\text{s}$ pulses in the Ramsey-type experiments as being sub- $\pi/2$ pulses. Just as in the atom-photon system, if the pulse duration is shorter than a $\pi/2$ pulse, the resulting superposition will not be a 50/50 mixture of two states. Instead, the superposition will favor the initial state, which in our case is the unbound atom pair state. When two of these sub- $\pi/2$ pulses are applied in a Ramsey-type experiment, the population in each state will still oscillate. The two pulses will not be able to transfer the entire population out of the initial state, though, resulting in oscillations with smaller amplitudes than in the ideal case. This may explain why our Ramsey oscillations do not span the total possible molecule number.

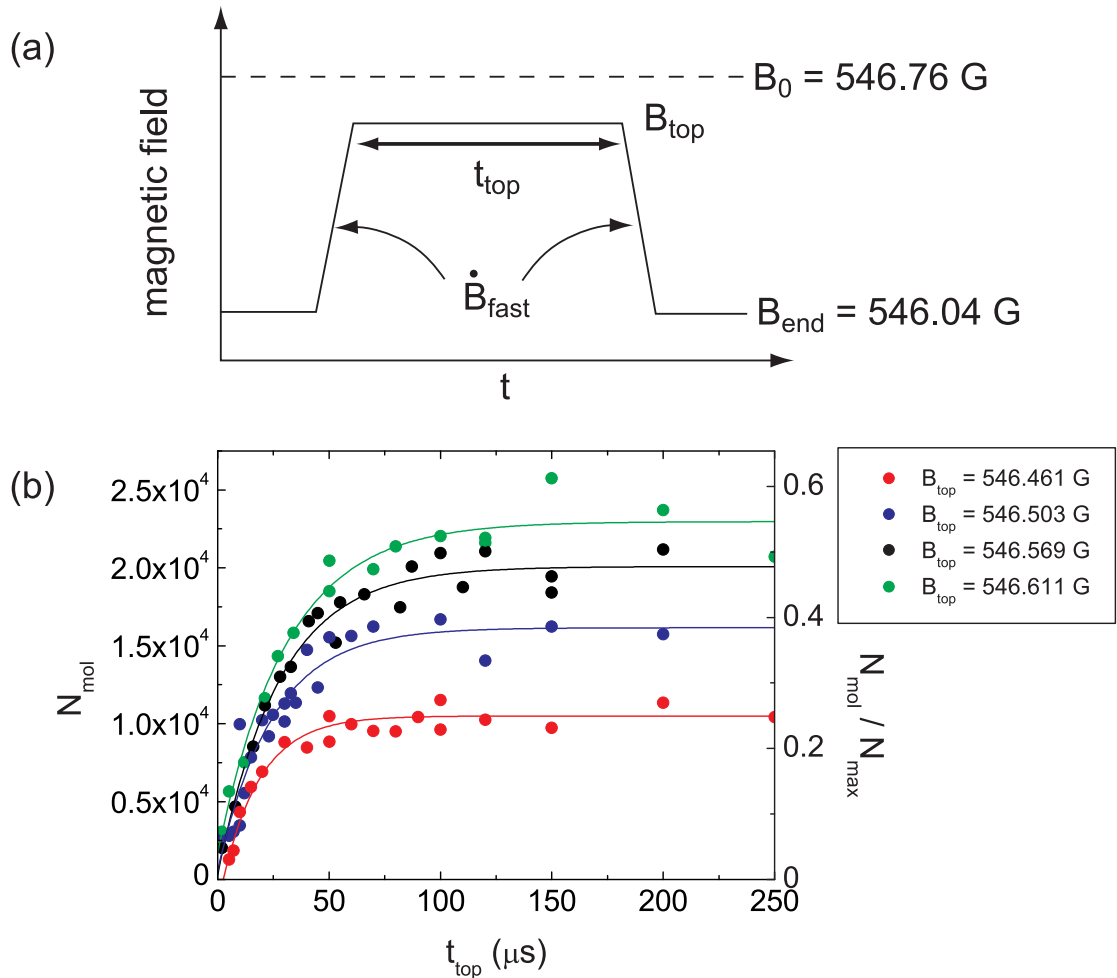


Figure 5.9: Time dependence of the molecule number in a single-pulse experiment. (a) A schematic of the magnetic pulse sequence. The ramp speed, \dot{B}_{fast} is 140 G/ms. (b) The measured molecule number is shown as a function of the hold time t_{top} for several different values of B_{top} . No oscillations in the molecule number are visible. The lines are fits to $N_{\text{mol}} = Ae^{-t/\tau} + y_0$. The green data correspond to the height of the two pulses in a typical double-pulse sequence in which Ramsey-type oscillations are observed.

5.4.2 Rabi oscillations in expansion

While we are unable to observe Rabi oscillations in the trapped mixture, we are able to observe oscillations in single-pulse experiments at the lower densities enabled by expansion of the gas. A schematic of a single pulse is shown Fig. 5.9a. After 1 ms of expansion from the trap, the magnetic field is ramped from 545.80 G to B_{top} , held for a time t_{top} , and ramped back down, with both ramps having speeds of 140 G/ms. The molecule population after a single pulse to $B_{\text{top}} = 546.51$ G as a function of the hold time t_{top} is shown in Fig. 5.10. Defining the contrast as the $t_{\text{top}} = 0$ amplitude $|A|$ divided by the final level of the damped oscillation y_0 , we measure a contrast of 0.5 ± 0.2 .

Since we can observe Rabi oscillations at some densities but not others, the visibility of Rabi oscillations must depend sensitively on the density of the gas. Figure 5.11 shows the molecule population as a function of hold time for gases with several different densities. The gases are prepared identically in the trap, and the different densities are achieved by varying the expansion time from the trap. If the density is too high, we recover the behavior of Fig. 5.9, but for the lower densities, we observe oscillation contrasts comparable to that in Fig. 5.10. Once the peak densities drop to $\leq 10^{12} \text{ cm}^{-3}$, we observe little change in the oscillation visibility when the density is further reduced. Presumably, at these densities, the magnetic-field ramps are sufficiently diabatic to have little impact on the oscillation amplitude. We estimate that the magnetic-field ramp speeds are >100 times faster than the $1/e$ ramp speed for adiabaticity. Also, the collision rates are becoming negligible ($\Gamma_{\text{KRb}} < 3\text{kHz}$).

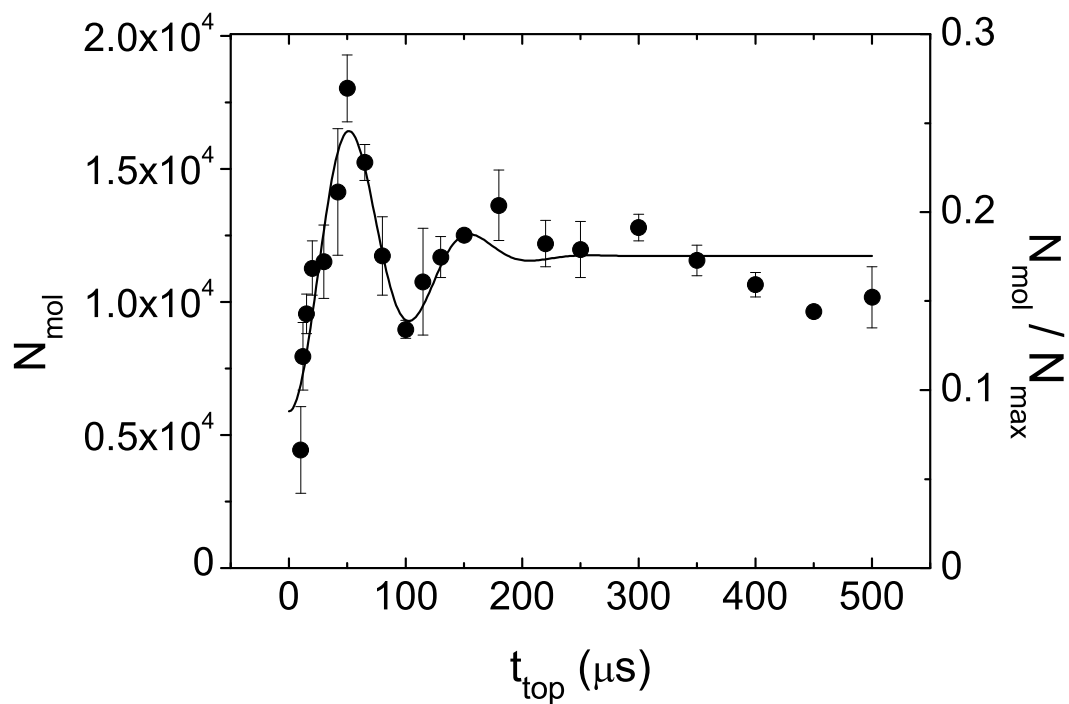


Figure 5.10: Rabi-type atom-molecule oscillations. The measured molecule number is shown as a function of the hold time t_{top} for a single pulse where B_{top} was 546.51 G. The line is a fit to $N_{\text{mol}} = Ae^{-t^2/(2\sigma^2)} \cos(2\pi\nu_{\text{osc}}t) + y_0$, yielding a frequency $\nu_{\text{osc}} = (9.3 \pm 0.5)$ kHz and rms damping time $\sigma = (80 \pm 20)$ μs .

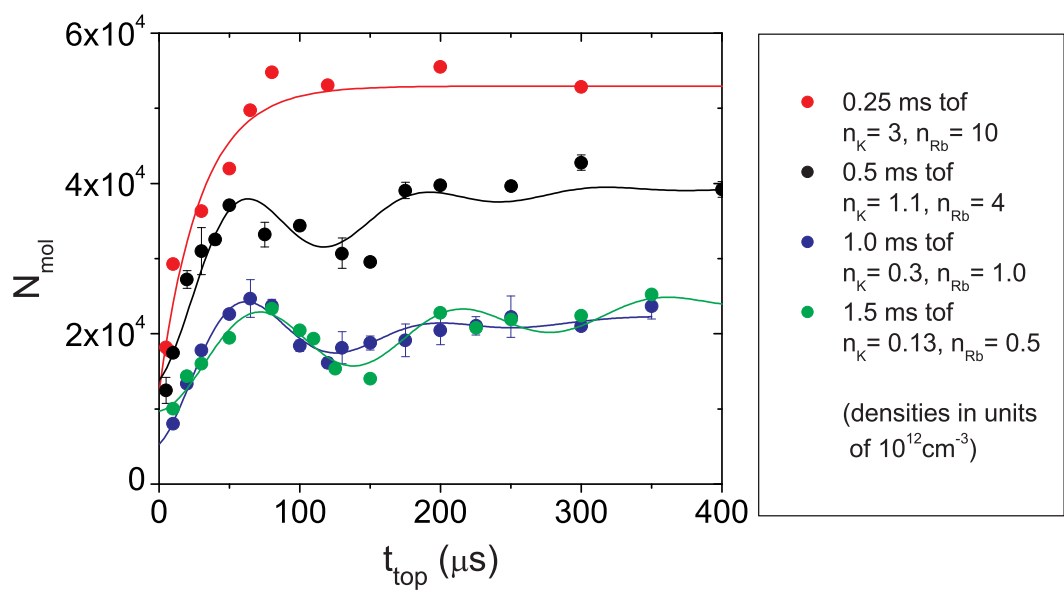


Figure 5.11: Rabi-type atom-molecule oscillations with varying density clouds. The measured molecule number is plotted as a function of the hold time at $B_{\text{top}} = 546.56\text{G}$ for single magnetic-field pulses applied after varying expansion times from the trap, or times-of-flight (tof). The lines, which are fits to $N_{\text{mol}} = A e^{-t/\tau_1} \sin(2\pi\nu_{\text{osc}}t - \phi) + B \cdot (1 - e^{-t/\tau_2}) + y_0$, are included only as a guide to the eye.

5.4.3 Amplitude dependence on B

The peak-to-peak amplitude of the oscillations in the molecule population depends on the value of B_{top} as shown in Fig. 5.12a. As B_{top} is increased, we observe fewer oscillations before they damp out, and for the data above $B_{\text{top}} = 546.6$ G, only one period of the oscillation is observed. Therefore, we define the peak-to-peak amplitude as the difference in molecule number between the first maximum and the subsequent minimum. We find that the amplitude of the oscillations is peaked near the Fano-Feshbach resonance where we observe a peak-to-peak amplitude that is 23% of N_{max} . We observe Rabi-type oscillations for values of B_{top} as far as 290 mG from the resonance. At $B_{\text{top}} = 546.47$ G, the oscillation amplitude drops to 6% of N_{max} . Here, the calculated molecule size is 1 100 a_0 , which is 5% of the typical distance between nearest-neighbor K and Rb atoms of 23 700 a_0 .

5.4.4 Frequency dependence on B

The frequency of the Rabi-type oscillations also depends on B_{top} as shown in Fig. 5.12b. Below the resonance, the measured frequency agrees with the prediction for the molecule binding energy, while above the resonance, where we only observe one period of the oscillation, the frequency saturates. This saturation may be expected in a many-level system [120, 118]. Figure 5.13 shows a schematic of the energy levels of two atoms confined in a harmonic trap. Above resonance, the molecule state adiabatically evolves into the ground state of the trap, and the energy difference between the trap states approaches a constant value. If, for example, a diabatic magnetic-field ramp to a value of B_{top} above the resonance creates a superposition of pairs in the ground state and the first excited state, we would expect the observed oscillation frequency to approach the trap level

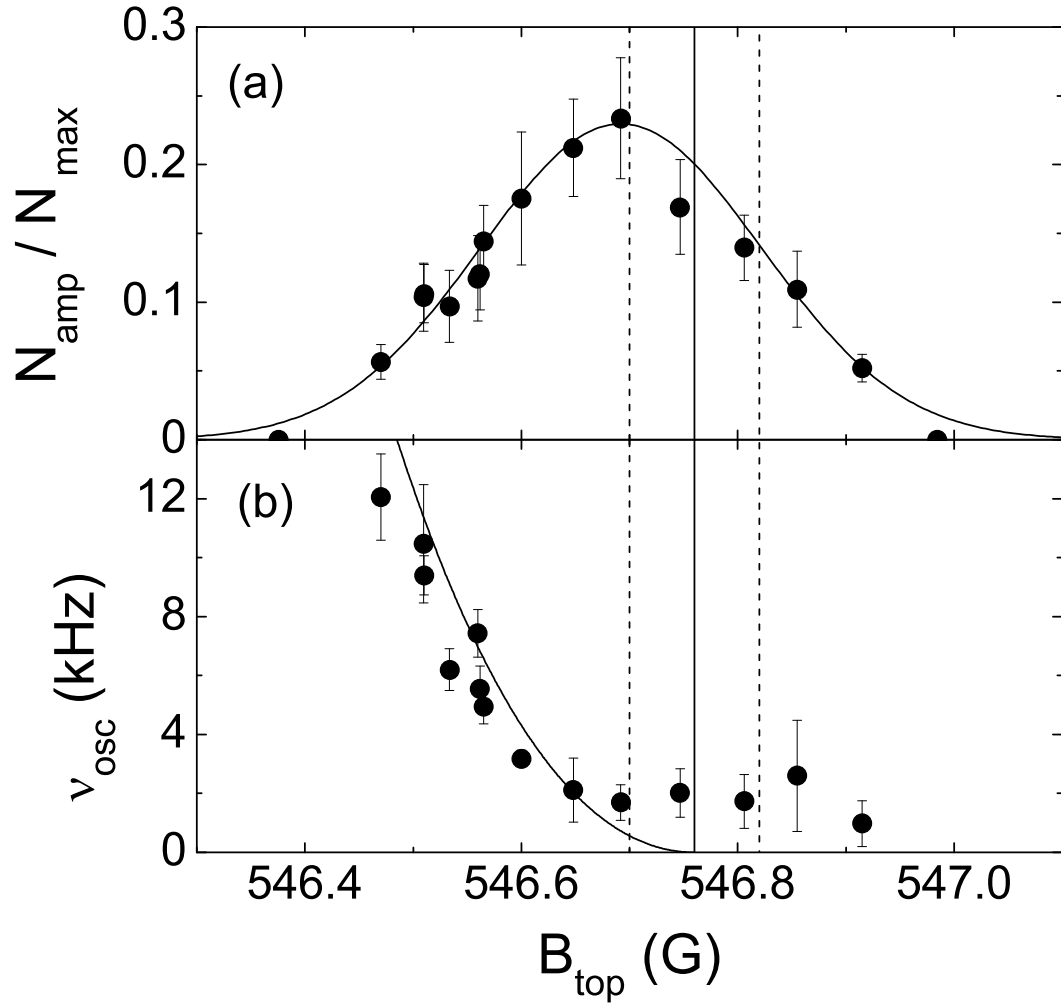


Figure 5.12: Magnetic-field dependence of the (a) peak-to-peak amplitude and (b) frequency of the single-pulse oscillations. The solid line in (a) is a Gaussian fit to the data, while the solid line in (b) is the molecule binding energy curve from Fig. 5.6. The vertical lines represent the fitted Fano-Feshbach resonance position and uncertainty from Fig. 5.6.

splitting divided by \hbar . This two-atom picture can be applied to a many-body system through a rescaling of the two-atom oscillator frequency to match the density of the ensemble [120, 118]. The effective oscillator frequency is given by [120]

$$\omega' = \frac{\hbar}{2\mu_{\text{KRb}}} \pi (\langle n_{\text{K}} \rangle \langle n_{\text{Rb}} \rangle)^{1/3}, \quad (5.9)$$

where $\langle n_i \rangle = \frac{1}{N_i} \int n_i^2(r) d^3r$ is the average number density of species i .⁴ We note that the observed saturation frequency of (1.7 ± 0.8) kHz agrees with the expected many-body level spacing of $2\omega'/\hbar = 1.2$ kHz.

The results of the single-pulse experiments can be used to infer the best pulses for double-pulse experiments. Maximum contrast should be achieved by using pulses where the hold time at B_{top} gives one quarter cycle of the single-pulse oscillation, which is analogous to a $\pi/2$ pulse in Ramsey's experiments [49]. In fact, we find that the empirically optimized pulse sequence for the expanded clouds corresponds to this condition.

5.5 Oscillation decoherence/dephasing

For both the single-pulse and double-pulse experiments, we observe damping of the atom-molecule oscillations within a few hundred microseconds (see Fig. 5.5, 5.10, and 5.11). There are many mechanisms for this loss of visibility of the fringes. Some are intrinsic to the atomic gas, while others are technical. The coherence times we observe appear to be limited by a combination of these mechanisms.

5.5.1 Non-technical mechanisms

Molecule lifetime

⁴ In Eq. 5.9, we have generalized to two species by replacing $\langle n \rangle^2/2$ with $\langle n_{\text{K}} \rangle \langle n_{\text{Rb}} \rangle$. This substitution follows from the fact that the number of possible pairs in a single species is $N(N - 1)/2 \approx N^2/2$, while the number of possible pairs in the mixture is $N_{\text{K}} N_{\text{Rb}}$ [109].

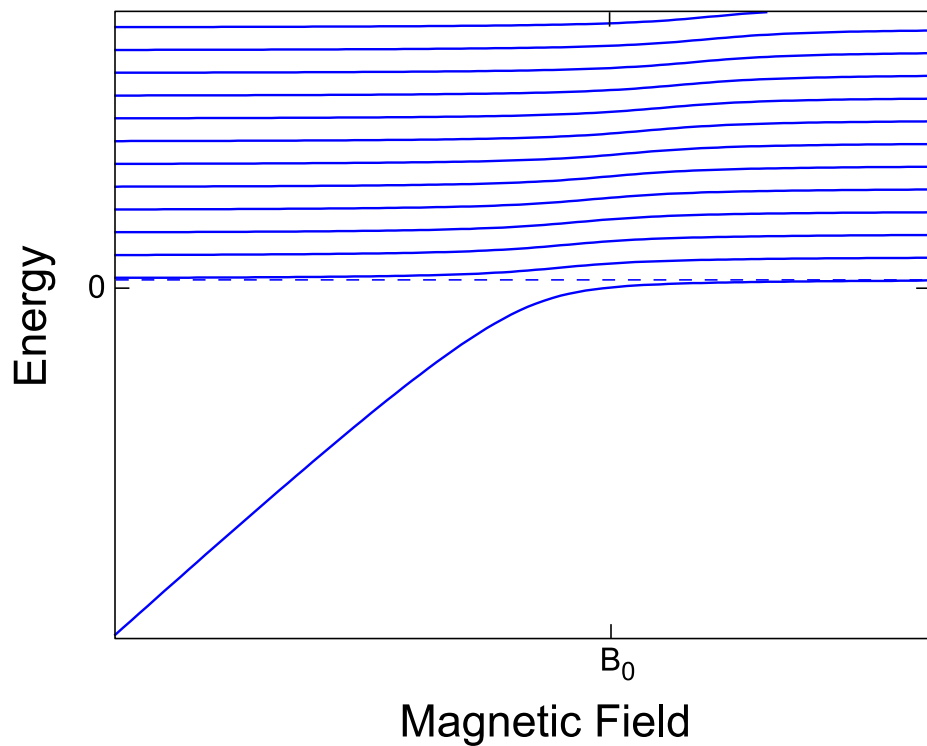


Figure 5.13: Schematic of the energy eigenvalues of a trapped atom pair in the vicinity of a Fano-Feshbach resonance. The solid lines represent the dressed trap states, while the dashed line shows the bare ground state of the trap.

There are many reasons why an oscillation in an ensemble of atoms might damp. Possibly the simplest cause of damping is loss of molecules—if the number of molecules decays with time, the amplitude of the oscillation will decay as well. The lifetime of Feshbach molecules depends on the density of the sample, the internal states and quantum statistics of the constituent atoms, and the proximity to the resonance [121, 122, 123, 124, 125, 126, 106]. For our mixture, we expect molecule lifetimes longer than a millisecond over the range of densities and fields probed [106] and have measured lifetimes as long as 10 ms. If the molecule lifetime were the cause of the damping, as in the experiments of Syassen *et al.* [45], the time-averaged number of molecules would decay. Instead, we observe damping in which the mean molecule number is constant. This type of damping is *not* due to a loss of molecules but is likely due to dephasing.

Energy distributions

Because we begin with an incoherent ensemble of atoms, the oscillations are expected to damp due to the differing relative kinetic energies of the atom pairs. Let us consider a simple illustration of this damping mechanism. Let us assume we have an ensemble of 10 atoms, each of which can pair with one and only one other atom, and each pair has a different relative kinetic energy. The probability of finding a given atom pair in the molecule state P_{pair} after either the single- or double-pulse sequence oscillates with a frequency determined by the energy difference between the atom and molecule states. A distribution of energies implies a distribution of frequencies. If we were able to monitor the oscillation frequency of each pair, we might observe oscillations such as those shown in Fig. 5.14. All the pairs begin oscillating in phase, but get out of sync, or dephase, due to their differing frequencies. Now, let us, instead, measure the total population in the molecule state as a function of time. The probability of finding the entire

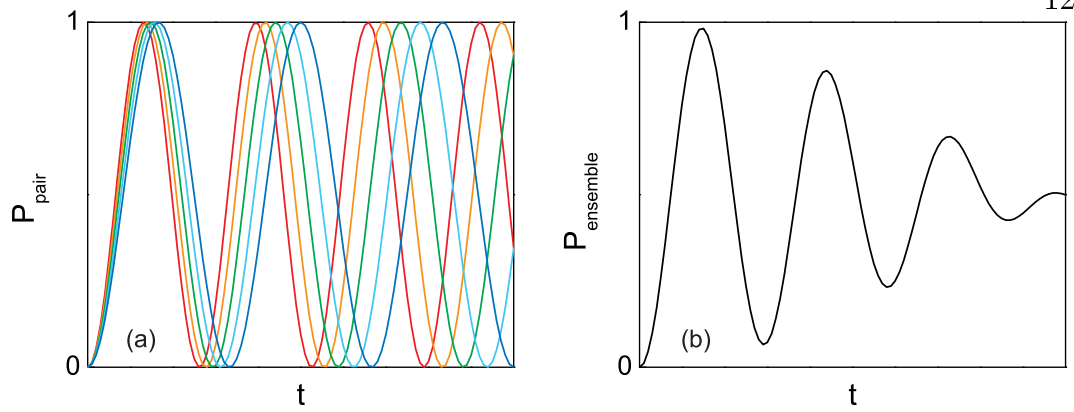


Figure 5.14: Illustration of dephasing. (a) The probability of finding an atom pair in the molecule state, P_{pair} , is shown as a function of time for five ideal pairs with 100% contrast and infinite coherence times but different frequencies. (b) The probability of finding all of the pairs in the molecule state, P_{ensemble} , is plotted as a function of time.

population in the molecule state is given by

$$P_{\text{ensemble}} = \frac{1}{N_{\text{pairs}}} \sum P_{\text{pair}}, \quad (5.10)$$

where $N_{\text{pairs}} = 5$ is the number of atom pairs. The total probability, P_{ensemble} , damps even if the coherence of the individual pairs persists, as shown in Fig. 5.14b.⁵

In the experiment, we measure the number of molecules as a function of time and are only sensitive to the total number in the molecule state. In the absence of other decoherence or dephasing mechanisms, the envelope of the oscillation in the total population is determined by the distribution of frequencies of the oscillating pairs. These oscillations in the molecule population may provide a probe of the initial relative kinetic energy distributions of the atom pairs.

Using the Monte Carlo simulations discussed in Chapter 4, we can calculate expected coherence times based on either of two assumptions about the distribu-

⁵ In the illustration, because there are only 5 atom pairs, the total probability would experience revivals of the oscillation. In the experiment, there is a near-continuum of relative kinetic energies, so we expect no such revivals.

tion of the relative kinetic energies of the oscillating pairs: (1) the distribution is the same as that of the pairs converted to molecules via adiabatic sweeps or (2) the distribution is the same as that of nearest-neighbor pairs. For trapped mixtures, the second assumption implies that the distribution reflects the temperature of the gas, and for expanded clouds, it reflects the local temperature distribution. Figure 5.15 shows expected oscillations for the typical in-trap conditions. Both the estimate based on the energy of the molecules and that of nearest neighbors predict coherence times longer than those observed experimentally (compare to Fig. 5.5b), but the nearest-neighbor calculation predicts a coherence time only a factor of 2 longer. Figure 5.16 shows similar calculations for the typical expansion conditions. Once again, we find that the coherence time estimated from the energy distribution of the molecules is much longer than our observations, while the nearest-neighbor energy distribution yields a result much closer to the experimental results (compare to Fig. 5.10). This may indicate that the requirements for creating pairs in a superposition are different or more stringent than for associating molecules with an adiabatic magnetic-field sweep. We might suspect that for the diabatic pulse to pair atoms, the interparticle separation must be similar to that of the molecule. This would introduce a real-space criterion in addition to (or instead of) the phase-space criterion, Eq. 4.1. However, there are additional decoherence mechanisms that are likely limiting the coherence times of both the Rabi- and Ramsey-type oscillations we have observed in the experiment. Dephasing due to the relative kinetic energy of the pairs is independent of magnetic field. As we shall see below (§5.5.2), the coherence times measured in the experiment do depend on magnetic-field, indicating that we are not yet probing the relative kinetic energy distribution of the pairs.

Atom dynamics

Another factor that can affect the coherence of atom-molecule oscillations is

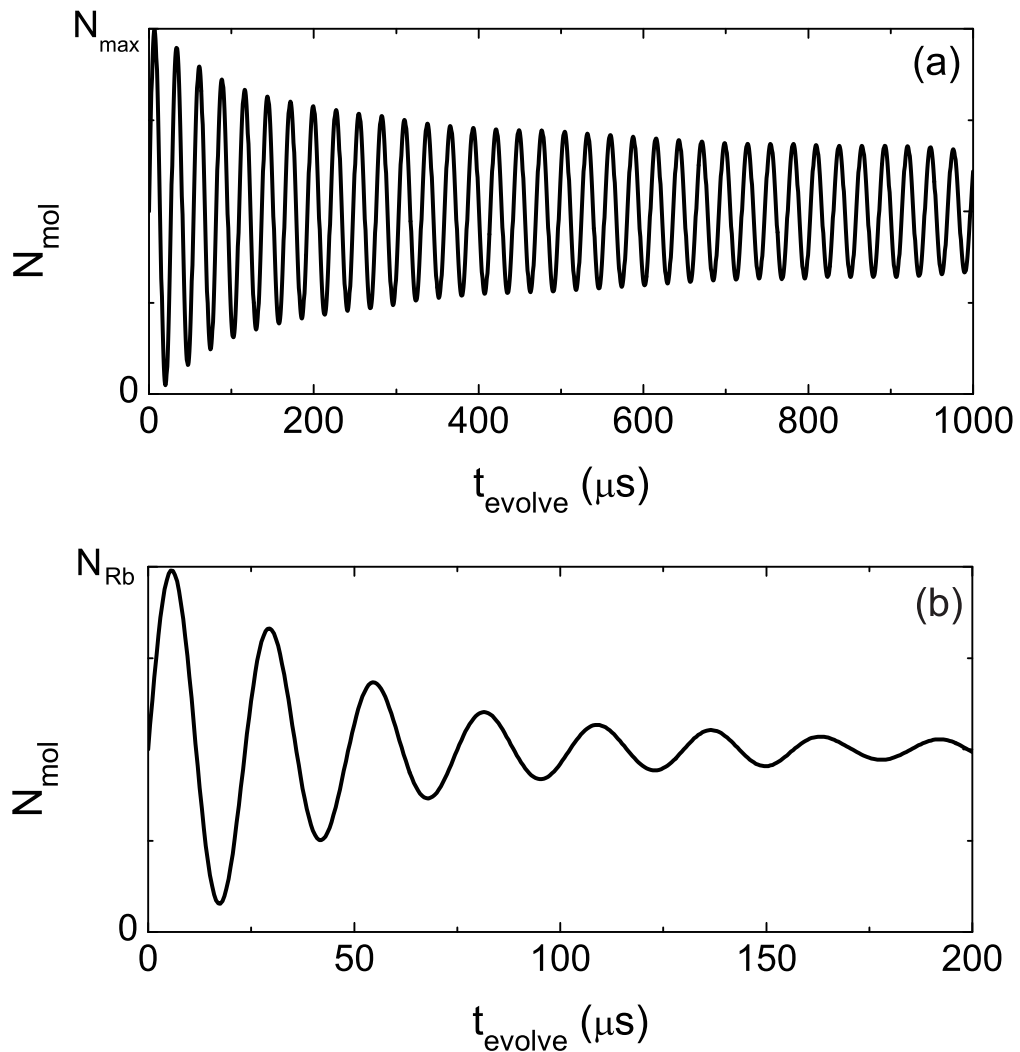


Figure 5.15: Calculated oscillations for typical in-trap conditions with coherence times limited by the energy distribution of the pairs. The calculation in (a) uses the relative kinetic energy distribution of molecules formed by adiabatic magnetic-field sweeps, while the calculation in (b) uses that of nearest-neighbor atom pairs.

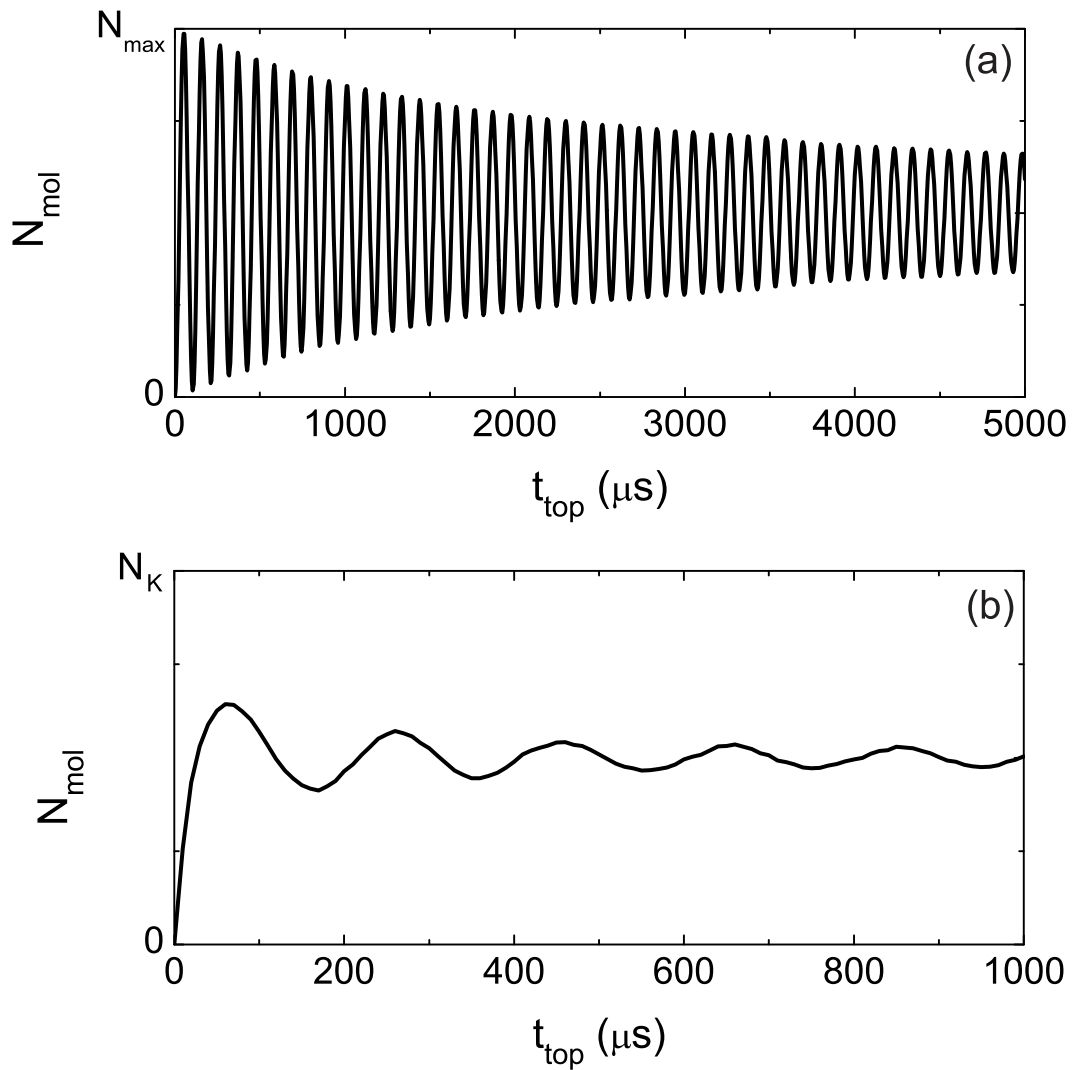


Figure 5.16: Calculated oscillations for typical expansion conditions with coherence times limited by the energy distribution of the pairs. The calculation in (a) uses the relative kinetic energy distribution of molecules formed by adiabatic magnetic-field sweeps, while the calculation in (b) uses that of nearest-neighbor atom pairs.

the motion of the atoms in the trap. Collisions between molecules and unbound atoms or other molecules are likely to break up the molecules, which in general, limit the molecule lifetime. However, the collision rate (Eq. 5.7) is negligible on the timescale of the observed oscillations. For the in-trap Ramsey oscillations (Figs. 5.5 and 5.6), the calculated collision rate is < 5 kHz. There may, however, be more subtle interactions that cause decoherence.

We expect the likelihood of coupling between two atoms to depend on their distance from one another. Because the atoms are not stationary in the trap, but are moving around, we might imagine partner-swapping events. Let us consider a K atom initially coupled to a Rb atom (Rb #1), with an uncoupled Rb atom (Rb #2) nearby. At some later time, it may be the case that Rb #2 is in closer proximity to the K atom than Rb #1, which may result in the K atom coupling instead to Rb #1. The resulting superposition would likely have a different phase, contributing to the dephasing of the observed atom-molecule oscillations. For such partner swapping to affect on the coherence time of the observed oscillations, however, the timescale of the motion of the atoms must be short compared to the interrogation time. As an estimate of this timescale, we use the Monte Carlo simulation discussed in Chapter 4 to calculate the time it takes for nearest-neighbor atoms to separate by an additional distance d , which is the typical interparticle spacing (see Appendix B for a discussion of the interparticle spacing). Fig. 5.17 shows the results of these calculations for both the trapped and expanded gas experiments. For the typical in-trap conditions, the separation of nearly half of the pairs increases by d in only 20 μ s, while for the typical expansion conditions, it takes 40 μ s. In both cases, the timescale for motion is comparable to the observed coherence times (see Figs. 5.5 and 5.10). The motion of the particles may be contributing to the decoherence of our observed oscillations. This may also explain why the contrast of the observed Ramsey oscillations is less than 1 both

in trap and in expansion, where the pulses toward resonance are $15 \mu\text{s}$ and $50 \mu\text{s}$ long, respectively.

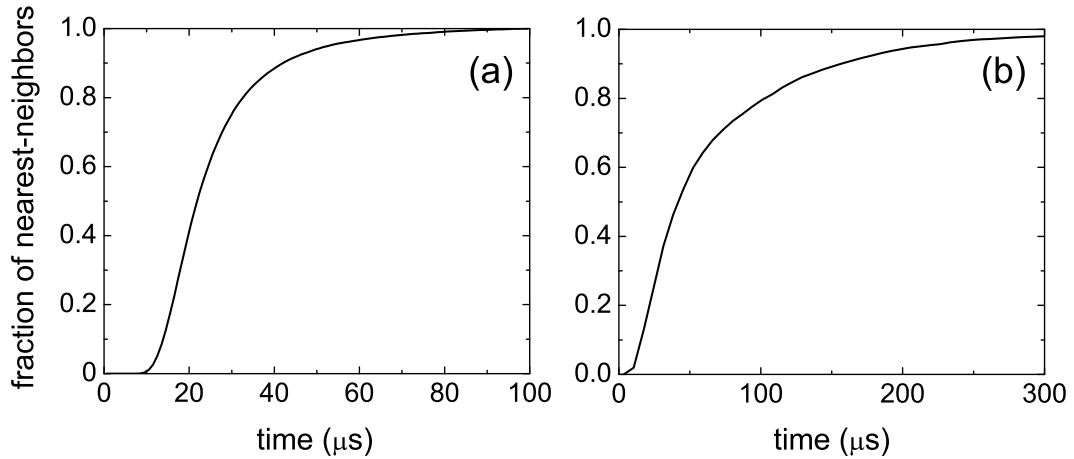


Figure 5.17: Atom motion in the trap and in expansion. Plotted is the calculated fraction of nearest neighbors that have separated by an additional distance equal to the typical interparticle spacing for the typical in-trap conditions (a) and the typical expansion conditions (b).

5.5.2 Technical mechanisms

Magnetic field inhomogeneity

We believe the main technical decoherence mechanism in our experiment is spatial inhomogeneity in the applied magnetic field. A spatial variation in magnetic field would cause the molecule binding energy to vary across the cloud. Given the quadratic dependence of the molecule binding energy on magnetic field near resonance (Eq. 5.8), this results in more rapid dephasing for larger magnetic-field detuning from the Fano-Feshbach resonance. Figure 5.18 shows the measured coherence time of Ramsey oscillations as a function of magnetic field. The measured coherence times of oscillations with $B_{\text{evolve}} < 546.1 \text{ G}$ are consistent with a 60 mG magnetic-field variation along the axial direction. If this magnetic-field inhomogeneity were the only mechanism for decoherence we would expect the coherence

time at $B_{\text{evolve}} = 546.3$ G to be $70 \mu\text{s}$. Instead, we measure $18 \mu\text{s}$, indicating that another decoherence mechanism dominates closer to the Fano-Feshbach resonance. The magnetic-field dependence for $B_{\text{evolve}} > 546.1$ G suggests that this additional mechanism may be collisional, though the observed coherence times are a factor of 14 shorter than the collision times $1/\Gamma$ we calculate with Eq. 5.7.

By improving the magnetic-field curvature cancellation discussed in §2.5, we should be able to improve the homogeneity of the magnetic field. This will allow for the investigation of the intrinsic dephasing due to the relative kinetic energies of the atom pairs.

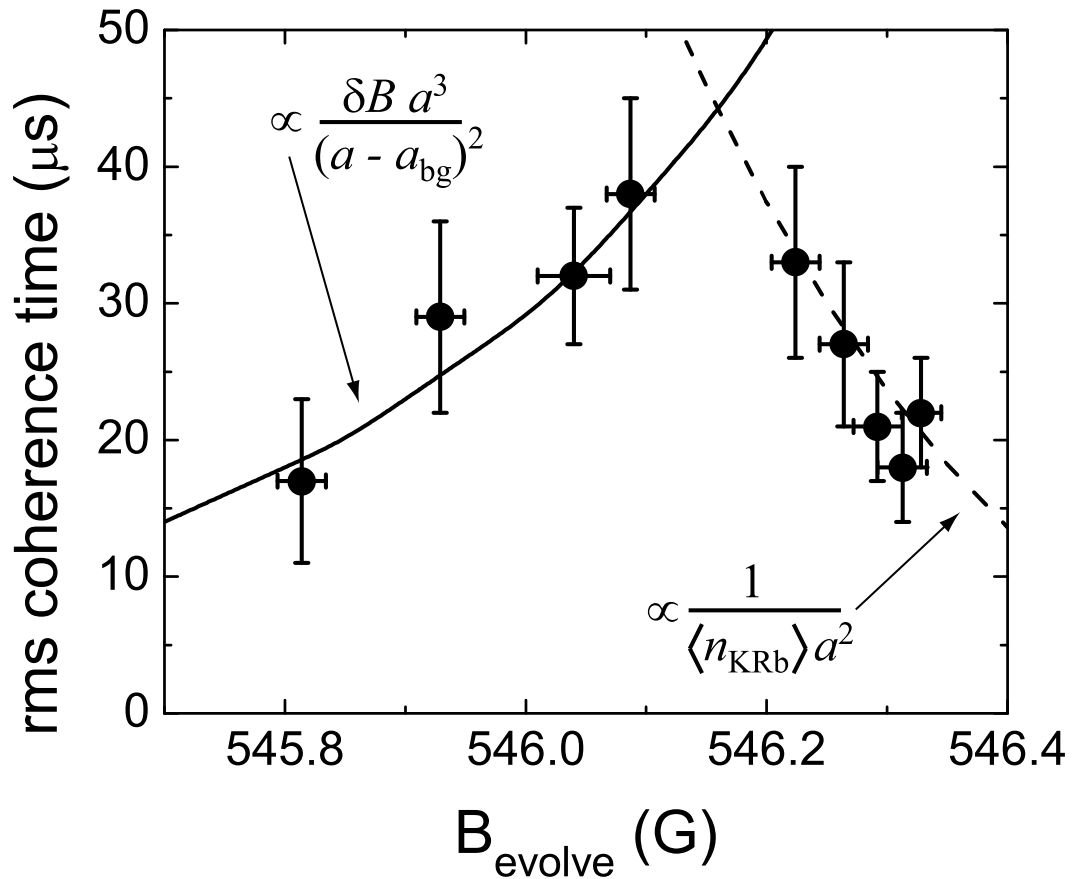


Figure 5.18: Magnetic-field dependence of the coherence times of Ramsey oscillations. The rms damping time is plotted as a function of B_{evolve} for Ramsey oscillations induced in trapped clouds under typical in-trap conditions. The solid line shows the calculated damping time for a linear magnetic-field gradient of 0.5 G/cm in the axial direction, which corresponds to a magnetic-field variation of $\delta B = 60$ mG across the atom/molecule clouds. The dashed line is $1/\Gamma_{\text{KRb}}$ calculated for $\langle n_{\text{KRb}} \rangle = 5 \times 10^{12} \text{ cm}^{-3}$ and scaled by a factor of 14 to match the data.

Chapter 6

As yet unsubstantiated Monte Carlo predictions

The Monte Carlo simulations discussed in Chapter 4 have proven to be a powerful tool in predicting the number of molecules that can be created via adiabatic magnetic-field sweeps through Fano-Feshbach resonances [61, 63], oscillating magnetic fields near a resonance [62], and rf association [64]. However, our direct measurements of the number of molecules created by adiabatic magnetic-field sweeps in the Bose-Fermi mixture always yield conversion fractions that are lower than we predict with the Monte Carlo simulations. We believe this to be due to enhanced losses incurred while crossing the resonance, and efforts are currently underway to understand and minimize these losses. If we can eliminate such losses, we may be able to use these simulations to predict more than just the number of molecules. Because the formation of molecules in the calculation depends on the relative momentum of the constituent atoms, we can also make predictions about the distributions of the relative kinetic energies of the paired atoms. To date, the ability of the Monte Carlo simulations to accurately predict the molecules' momenta (and, consequently energy) has not been experimentally tested. The atom-molecule oscillations we observe (see Chapter 5) may be able to probe the energies of the pairs and offer a method to test this aspect of the simulations.

In the absence of technical or collisional decoherence mechanisms, the coherence time of atom-molecule oscillations should be determined by the relative

kinetic energy distribution of the pairs. By using the Monte Carlo simulation to predict these energies, we can, therefore, make predictions about the coherence time and the shape of the observed oscillations. In this chapter, I discuss how these quantities depend on the temperature and quantum degeneracy of the initial atom gas.

6.1 Assumptions

In applying the results of the Monte Carlo simulations to atom-molecule oscillations, we are making several assumptions. The first assumption is that the frequency at which an atom pair oscillates is determined by the energy difference between the atom pair and molecule state as $\nu_{\text{osc}} = (E_b + E_{\text{rel}})/\hbar$. Here, E_b is the molecule binding energy and the relative kinetic energy is $E_{\text{rel}} = p_{\text{rel}}^2/(2\mu)$, where μ is the reduced mass and p_{rel} is the magnitude of the relative momentum of the atom pair. We are also assuming that the dephasing of the atom pairs is the dominant mechanism for decoherence. That is, the oscillation in the total population is given by

$$N_{\text{tot}}(t) = \frac{1}{2} \left(\int_0^\infty \cos(2\pi\nu_{\text{osc}}t) f(\nu_{\text{osc}}) d\nu_{\text{osc}} + 1 \right), \quad (6.1)$$

where $f(\nu_{\text{osc}})$ is the probability distribution of oscillation frequencies of the atom pairs. Therefore, by calculating the probability distribution of relative kinetic energies, we can determine the expected shape of the oscillation and vice versa.

We also make the assumption that the distribution of E_{rel} for pairs coupled by diabatic magnetic-field pulses is identical to either the distribution of E_{rel} either for pairs associated by adiabatic magnetic-field sweeps (pairs satisfying the phase-space criterion, Eq. 4.1) or for nearest-neighbor pairs. Neither of these is likely to be strictly true in the experiment, but as we shall see below, we may be able to use the temperature dependence of the oscillation coherence times to

determine which, if either, of these distributions best reflects the pairs coupled by the magnetic-field pulses.

6.2 Dependence of coherence times on temperature

In this section, we consider the effect of temperature on the coherence times of the oscillations. As we have seen in Chapter 4, the number of molecules formed via adiabatic magnetic-field sweeps through a Fano-Feshbach resonance is expected to depend only on the quantum degeneracy of the mixture, and not on the absolute temperature. However, for the same quantum degeneracy, a mixture at a higher temperature will have a wider distribution of E_{rel} . This could result in more rapid dephasing of atom-molecule oscillations. Figure 6.1a shows calculated atom-molecule oscillations for mixtures at a variety of temperatures. In each of these simulations, the number of atoms are $N_K = 15,000$ and $N_{\text{Rb}} = 5,000$, and the temperature T of the mixture is equal to T_C and $0.27 T_F$. As we might expect, the calculated coherence time, shown in Fig. 6.1b, is inversely proportional to the temperature of the mixture. Therefore, to observe long-lived atom-molecule oscillations in the experiment, we want to work with clouds with low absolute temperatures.

The above calculations assumed the energy distribution of the oscillating pairs to be the same as the energy distribution of molecules associated by adiabatic sweeps. If, instead, we assume that the oscillating pairs are described by the energy distribution of nearest-neighbors, we find a different shape for the oscillations and shorter coherence times. The $1/e$ coherence time for $T = T_C = 36\text{nK}$ is $220 \mu\text{s}$ for the nearest-neighbor calculation, in contrast to $3300 \mu\text{s}$ for the molecule calculation (see Appendix A for a discussion). However, we still find that for clouds with the same quantum degeneracy, the expected coherence time is inversely proportional to the temperature.

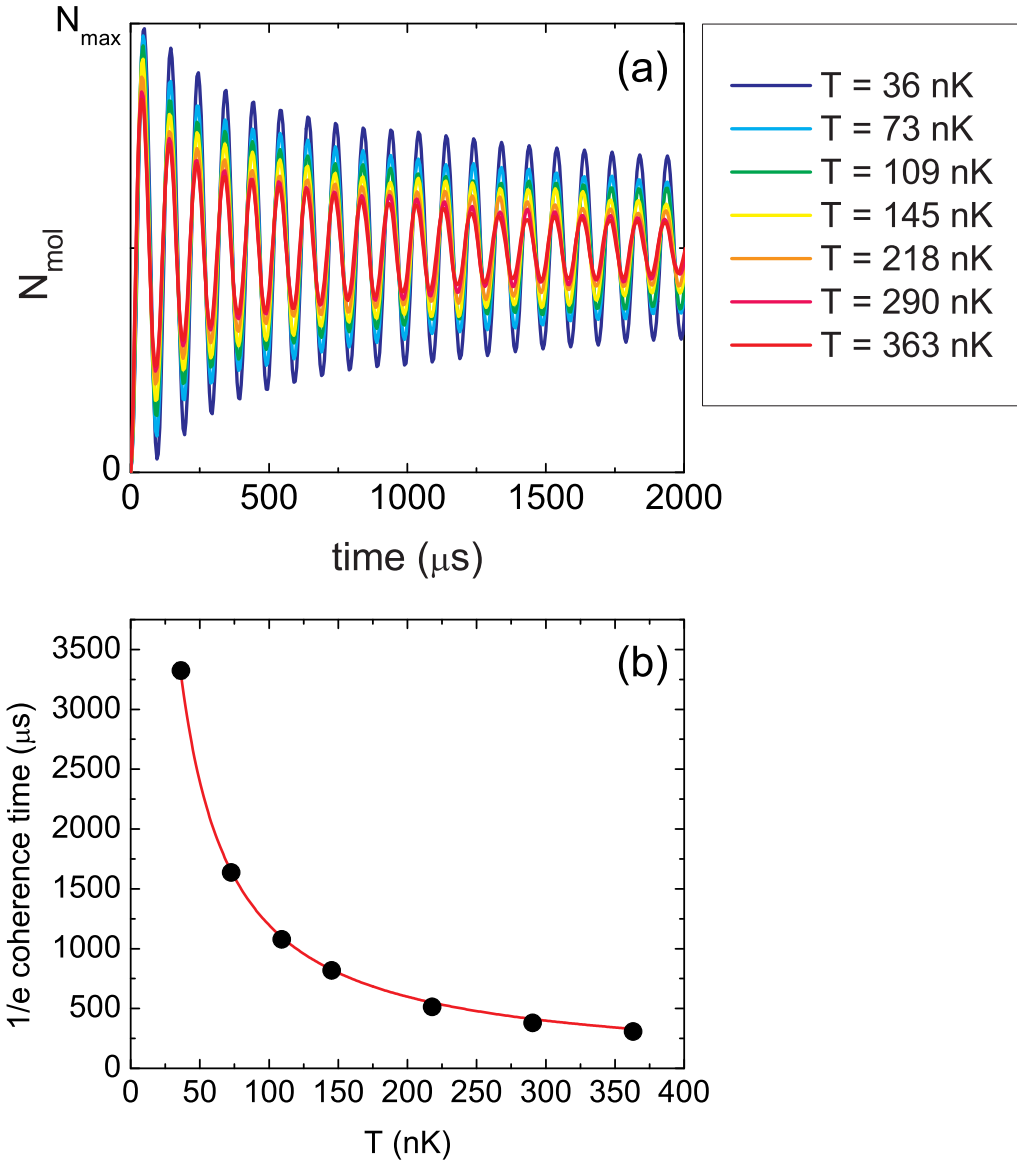


Figure 6.1: Expected temperature dependence of the coherence time of atom-molecule oscillations. (a) Calculated atom-molecule oscillations for atom clouds with $N_K = 15,000$ and $N_{\text{Rb}} = 5,000$ at a temperature $T = T_C$. For each curve, we run the Monte Carlo simulation for molecule creation to obtain the distribution of relative kinetic energies of the molecules, and the number of molecules as a function of time is calculated with Eq. 6.1 with a molecule binding energy $E_b = h \times 10 \text{ kHz}$. While these oscillations do not fit to exponentially decaying envelopes, as an estimate of the coherence time for each, we calculate the time at which the amplitude drops by $1/e$. The calculated $1/e$ coherence times, τ , are plotted as a function of temperature in (b). The line is a fit to $\tau = A/T$, yielding $A = (1.197 \pm 0.008) \text{ ms} \cdot \text{nK}$.

6.3 Dependence of coherence times on quantum degeneracy

In comparing the calculated energy distributions of nearest-neighbors and of molecules, we see that the phase-space criterion for molecule formation (Eq. 4.1) preferentially selects out pairs with low relative kinetic energy. This leads to longer coherence times if the diabatically coupled pairs must also satisfy this criterion. Simply comparing the observed coherence times in the experiment (in the absence of other decoherence mechanisms) to these predictions should give a good indication of whether either of these energy distributions is reflected in the oscillating pairs. An additional method to determine if the diabatic magnetic-field pulses preferentially select low-energy pairs is to study the dependence of the coherence time of the quantum degeneracy of the mixture.

Figure 6.2a shows the calculated atom-molecule oscillations for clouds at varying T/T_C , with T_C fixed at 36 nK. Here, the envelope of the oscillation is determined by the distribution of energies of adiabatically-associated molecules. As the temperature of the cloud drops below T_C , we see that the oscillation envelope changes, and the coherence time *decreases* with decreasing temperature (see Fig. 6.2b), and above T_C , we observe little dependence on the temperature. This is in direct contradiction to the naive picture that a colder cloud ought to have a narrower distribution of energies. However, we can understand this by considering how atoms are paired in the Monte Carlo simulation. To form a molecule, atoms are required to have a small product of $\Delta r_{\text{rel}}\Delta p_{\text{rel}}$. Above T_C , the position and momentum distributions of the Bose and Fermi clouds are similar to one another. While the momentum distribution may be wide for both, it is possible to have many pairs with a large center-of-mass momentum but small relative momentum. In this case, the distribution of E_{rel} will have a large contribution at low energies, which will result in long coherence times. In the case of a zero temperature

mixture, all the Rb atoms are in a BEC. The relative momentum between a Rb atom and any K atom, then, is equal to the momentum of the K atom. Therefore, the distribution of relative energies is simply the energy distribution of a $T = 0$ Fermi gas. Due to the Pauli exclusion principle, there can be no pile-up at low energies. This wider distribution of relative energies results in shorter coherence times, despite the lower temperature.

If, instead, we assume that the pairs coupled by the diabatic pulses have an energy distribution similar to that of nearest-neighbors, we find that the coherence times of the atom-molecule oscillations follow the intuitive notion that colder clouds result in longer-lived oscillations. Figure 6.3 shows the results of calculations using the Monte Carlo simulation to identify nearest-neighbor pairs and calculate their relative kinetic energies. Here, we have no preferential selection of low-energy pairs since the distribution of E_{rel} of nearest neighbors is the same as the distribution of E_{rel} over the whole cloud. As the mixture gets colder, the distribution of E_{rel} becomes narrower, and the coherence time increases.

Discerning the functional form of the envelope of an oscillation to determine the energy distribution of the oscillating pairs can be difficult in real experiments where shot-to-shot noise may limit the visibility of the fringes. However, by observing whether the coherence time increases or decreases as a function of the quantum degeneracy of the mixture, we should be able to determine if the atom pairs coupled by the diabatic magnetic-field pulses are subject to the same phase-space criterion as molecules associated via magnetic-field sweeps, oscillating magnetic fields, and rf association.

By studying the coherence times of oscillations that are not limited by collisions or magnetic-field inhomogeneities, we should be able to probe the distributions of the relative kinetic energies of the pairs coupled by the pulses and perhaps gain insight into the coupling mechanism.

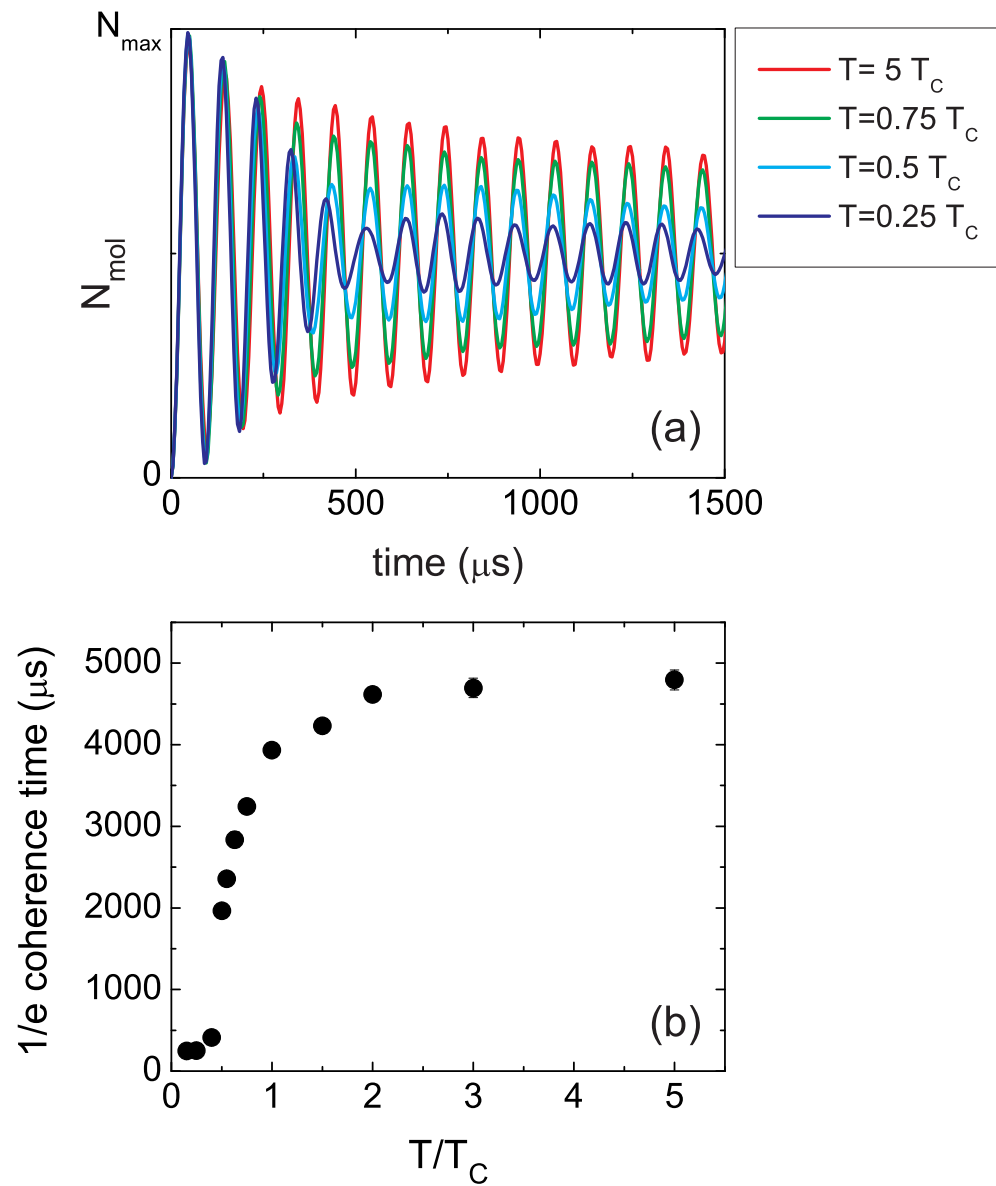


Figure 6.2: Expected dependence of the atom-molecule oscillation coherence time on quantum degeneracy. (a) Calculated atom-molecule oscillations for atom clouds with $N_K = 15,000$ and $N_{\text{Rb}} = 5,000$ and $T_C = 36 \text{ nK}$. For each curve, we run the Monte Carlo simulation for molecule creation to obtain the distribution of relative kinetic energies of the molecules, and the number of molecules as a function of time is calculated with Eq. 6.1 with a molecule binding energy $E_b = h \times 10 \text{ kHz}$. The calculated $1/e$ coherence times are plotted as a function of temperature in (b).

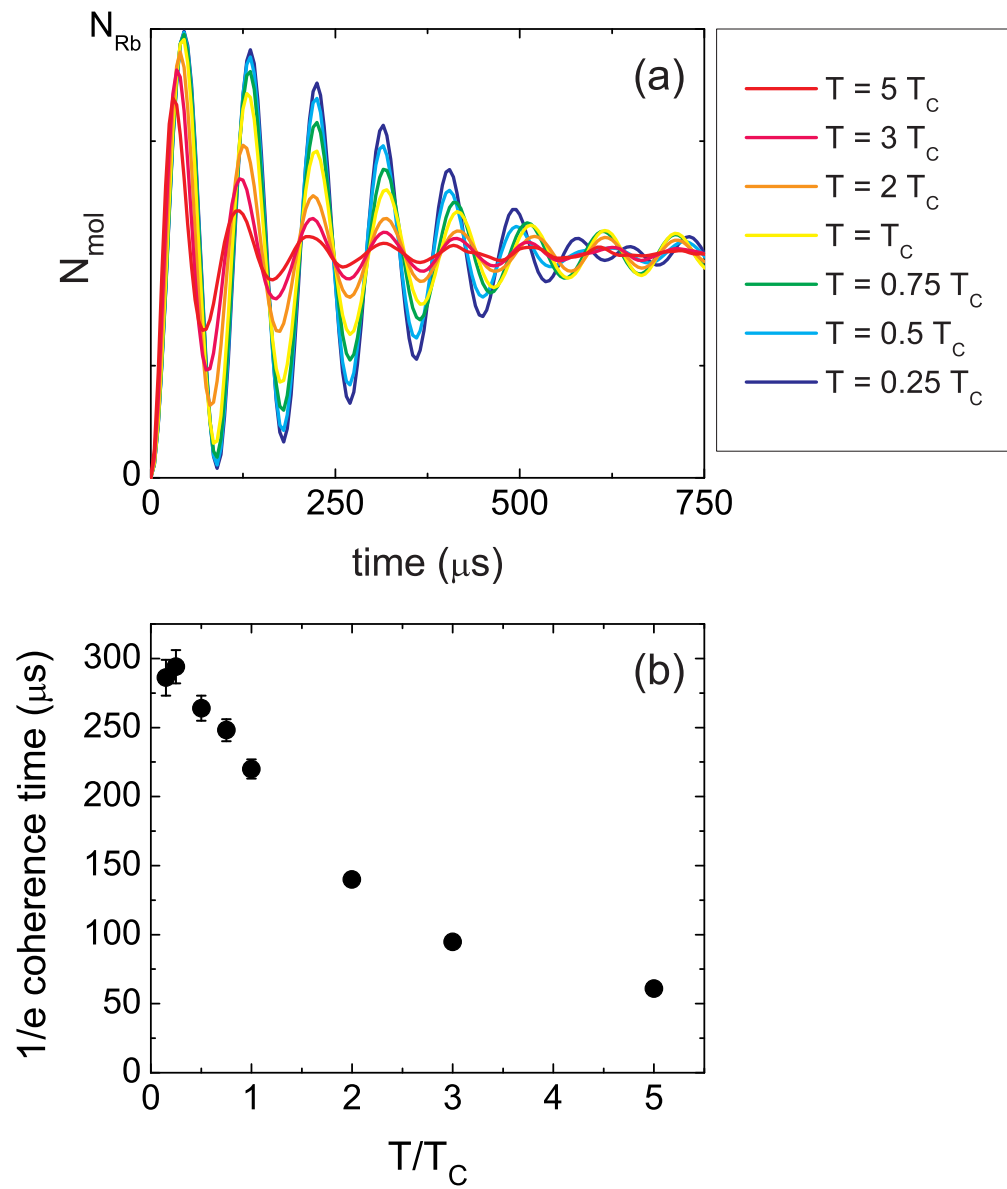


Figure 6.3: Expected dependence of the nearest-neighbor atom-molecule oscillation coherence time on quantum degeneracy. (a) Calculated atom-molecule oscillations for atom clouds with $N_K = 15,000$ and $N_{\text{Rb}} = 5,000$ and $T_C = 36 \text{ nK}$. For each curve, we run the Monte Carlo simulation to identify nearest neighbors and obtain their relative kinetic energies. The number of molecules as a function of time is calculated with Eq. 6.1 with a molecule binding energy $E_b = h \times 10 \text{ kHz}$. The calculated $1/e$ coherence times are plotted as a function of temperature in (b).

Chapter 7

Conclusions and Outlook

In this thesis, I have described the renovation of our Bose-Fermi mixture apparatus and the experiments creating ultracold fermionic molecules that followed. These experiments culminated in the creation of a quantum superposition of atoms and molecules, which involves three chemically distinct species with different quantum statistics: bosonic Rb atoms, fermionic K atoms, and fermionic KRb molecules. In this superposition, two atoms are both a pair of free atoms *and* a bound molecule at the same time! The superposition was not demonstrated in two or only a few atoms but in tens of thousands of atoms simultaneously. Additionally, these atoms were not prepared in a single energy state, but occupied a distribution of states. Despite this, coherent oscillations in the macroscopic atom population have been observed. These oscillations may prove to be a direct probe of the temperature and quantum degeneracy of the molecules.

Currently, efforts are under way to eliminate magnetic-field inhomogeneities, which are likely the dominant mechanism for the dephasing of the atom-molecule oscillations we have observed. In the absence of such technical causes for dephasing, the coherence times of the oscillations should be limited by the distribution of relative kinetic energies of the pairs participating in the superposition. This will allow for the testing of my predictions for the oscillations' dependences on temperature and degeneracy.

Similar oscillations have been predicted for quantum degenerate two-component Fermi systems [55, 56, 57]. As in our experiments, the initial atomic gas would not be prepared in a single energy state but would instead be described by a Fermi-Dirac energy distribution. A particularly interesting application would be to study coherent oscillations between the superfluid BCS state and a molecular BEC in the BCS-BEC crossover [55, 56].

For the longer term, I expect this experiment to move away from molecules and begin to study some of the more exotic phenomena predicted in Bose-Fermi mixtures. With so many options, it's difficult to predict which path will be chosen, but I think the observation of Boson-mediated Cooper pairing (with or without a lattice) would be a great achievement.

Bibliography

- [1] E. A. Cornell and C. E. Wieman, Nobel Lecture: Bose-Einstein condensation in a dilute gas, the first 70 years and some recent experiments, *Rev. Mod. Phys.* **74**, 875 (2002).
- [2] W. Ketterle, Nobel lecture: When atoms behave as waves: Bose-Einstein condensation and the atom laser, *Rev. Mod. Phys.* **74**, 1131 (2002).
- [3] N. Claussen, Dynamics of Bose-Einstein Condensates near a Feshbach resonance in ^{85}Rb , Ph.D. thesis, University of Colorado, Boulder, 2003.
- [4] T. Weber, J. Herbig, M. Mark, H.-C. Nagerl, and R. Grimm, Bose-Einstein condensation of Cesium, *Science* **299**, 232 (2003).
- [5] T. Volz, S. Dürr, S. Ernst, A. Marte, and G. Rempe, Characterization of elastic scattering near a Feshbach resonance in ^{87}Rb , *Phys. Rev. A* **68**, 010702 (2003).
- [6] C. A. Regal, M. Greiner, and D. S. Jin, Observation of resonance condensation of fermionic atom pairs, *Phys. Rev. Lett.* **92**, 040403 (2004).
- [7] M. W. Zwierlein, C. A. Stan, C. H. Schunck, S. M. F. Raupach, A. J. Kerman, and W. Ketterle, Condensation of pairs of fermionic atoms near a Feshbach resonance, *Phys. Rev. Lett.* **92**, 120403 (2004).
- [8] T. Köhler, K. Goral, and P. S. Julienne, Production of cold molecules via magnetically tunable Feshbach resonances, *Rev. Mod. Phys.* **78**, 1311 (2006).
- [9] G. Modugno, G. Roati, F. Riboli, F. Ferlaino, R. J. Brecha, and M. Inguscio, Collapse of a degenerate Fermi gas, *Science* **297**, 2240 (2002).
- [10] C. A. Stan, M. W. Zwierlein, C. H. Schunck, S. M. F. Raupach, and W. Ketterle, Observation of Feshbach resonances between two different atomic species, *Phys. Rev. Lett.* **93**, 143001 (2004).
- [11] S. Inouye, J. Goldwin, M. L. Olsen, C. Ticknor, J. L. Bohn, and D. S. Jin, Observation of heteronuclear Feshbach resonances in a mixture of bosons and fermions, *Phys. Rev. Lett.* **93**, 183201 (2004).

- [12] E. G. M. van Kempen, S. J. J. M. F. Kokkelmans, D. J. Heinzen, and B. J. Verhaar, Interisotope determination of ultracold rubidium interactions from three high-precision experiments, *Phys. Rev. Lett.* **88**, 093201 (2002).
- [13] A. Marte, T. Volz, J. Schuster, S. Durr, G. Rempe, E. G. M. van Kempen, and B. J. Verhaar, Feshbach resonances in Rubidium 87: Precision measurement and analysis, *Phys. Rev. Lett.* **89**, 283202 (2002).
- [14] R. Roth and H. Feldmeier, Mean-field instability of trapped dilute boson-fermion mixtures, *Phys. Rev. A* **65**, 021603 (2002).
- [15] C. Ospelkaus, S. Ospelkaus, K. Sengstock, and K. Bongs, Interaction-driven dynamics of ^{40}K - ^{87}Rb fermion-boson gas mixtures in the large-particle-number limit, *Phys. Rev. Lett.* **96**, 020401 (2006).
- [16] J. L. Roberts, N. R. Claussen, S. L. Cornish, E. A. Donley, E. A. Cornell, and C. E. Wieman, Controlled collapse of a Bose-Einstein condensate, *Phys. Rev. Lett.* **86**, 4211 (2001).
- [17] E. A. Donley, N. R. Claussen, S. L. Cornish, J. L. Roberts, E. A. Cornell, and C. E. Wieman, Dynamics of collapsing and exploding Bose-Einstein condensates, *Nature* **412**, 295 (2001).
- [18] L. Viverit, C. J. Pethick, and H. Smith, Zero-temperature phase diagram of binary boson-fermion mixtures, *Phys. Rev. A* **61**, 053605 (2000).
- [19] S. Ospelkaus, C. Ospelkaus, L. Humbert, K. Sengstock, and K. Bongs, Tuning of heteronuclear interactions in a degenerate Fermi-Bose mixture, *Phys. Rev. Lett.* **97**, 120403 (2006).
- [20] A. P. Albus, S. Giorgini, F. Illuminati, and L. Viverit, Critical temperature of Bose-Einstein condensation in trapped atomic Bose-Fermi mixtures, *J. Phys. B: At. Mol. Opt. Phys.* **35**, L511 (2002).
- [21] T. Karpiuk, M. Brewczyk, S. Ospelkaus-Schwarzer, K. Bongs, M. Gajda, and K. Rzążewski, Soliton trains in Bose-Fermi mixtures, *Phys. Rev. Lett.* **93**, 100401 (2004).
- [22] J. Santhanam, V. M. Kenkre, and V. V. Konotop, Solitons of Bose-Fermi mixtures in a strongly elongated trap, *Phys. Rev. A* **73**, 013612 (2006).
- [23] T. Karpiuk, M. Brewczyk, and K. Rzążewski, Bright solitons in Bose-Fermi mixtures, *Phys. Rev. A* **73**, 053602 (2006).
- [24] D. V. Efremov and L. Viverit, p -wave Cooper pairing of fermions in mixtures of dilute Fermi and Bose gases, *Phys. Rev. B* **65**, 134519 (2002).
- [25] F. Matera, Fermion pairing in Bose-Fermi mixtures, *Phys. Rev. A* **68**, 043624 (2003).

- [26] H. Heiselberg, C. J. Pethick, H. Smith, and L. Viverit, Influence of induced interactions on the superfluid transition in dilute Fermi gases, *Phys. Rev. Lett.* **85**, 2418 (2000).
- [27] M. J. Bijlsma, B. A. Heringa, and H. T. C. Stoof, Phonon exchange in dilute Fermi-Bose mixtures: Tailoring the Fermi-Fermi interaction, *Phys. Rev. A* **61**, 053601 (2000).
- [28] M. Lewenstein, L. Santos, M. A. Baranov, and H. Fehrmann, Atomic Bose-Fermi mixtures in an optical lattice, *Phys. Rev. Lett.* **92**, 050401 (2004).
- [29] H. P. Büchler and G. Blatter, Supersolid versus phase separation in atomic Bose-Fermi mixtures, *Phys. Rev. Lett.* **91**, 130404 (2003).
- [30] R. Roth and K. Burnett, Quantum phases of atomic boson-fermion mixtures in optical lattices, *Phys. Rev. A* **69**, 021601 (2004).
- [31] F. Illuminati and A. Albus, High-temperature atomic superfluidity in lattice Bose-Fermi mixtures, *Phys. Rev. Lett.* **93**, 090406 (2004).
- [32] D.-W. Wang, M. D. Lukin, and E. Demler, Engineering superfluidity in Bose-Fermi mixtures of ultracold atoms, *Phys. Rev. A* **72**, 051604 (2005).
- [33] F. Schmitt, M. Hild, and R. Roth, Bose-Fermi mixtures in 1D optical superlattices using full and truncated single-band bases, *J. Phys. B: At. Mol. Opt. Phys.* **40**, 371 (2007).
- [34] A. Sanpera, A. Kantian, L. Sanchez-Palencia, J. Zakrzewski, and M. Lewenstein, Atomic Fermi-Bose mixtures in inhomogeneous and random lattices: From Fermi glass to quantum spin glass and quantum percolation, *Phys. Rev. Lett.* **93**, 040401 (2004).
- [35] S. Ospelkaus, C. Ospelkaus, O. Wille, M. Succo, P. Ernst, K. Sengstock, and K. Bongs, Localization of bosonic atoms by fermionic impurities in a three-dimensional optical lattice, *Phys. Rev. Lett.* **96**, 180403 (2006).
- [36] T. Best, S. Will, U. Schneider, L. Hackermüller, D.-S. Lühmann, D. van Oosten, and I. Bloch, Role of interactions in ^{87}Rb - ^{40}K Bose-Fermi mixtures in a 3d optical lattice, *arXiv:0807.4504v1* (2008).
- [37] M. L. Olsen, J. D. Perreault, T. D. Cumby, and D. S. Jin, Coherent atom-molecule oscillations in a Bose-Fermi mixture, *arXiv:0810.1965* (2008).
- [38] K.-K. Ni, S. Ospelkaus, M. H. G. de Miranda, A. Pe'er, B. Neyenhuis, J. J. Zirbel, S. Kotochigova, P. S. Julienne, D. S. Jin, and J. Ye, A high phase-space-density gas of polar molecules, *Science* **322**, 231 (2008).
- [39] D. DeMille, Quantum computation with trapped polar molecules., *Phys. Rev. Lett.* **88**, 067901 (2008).

- [40] H. P. Buchler, E. Demler, M. Lukin, A. Micheli, N. Prokof'ev, G. Pupillo, and P. Zoller, Strongly correlated 2D quantum phases with cold polar molecules: Controlling the shape of the interaction potential, *Phys. Rev. Lett.* **98**, 060404 (2007).
- [41] G. Pupillo, A. Micheli, H. P. Buchler, and P. Zoller, Condensed matter physics with cold polar molecules, *arXiv:0805.1896v1* (2008).
- [42] F. Ferlaino, C. D'Errico, G. Roati, M. Zaccanti, M. Inguscio, G. Modugno, and A. Simoni, Feshbach spectroscopy of a K-Rb atomic mixture, *Phys. Rev. A* **73**, 040702 (2006).
- [43] S. Ospelkaus, A. Pe'er, K.-K. Ni, J. J. Zirbel, B. Neyenhuis, S. Kotochigova, P. S. Julienne, J. Ye, and D. S. Jin, Efficient state transfer in an ultracold dense gas of heteronuclear molecules, *Nat. Phys.* **4**, 622 (2008).
- [44] E. A. Donley, N. R. Claussen, S. T. Thompson, and C. E. Wieman, Atom-molecule coherence in a Bose-Einstein condensate, *Nature* **417**, 529 (2002).
- [45] N. Syassen, D. M. Bauer, M. Lettner, D. Dietze, T. Volz, S. Durr, and G. Rempe, Atom-molecule Rabi oscillations in a Mott insulator, *Phys. Rev. Lett.* **99**, 033201 (2007).
- [46] I. I. Rabi, J. R. Zacharias, S. Millman, and P. Kusch, A new method of measuring nuclear magnetic moment, *Phys. Rev.* **53**, 318 (1938).
- [47] I. I. Rabi, S. Millman, P. Kusch, and J. R. Zacharias, The molecular beam resonance method for measuring nuclear magnetic moments: The magnetic moments of ${}^3\text{Li}^6$, ${}^3\text{Li}^7$ and ${}^9\text{F}^{19}$, *Phys. Rev.* **55**, 526 (1939).
- [48] N. F. Ramsey, A new molecular beam resonance method, *Phys. Rev.* **76**, 996 (1949).
- [49] N. F. Ramsey, Experiments with separated oscillatory fields and hydrogen masers, *Rev. Mod. Phys.* **62**, 541 (1990).
- [50] V. F. Ezhov, S. N. Ivanov, I. M. Lobashov, V. A. Nazarenko, G. D. Posev, A. P. Serebrov, and R. R. Toldaev, Adiabatic method of separated oscillatory fields, *JETP Lett.* **24**, 34 (1976).
- [51] Y. Makhlin, G. Schön, and A. Shnirman, Quantum-state engineering with Josephson-junction devices, *Rev. Mod. Phys.* **73**, 357 (2001).
- [52] N. F. Ramsey, History of atomic clocks, *J. Res. Nat. Bur. Stand.* **88**, 301 (1983).
- [53] K. Winkler, G. Thalhammer, M. Theis, H. Ritsch, R. Grimm, and J. H. Denschlag, Atom-molecule dark states in a Bose-Einstein condensate, *Phys. Rev. Lett.* **95**, 063202 (2005).

- [54] C. Ryu, X. Du, E. Yesilada, A. M. Dudarev, S. Wan, Q. Niu, and D. J. Heinzen, Raman-induced oscillation between an atomic and a molecular quantum gas, *arXiv:cond-mat/0508201* (2005).
- [55] A. V. Andreev, V. Gurarie, and L. Radzihovsky, Nonequilibrium dynamics and thermodynamics of a degenerate Fermi gas across a Feshbach resonance, *Phys. Rev. Lett.* **93**, 130402 (2004).
- [56] R. A. Barankov and L. S. Levitov, Atom-molecule coexistence and collective dynamics near a Feshbach resonance of cold fermions, *Phys. Rev. Lett.* **93**, 130403 (2004).
- [57] J. von Stecher and C. H. Greene, Spectrum and dynamics of the BCS-BEC crossover from a few-body perspective, *Phys. Rev. Lett.* **99**, 090402 (2007).
- [58] O. Dannenberg, M. Mackie, and K.-A. Suominen, Shortcut to a Fermi-degenerate gas of molecules via cooperative association, *Phys. Rev. Lett.* **91**, 210404 (2003).
- [59] M. Wouters, J. Tempere, and J. T. Devreese, Resonant dynamics in boson-fermion mixtures, *Phys. Rev. A* **67**, 063609 (2003).
- [60] J. Goldwin, Quantum degeneracy and interactions in the ^{87}Rb - ^{40}K Bose-Fermi mixture, Ph.D. thesis, University of Colorado, Boulder, 2005.
- [61] E. Hodby, S. T. Thompson, C. A. Regal, M. Greiner, A. C. Wilson, D. S. Jin, E. A. Cornell, and C. E. Wieman, Production efficiency of ultracold Feshbach molecules in bosonic and fermionic systems, *Phys. Rev. Lett.* **94**, 120402 (2005).
- [62] S. T. Thompson, E. Hodby, and C. E. Wieman, Ultracold molecule production via a resonant oscillating magnetic field, *Phys. Rev. Lett.* **95**, 190404 (2005).
- [63] S. B. Papp and C. E. Wieman, Observation of heteronuclear Feshbach molecules in a ^{85}Rb - ^{87}Rb gas, *Phys. Rev. Lett.* **97**, 180404 (2006).
- [64] J. J. Zirbel, K.-K. Ni, S. Ospelkaus, T. L. Nicholson, M. L. Olsen, P. S. Julienne, C. E. Wieman, J. Ye, and D. S. Jin, Heteronuclear molecules in an optical dipole trap, *Phys. Rev. A* **78**, 013416 (2008).
- [65] B. DeMarco, H. Rohner, and D. S. Jin, An enriched ^{40}K source for fermionic atom studies, *Rev. Sci. Instrum.* **70**, 1967 (1999).
- [66] *CRC Handbook of Chemistry and Physics*, edited by D. R. Lide (CRC Press, Boca Raton, 2008).
- [67] J. Goldwin, S. B. Papp, B. DeMarco, and D. S. Jin, Two-species magneto-optical trap with ^{40}K and ^{87}Rb , *Phys. Rev. A* **65**, 021402 (2002).

- [68] C. Monroe, W. Swann, H. Robinson, and C. Wieman, Very cold trapped atoms in a vapor cell, *Phys. Rev. Lett.* **65**, 1571 (1990).
- [69] B. P. Anderson and M. A. Kasevich, Loading a vapor-cell magneto-optic trap using light-induced atom desorption, *Phys. Rev. A* **63**, 023404 (2001).
- [70] J. J. Zirbel, Ultracold fermionic Feshbach molecules, Ph.D. thesis, University of Colorado, Boulder, 2008.
- [71] E. Arimondo, M. Inguscio, and P. Violino, Experimental determinations of the hyperfine structure in the alkali atoms, *Rev. Mod. Phys.* **49**, 31 (1977).
- [72] T. Walker, D. Sesko, and C. Wieman, Collective behavior of optically trapped neutral atoms, *Phys. Rev. Lett.* **64**, 408 (1990).
- [73] W. Petrich, M. H. Anderson, J. R. Ensher, and E. A. Cornell, Behavior of atoms in a compressed magneto-optical trap, *J. Opt. Soc. Am. B* **11**, 1332 (1994).
- [74] J. Dalibard and C. Cohen-Tannoudji, Laser cooling below the Doppler limit by polarization gradients: simple theoretical models, *J. Opt. Soc. Am. B* **6**, 2023 (1989).
- [75] S. B. Papp, Experiments with a two-species Bose-Einstein condensate utilizing widely tunable interparticle interactions., Ph.D. thesis, University of Colorado, Boulder, 2007.
- [76] A. G. Truscott, K. E. Strecker, W. I. McAlexander, G. B. Partridge, and R. G. Hulet, Observation of Fermi pressure in a gas of trapped atoms, *Science* **291**, 5513 (2001).
- [77] M. Brown-Hayes and R. Onofrio, Optimal cooling strategies for magnetically trapped atomic Fermi-Bose mixtures, *Phys. Rev. A* **70**, 063614 (2004).
- [78] B. DeMarco, Quantum behavior of an atomic Fermi gas, Ph.D. thesis, University of Colorado, Boulder, 2001.
- [79] J. R. Ensher, The first experiments with Bose-Einstein condensation of ^{87}Rb , Ph.D. thesis, University of Colorado, Boulder, 1998.
- [80] J. L. Roberts, Bose-Einstein condensates with tunable atom-atom interactions: The first experiments with ^{85}Rb BECs, Ph.D. thesis, University of Colorado, Boulder, 2001.
- [81] K. B. MacAdam, A. Steinbach, and C. Wieman, A narrow band tunable diode laser system with grating feedback, and a saturated absorption spectrometer for Cs and Rb, *Am. J. Phys.* **60**, 1098 (1992).

- [82] U. Fano, Effects of configuration interaction on intensities and phase shifts, *Phys. Rev.* **124**, 1866 (1961).
- [83] H. Feshbach, A unified theory of nuclear reactions. II, *Ann. Phys.* **19**, 287 (1962).
- [84] W. C. Stwalley, Stability of spin-aligned hydrogen at low temperatures and high magnetic fields: New field-dependent scattering resonances and predissociations, *Phys. Rev. Lett.* **37**, 1628 (1976).
- [85] E. Tiesinga, B. J. Verhaar, and H. T. C. Stoof, Threshold and resonance phenomena in ultracold ground-state collisions, *Phys. Rev. A* **47**, 4114 (1993).
- [86] K. Goral, T. Kohler, S. A. Gardiner, E. Tiesinga, and P. S. Julienne, Adiabatic association of ultracold molecules via magnetic-field tunable interactions, *J. Phys. B: At. Mol. Opt. Phys.* **37**, 3457 (2004).
- [87] C. Chin, A simple model of Feshbach molecules, *arXiv:cond-mat/0506313* (2005).
- [88] A. J. Moerdijk, B. J. Verhaar, and A. Axelsson, Resonances in ultracold collisions of ${}^6\text{Li}$, ${}^7\text{Li}$, and ${}^{23}\text{Na}$, *Phys. Rev. A* **51**, 4852 (1995).
- [89] J. J. Sakurai, *Modern Quantum Mechanics* (The Benjamin/Cummings Publishing Company, Menlo Park, CA, 1985).
- [90] L. D. Landau and E. M. Lifshitz, *Quantum mechanics: Non-relativistic theory* (Pergamon Press, Oxford, 1965).
- [91] S. Inouye, M. R. Andrews, J. Stenger, H. J. Miesner, D. M. Stamper-Kurn, and W. Ketterle, Observation of Feshbach resonances in a Bose-Einstein condensate, *Nature* **392**, 151 (1998).
- [92] F. Ferlaino, C. D'Errico, G. Roati, M. Zaccanti, M. Inguscio, G. Modugno, and A. Simoni, Erratum: Feshbach spectroscopy of a K-Rb atomic mixture [Phys. Rev. A **73**, 040702 (2006)], *Phys. Rev. A* **74**, 039903 (2006).
- [93] E. Nielsen and J. H. Macek, Low-energy recombination of identical bosons by three-body collisions, *Phys. Rev. Lett.* **83**, 1566 (1999).
- [94] B. D. Esry, C. H. Greene, and J. P. Burke, Recombination of three atoms in the ultracold limit, *Phys. Rev. Lett.* **83**, 1751 (1999).
- [95] F. H. Mies, C. J. Williams, P. S. Julienne, and M. Krauss, Estimating bounds on collisional relaxation rates of spin-polarized ${}^{87}\text{Rb}$ atoms at ultracold temperatures., *J. Res. Natl. Inst. Stand. Technol.* **101**, 521 (1996).

- [96] P. O. Fedichev, M. W. Reynolds, and G. V. Shlyapnikov, Three-body recombination of ultracold atoms to a weakly bound s level, *Phys. Rev. Lett.* **77**, 2921 (1996).
- [97] A. J. Moerdijk, H. M. J. M. Boesten, and B. J. Verhaar, Decay of trapped ultracold alkali atoms by recombination, *Phys. Rev. A* **53**, 916 (1996).
- [98] J. Stenger, S. Inouye, M. R. Andrews, H.-J. Miesner, D. M. Stamper-Kurn, and W. Ketterle, Strongly enhanced inelastic collisions in a Bose-Einstein condensate near Feshbach resonances, *Phys. Rev. Lett.* **82**, 2422 (1999).
- [99] J. L. Roberts, N. R. Claussen, S. L. Cornish, and C. E. Wieman, Magnetic field dependence of ultracold inelastic collisions near a Feshbach resonance, *Phys. Rev. Lett.* **85**, 728 (2000).
- [100] V. Vuleti, A. J. Kerman, C. Chin, and S. Chu, Observation of low-field Feshbach resonances in collisions of cesium atoms, *Phys. Rev. Lett.* **82**, 1406 (1999).
- [101] C. A. Regal, C. Ticknor, J. L. Bohn, and D. S. Jin, Tuning p-wave interactions in an ultracold Fermi gas of atoms, *Phys. Rev. Lett.* **90**, 053201 (2003).
- [102] C. Ticknor, C. A. Regal, D. S. Jin, and J. L. Bohn, Multiplet structure of Feshbach resonances in nonzero partial waves, *Phys. Rev. A* **69**, 042712 (2004).
- [103] T. Weber, J. Herbig, M. Mark, H.-C. Nägerl, and R. Grimm, Three-body recombination at large scattering lengths in an ultracold atomic gas, *Phys. Rev. Lett.* **91**, 123201 (2003).
- [104] S. L. Cornish, N. R. Claussen, J. L. Roberts, E. A. Cornell, and C. E. Wieman, Stable ^{85}Rb Bose-Einstein condensates with widely tunable interactions, *Phys. Rev. Lett.* **85**, 1795 (2000).
- [105] C. A. Regal, C. Ticknor, J. L. Bohn, and D. S. Jin, Creation of ultracold molecules from a Fermi gas of atoms, *Nature* **424**, 47 (2003).
- [106] J. J. Zirbel, K.-K. Ni, S. Ospelkaus, J. P. D'Incao, C. E. Wieman, J. Ye, and D. S. Jin, Collisional stability of fermionic Feshbach molecules, *Phys. Rev. Lett.* **100**, 143201 (2008).
- [107] J. P. D'Incao and B. D. Esry, Suppression of molecular decay in ultracold gases without Fermi statistics, *Phys. Rev. Lett.* **100**, 163201 (2008).
- [108] J. E. Williams, N. Nygaard, and C. W. Clark, Theory of Feshbach molecule formation in a dilute gas during a magnetic field ramp., *N. J. Phys.* **8**, 150 (2006).

- [109] C. H. Greene, Private communication, .
- [110] S. Kotochigova, Private communication, .
- [111] S. Rousseau, A. R. Allouche, and M. Aubert-Frcon, Theoretical study of the electronic structure of the KRb molecule, *J. Mol. Spectrosc.* **203**, 235 (2000).
- [112] C. Ospelkaus, S. Ospelkaus, L. Humbert, P. Ernst, K. Sengstock, and K. Bongs, Ultracold heteronuclear molecules in a 3D optical lattice, *Phys. Rev. Lett.* **97**, 120402 (2006).
- [113] C. A. Regal and D. S. Jin, private communication, .
- [114] D. E. Miller, J. R. Anglin, J. R. Abo-Shaeer, K. Xu, J. K. Chin, and W. Ketterle, High-contrast interference in a thermal cloud of atoms, *Phys. Rev. A* **71**, 043615 (2005).
- [115] C. Cohen-Tannoudji, J. Dupont-Roc, and G. Grynberg, *Atom-Photon Interactions* (John Wiley & Sons, New York, 1998).
- [116] H. J. Metcalf and P. van der Straten, *Laser Cooling and Trapping* (Springer, New York, 1999).
- [117] K. Góral, T. Köhler, and K. Burnett, Ramsey interferometry with atoms and molecules: Two-body versus many-body phenomena, *Phys. Rev. A* **71**, 023603 (2005).
- [118] P. S. Julienne, E. Tiesinga, and T. Köhler, Making cold molecules by time-dependent feshbach resonances, *J. Mod. Opt.* **51**, 1787 (2004).
- [119] G. F. Gribakin and V. V. Flambaum, Calculation of the scattering length in atomic collisions using the semiclassical approximation, *Phys. Rev. A* **48**, 546 (1993).
- [120] B. Borca, D. Blume, and C. H. Greene, A two-atom picture of coherent atom-molecule quantum beats, *N. J. Phys.* **5**, 111 (2003).
- [121] C. A. Regal, M. Greiner, and D. S. Jin, Lifetime of molecule-atom mixtures near a Feshbach resonance in ${}^{40}\text{K}$, *Phys. Rev. Lett.* **92**, 083201 (2004).
- [122] S. T. Thompson, E. Hodby, and C. E. Wieman, Spontaneous dissociation of ${}^{85}\text{Rb}$ Feshbach molecules, *Phys. Rev. Lett.* **94**, 020401 (2005).
- [123] K. Xu, T. Mukaiyama, J. R. Abo-Shaeer, J. K. Chin, D. E. Miller, and W. Ketterle, Formation of quantum-degenerate sodium molecules, *Phys. Rev. Lett.* **91**, 210402 (2003).

- [124] S. Dürr, T. Volz, A. Marte, and G. Rempe, Observation of molecules produced from a Bose-Einstein condensate, *Phys. Rev. Lett.* **92**, 020406 (2004).
- [125] J. Zhang, E. G. M. Van Kempen, T. Bourdel, L. Khaykovich, J. Cubizolles, F. Chevy, M. Teichmann, L. Tarruell, S. J. J. M. F. Kokkelmans, and C. Salomon, Expansion of a lithium gas in the BEC-BCS crossover, *arXiv:cond-mat/0410167v1* (2004).
- [126] N. Zahzam, T. Vogt, M. Mudrich, D. Comparat, and P. Pillet, Atom-molecule collisions in an optically trapped gas, *Phys. Rev. Lett.* **96**, 023202 (2006).

Appendix A

Fitting dephased oscillations

In Chapter 5, I posited that the damping of the observed atom-molecule oscillations is likely caused by a distribution of oscillation frequencies of the atom pairs. This distribution of frequencies may be due to the relative kinetic energies of the atom pairs, but for much of the data, it is most likely due to the inhomogeneity of the magnetic field. We fit the data to sines with Gaussian envelopes and extracted oscillation frequencies. In this appendix, I address the question of how the measured frequency is influenced by the shape of the distribution of oscillation frequency.

We will begin with the case of an oscillation with a coherence time defined purely by the inhomogeneity of the magnetic field. For the purpose of illustration, we will consider an atom cloud well above quantum degeneracy such that the positions of the atoms are described by a Gaussian distribution. We also assume that in the absence of the magnetic-field inhomogeneity, each pair would oscillate with a frequency ν_0 , equal to the molecule binding energy divided by \hbar (i.e. all the atom pairs occupy a single energy state). In the experiment, we find the magnetic field varies linearly along the axial direction of the cloud with a gradient of 0.5G/cm. As shown in Fig. A.1a, this implies a Gaussian distribution of magnetic fields across the cloud. Figure A.1b shows the resulting distribution of oscillation frequencies. Here, we have assumed $\nu_0 = 100$ kHz corresponds to the

molecule binding energy at the center of the cloud. The distribution of frequencies is also well-approximated by a Gaussian.¹ The oscillation in the total population is the sum of the oscillations of all the pairs

$$\begin{aligned} N_{\text{mol}}(t) &= \frac{N_{\text{pairs}}}{2} \left(A \int_0^\infty \sin(2\pi\nu t) e^{-(\nu-\nu_0)^2/(2\sigma^2)} d\nu + 1 \right) \\ N_{\text{mot}}(t) &= \frac{N_{\text{pairs}}}{2} \left(e^{-t^2\sigma^2/2} \sin(2\pi\nu_0 t) + 1 \right). \end{aligned} \quad (\text{A.1})$$

In this case of a Gaussian frequency distribution around ν_0 , the total population oscillation will have a frequency of ν_0 and be bounded by a Gaussian envelope.

Now, let us consider atom pairs in a uniform magnetic field, but with a distribution of relative kinetic energies. Once again, we assume a classical gas. If the energy distribution of the pairs mimics that of nearest neighbors, the relative kinetic energy E will follow the Boltzmann energy distribution (see Fig. A.2)

$$P(E) = A\sqrt{E}e^{-E/(k_b T)}, \quad (\text{A.2})$$

where A is a normalization constant and k_b is the Boltzmann constant. If we assume each atom pair will oscillate with a frequency $\nu = \nu_0 + \nu_E$, where $\nu_E = E/h$, then the oscillation in the total population will be given by

$$\begin{aligned} N_{\text{mol}}(t) &= \frac{N_{\text{max}}}{2} \left(\frac{2}{\tau^{3/2}\sqrt{\pi}} \int_0^\infty \sin(2\pi(\nu_0 + \nu_E)t) \sqrt{\nu_E} e^{-\nu_E/\tau} d\nu_E + 1 \right) \\ N_{\text{mol}}(t) &= \frac{N_{\text{max}}}{2} \left(\frac{\sin(2\pi\nu_0 t + \frac{3}{2}\arctan(2\pi t\tau))}{(1 + (2\pi t\tau)^2)^{3/4}} + 1 \right), \end{aligned} \quad (\text{A.3})$$

where $\tau = k_b T/h$. Figure A.3a shows the oscillation of a 200 nK cloud with $\nu_0 = 100$ kHz. In this case, the frequency of the oscillation in the total population varies with time. We can rewrite the argument of the sine to make this explicit

$$2\pi\nu_0 t + \frac{3}{2}\arctan(2\pi t\tau) = 2\pi t \left(\nu_0 + \frac{3\arctan(2\pi t\tau)}{4\pi t} \right),$$

¹ For larger variations in magnetic field or very near the resonance, the quadratic dependence of the binding energy on magnetic field causes this distribution to become asymmetric.

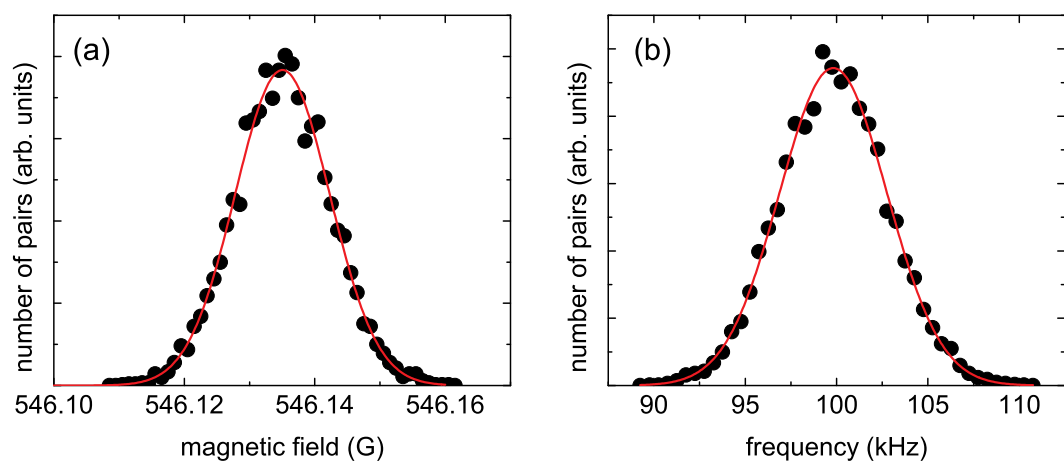


Figure A.1: Frequency distribution due to an inhomogeneous magnetic field. Using the Monte Carlo simulation discussed in chapter 4, we generate Gaussian clouds with an rms size of $150 \mu\text{m}$ in the axial direction. We then calculate the magnetic field and corresponding molecule binding energy (using Eq. 5.8) for each pair's average position assuming a 0.5 G/cm gradient along the axial direction. The calculated distribution of magnetic fields (a) and oscillation frequencies (b) are shown for a cloud centered on $B = 546.135 \text{ G}$, where the molecule binding energy is $h\nu_0 = h \times 100 \text{ kHz}$. The red curves show Gaussian fits with rms widths $\sigma_B = 7.2 \text{ mG}$ and $\sigma_\nu = 2.9 \text{ kHz}$.

$$\nu(t) = v_0 + \frac{3 \arctan(2\pi t\tau)}{4\pi t}. \quad (\text{A.4})$$

Figure A.3b shows the time dependence of the frequency. Since all of the pairs have frequencies $\geq \nu_0$, the initial frequency of the oscillation in the total population is also higher than ν_0 . The pairs at the high energy tail of the Boltzmann distribution (pairs with high oscillation frequencies) are the first to dephase, and the frequency decreases, approaching the zero-energy pair frequency, ν_0 . If we were to fit this oscillation to a sine with a Gaussian envelope, we would underestimate the coherence time and measure a frequency blue-shifted from the molecule binding energy by up to $\frac{3}{2}\tau = \frac{3}{2} \frac{k_b T}{h}$.

Now, we consider a distribution of relative kinetic energies of the oscillating pairs that reflects the energy distribution of molecules created via adiabatic magnetic-field sweeps. In this case, we must obtain the energy distribution from the Monte Carlo simulation (see Chapter 4). Figure A.4 shows the distribution of relative kinetic energies of the atom pairs that become molecules for a mixture with $N_K = 2.5N_{\text{Rb}}$ at 200 nK, which corresponds to 1.2 T_C and 0.3 T_F .

Figure A.5a shows the calculated oscillation with $\nu_0 = 10$ kHz. The distribution of relative kinetic energies leads to a variation of the oscillation frequency in time. To extract the frequency as a function of time, we fit the oscillation in Fig. A.5a with a sliding window 100 μs wide. Figure A.5b shows the difference between the fitted frequency and ν_0 . As in the case of the Boltzmann energy distribution above, the measured frequency approaches the zero-energy frequency as the high-energy pairs dephase. The apparent dip around 700 μs is likely an artifact of the fitting. Initially, the frequency exceeds ν_0 by 0.4 kHz, which is equal to $0.1 \frac{k_b T}{h}$. This is much smaller than the shift for the Boltzmann distribution, indicating that the adiabatic molecule formation process modeled with the Monte Carlo simulation preferentially forms pairs with small relative kinetic energy.

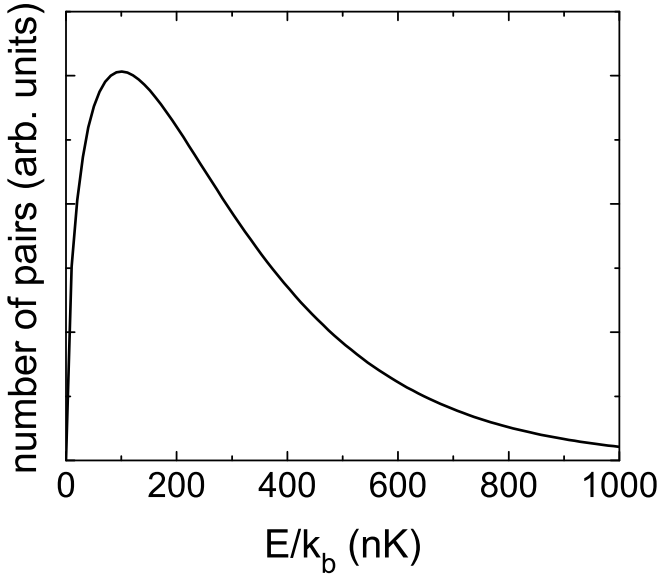


Figure A.2: Calculated distribution of relative kinetic energies, E , of nearest-neighbor pairs in a 200 nK Boltzmann gas.

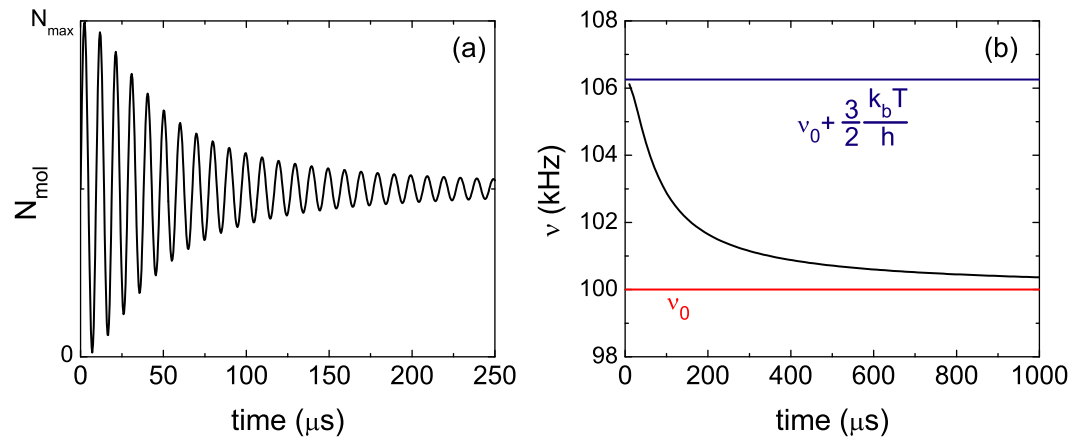


Figure A.3: Calculated atom-molecule oscillation for a 200 nK gas with a Boltzmann energy distribution at $B = 546.135\text{G}$. The number of molecules as a function of time, calculated with Eq. A.3 is shown in (a). The frequency ν , calculated with Eq. A.4 is plotted in (b). The frequency of a pair with zero relative kinetic energy is $\nu_0 = 100$ kHz.

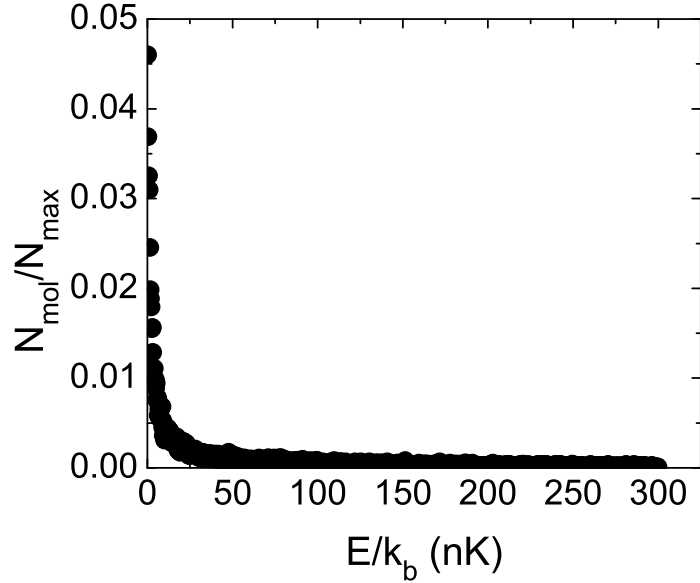


Figure A.4: Calculated distribution of the relative kinetic energies E of atom pairs associated into molecules in the Monte Carlo simulation. The points are the results of a simulation of a mixture with $N_K = 2.5 N_{Rb}$ at 200 nK, which corresponds to $1.2 T_C$.

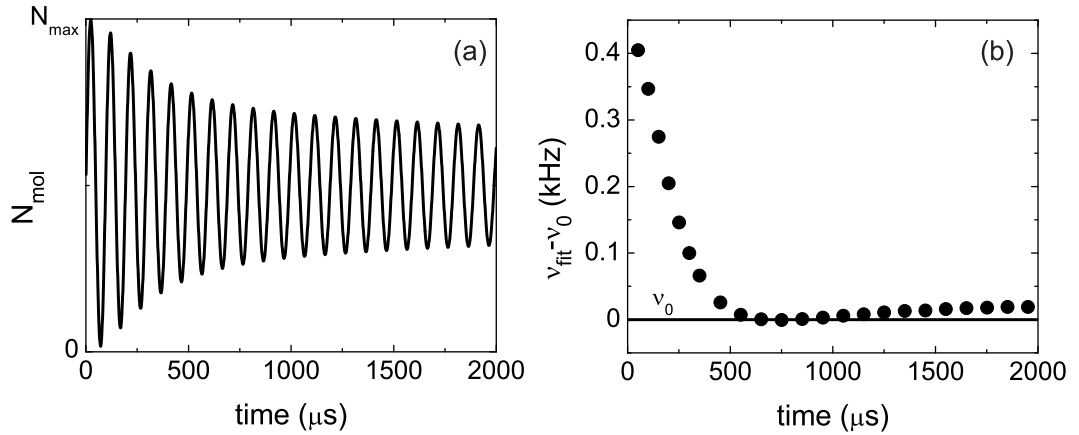


Figure A.5: Calculated atom-molecule oscillation for pairs with the distribution shown in Fig. A.4. The calculated number of molecules as a function of time is shown in (a). Fits to the oscillation were performed, and the frequency ν_{fit} in a sliding window 100 μs wide was extracted. The difference between ν_{fit} and the zero energy oscillation frequency ν_0 is shown in (b). Initially, the ν_{fit} exceeds ν_0 by 0.4 kHz, which is $0.1 k_b T / \hbar$.

We know that in the experiment, we have magnetic-field inhomogeneities *and* a distribution of energies. If the magnetic field limits the coherence time to, say, $30\mu\text{s}$, then the measured frequency will be the zero-energy frequency (molecule binding energy divided by h) shifted by the frequency of the energy-distributed oscillation during the first $30 \mu\text{s}$, i.e. $\sim \frac{3}{2} \frac{k_b T}{h}$ and $\sim 0.1 \frac{k_b T}{h}$ for the above examples. Therefore, the measured frequencies in Fig. 5.6 may be shifted from the molecule binding energy by up to $\frac{3}{2} \frac{k_b T}{h} = 6 \text{ kHz}$.

Appendix B

Nearest-neighbor distance and density-weighted density for Gaussian clouds with different sizes, numbers, and aspect ratios.

Often working with a two-species experiment requires extending theory done for single-species experiments. Sometimes this can be as simple as replacing an atomic mass with twice the reduced mass, but at times it is necessary to know the average density or nearest-neighbor distance. In this appendix, I address the questions of how to define these quantities in the two-species case. For this discussion, both clouds are assumed to have Gaussian profiles, but may contain different numbers of atoms and have different rms widths and aspect ratios.

We begin with the question of how to define the typical nearest-neighbor distance, which is relevant in comparison to the size of the molecules near a Fano-Feshbach resonance (see chapter 5). At first glance, this seems a simple task—generate Gaussian clouds, pick an atom, find its nearest neighbor (of the opposite species), calculate the separation between the two atoms, and repeat until all the atoms have been counted. In the case of two clouds with different numbers of atoms, we encounter a hitch: on average, the distance to the nearest atom in the opposite species depends on which species we are considering. This is illustrated in Fig. B.1. Here, we have a larger number of red atoms than blue atoms. If we calculate the average distance from a red atom to the nearest blue atom (option 1), we will find a much larger distance than if we calculate the average distance

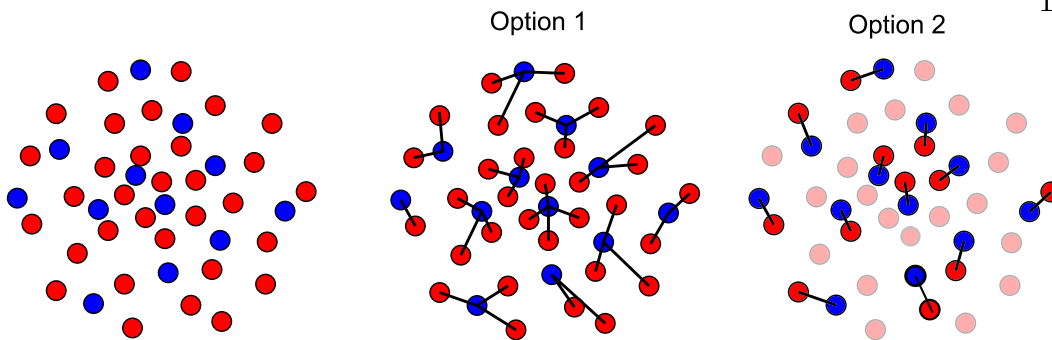


Figure B.1: Illustration of the calculation of the typical nearest-neighbor distance for a mixture with different numbers of atoms. In Option 1, we calculate the distance from a given red atom to the nearest blue atom. In Option 2, we calculate the distance from a given blue atom to the nearest red atom.

from a blue atom to the nearest red atom (option 2). So, which do we choose? In considering molecule creation, we might expect that an atom is likely to bind to its nearest neighbor. We would want to compare the distances between the Rb and K atom of each nearest-neighbor pair to the interatomic distance in a molecule (Eq. 5.6). In option 1, a single blue atom can be the nearest neighbor to many red atoms, but if it were to form a molecule, the blue atom would only pair with one red atom. In option 2, the gas is separated into nearest-neighbor pairs and lone red atoms, as would occur if every possible atom were to be associated into a molecule. In the following discussion, we will always calculate the nearest-neighbor distance d_{nn} from the cloud with fewer atoms, a.k.a. option 2.

If we properly define the nearest-neighbor distance and the two-species density n_{KRB} , we expect the relationship

$$d_{nn} = C (n_{KRB})^{-1/3} \quad (\text{B.1})$$

where C is a proportionality constant. Figure B.2 shows a typical distribution of nearest-neighbor distances in a Gaussian cloud.

In a single-species experiment, there are typically two relevant measures of density, the peak density n_0 and the average, or density-weighted, density

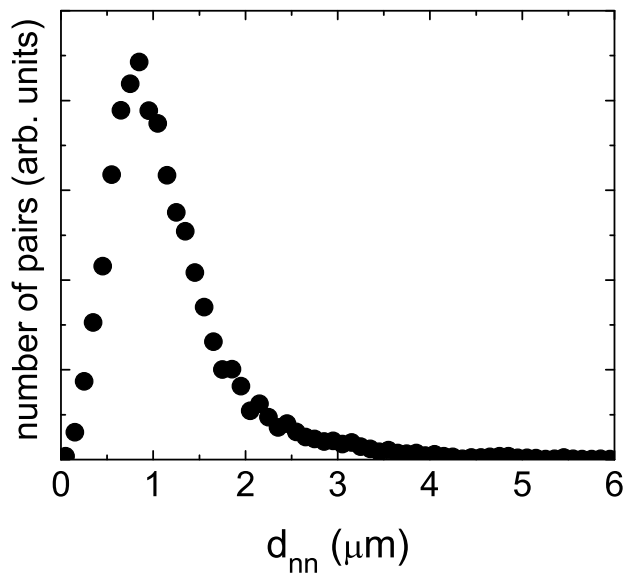


Figure B.2: Calculated distribution of nearest-neighbor distances d_{nn} for a simulated Gaussian cloud.

$\langle n \rangle = \frac{1}{N} \int n^2(\mathbf{r}) d^3r$. Here, $n(\mathbf{r})$ is the number density of atoms. We generalize this to the two-species case as $\langle n_{12} \rangle = \frac{1}{N_<} \int n_1(\mathbf{r})n_2(\mathbf{r}) d^3r$, where we have normalized by $N_<$, the number of atoms in the species with fewer atoms.

For a Gaussian cloud, the density is given by

$$n(\mathbf{r}) = n_0 e^{-\frac{1}{2\sigma_r^2}(r^2 + \lambda^2 z^2)}, \quad (\text{B.2})$$

where σ_r is the rms size in the radial direction, $\lambda = \sigma_z/\sigma_r$ is the ratio of the axial and radial sizes, and $n_0 = N\lambda/(2\pi\sigma_r^2)^{3/2}$. For two Gaussian clouds with different sizes, numbers, and aspect ratios (but the same center), the density-weighted density is

$$\langle n_{12} \rangle = \left(\frac{1}{2\pi} \right)^{3/2} N_2 \lambda_1 \lambda_2 \left(\frac{1}{\sigma_1^2 + \sigma_2^2} \right) \left(\frac{1}{\lambda_1^2 \sigma_2^2 + \lambda_2^2 \sigma_1^2} \right)^{1/2}, \quad (\text{B.3})$$

where we have assumed that $N_2 \geq N_1$. Figure B.3 shows the most probable nearest-neighbor distance in simulated clouds as a function of the two-species density $\langle n_{12} \rangle$ calculated with Eq. B.3. We find the expected relation, Eq. B.1, with the proportionality constant $C \sim \frac{1}{2}$. Note that all of the simulations were performed for the case where the cloud with fewer atoms is the spatially smaller cloud and has a lower density ($N_1 \leq N_2$, $\sigma_1 \leq \sigma_2$ in both the axial and radial directions, and $n_1 \leq n_2$ for all space).

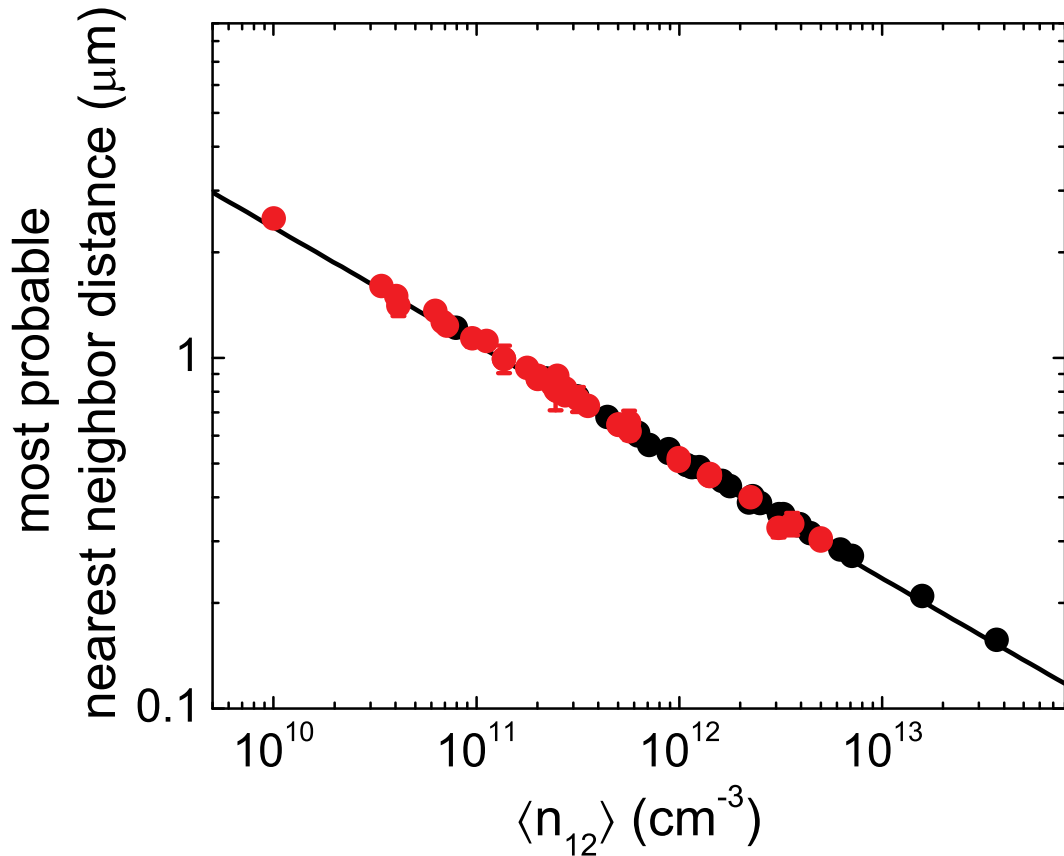


Figure B.3: Density dependence of the calculated nearest-neighbor distance. The most probable nearest-neighbor distance d_{nn} is plotted as a function of the two-species density-weighted density $\langle n_{12} \rangle$ (Eq. B.3) for simulated Gaussian clouds. The black points indicate simulations where the number and sizes of the two clouds are the same. In the simulations represented by the red points, the numbers, sizes, and/or aspect ratios of the two clouds differ from one another. The line is a fit to $d_{nn} = C \langle n_{12} \rangle^{-1/b}$ with $C = 0.51 \pm 0.03$ and $b = 3.008 \pm 0.019$.